THE LONG-TERM EVOLUTION OF SUBDUCTION ZONES: A MODELLING STUDY

DAGMAR OLBERTZ

THE LONG-TERM EVOLUTION OF SUBDUCTION ZONES: A MODELLING STUDY

DAGMAR OLBERTZ

THE LONG-TERM EVOLUTION OF SUBDUCTION ZONES: A MODELLING STUDY

De evolutie van subductie zones:
een numerieke modelstudie

(met een samenvatting in het Nederlands)

PROEFSCHRIFT

TER VERKRIJGING VAN DE GRAAD VAN DOCTOR
AAN DE UNIVERSITEIT UTRECHT OP GEZAG VAN DE
RECTOR MAGNIFICUS, PROF. DR J.A. VAN GINKEL
INGEVOLGE HET BESLUIT VAN HET COLLEGE VAN DEKANEN
IN HET OPENBAAR TE VERDEDIGEN
OP DINSDAG 8 APRIL 1997 DES NAMIDDAGS TE 12:45 UUR

door

DAGMAR CORDULA OLBERTZ

Geboren op 16 Mei 1963, te Köln, Duitsland

Promotor: Prof. Dr. M. J. R. Wortel

Co-Promotor: Prof. Dr. U. Hansen

The following publication has resulted from this study (Chapter 5):

Olbertz, D., M.J.R. Wortel, and U. Hansen, Trench migration and subduction zone geometry, *Geophys. Res. Lett., in press*, 1997.

*Wenn du aufwärts gehst und dich hochaufatmend
umsiehst, was du doch für ein Kerl bist, der solche
Höhen erklimmen kann, du, ganz allein -: dann
entdeckst du immer Spuren im Schnee. [...] und
immer ist einer dagewesen, und immer ist einer
noch höher geklettert als du es je gekonnt hast,
noch viel höher. Das darf dich nicht entmutigen.
Klettere, steige, steige. Aber es gibt keine Spitze.
Und es gibt keinen Neuschnee.*

Kurt Tucholsky, 1931
Es gibt keinen Neuschnee

Für Ralf und Yvonne

Contents

CHAPTER 1

Introduction and Summary

The motion of oceanic and continental lithosphere, volcanic activity, earthquakes, and other tectonic activities are expressions of processes in the Earth's mantle. Nowadays, it is widely accepted that these phenomena are related to convective flow in the mantle, which forms the mechanism to turn heat from the Earth's interior into mechanical work. One example of that mechanism is the creation of oceanic lithosphere at the mid-ocean ridges, which are zones of upwelling hot mantle material. At boundaries where two plates converge one of the plates, preferebly of oceanic type, is consumed by subduction into the mantle.

Most of the information about the Earth's structure has been obtained by seismology. Seismological observations have demonstrated that there is a great variety in subduction zone geometries. Subducted slabs with dip angles varying from very small (e.g. Peru) to nearly 90° (e.g. Mariana) have been observed. Slabs can either stagnate at the upper-lower mantle boundary (e.g. Izu-Bonin) or can penetrate into the lower mantle (e.g. Sunda arc). Initiation or cessation of subduction are manifestations of the time-dependence of the dynamical processes in the mantle. Images of the seismic velocity distribution of the mantle interior provide an instantaneous view of time-dependent structures which must be interpreted in a dynamical context. Understanding the long-term evolution of the subduction process is the primary motivation for this study. More specifically, the aim is to investigate the sensitivity of subduction zone geometry to various parameters, as, for example, plate velocities and viscosity structure of the mantle. For that purpose we have chosen to use a computational method. Numerical studies have the advantage that parameters can be varied over a great range. Plate motions and mantle flow can be included as boundary conditions easily, particularly compared to laboratory experiments. It must be emphasized that the model used here includes several shortcomings. The major simplification is probably the neglect of the third dimension.

Over the last two decades numerous studies concerning subduction zones have been performed. In *Chapter 2* a summary of some influential work and recent studies from different fields of geophysical disciplines is presented. Constraints on the structure and evolution of subducting slabs obtained from seismology, geoid data, plate tectonic analysis, and numerical and experimental studies are discussed. This information forms the basis for the research presented in this thesis.

In *Chapter 3* the numerical method used for the two-dimensional models is presented. First, the basic equations describing the convection system in a fluid resembling the Earth's mantle are given. Secondly, the finite element method

which is applied for solving the coupled system of partial differential equations of motion and energy is described. Since the study presented here is mainly based on seismological results we include the possibility to transform the model temperature to seismic velocity anomalies. The conversion is outlined in *Chapter 3*.

Chapter 4 addresses the influence of the viscosity structure of the mantle on a subducting slab. The viscosity might decrease across the lithosphere by three to four orders of magnitude. At the upper-lower mantle boundary it probably increases by a factor of 10 to 100. Details about the viscosity profile of the Earth are still debated.

As the first model results are presented in *Chapter 4* the model set up and geometry are described. The model domain spans the uppermost 1200 km of the Earth's mantle. Appropriate boundary conditions, as for example a background mantle flow and an 'open' bottom, which is permeable for material flow, provide a model domain as being part of the whole mantle convection system. Stiffness of lithospheric plates is modeled with temperature-dependence of the viscosity. Rayleigh number (Ra), which is a measure for the instability of a convection system, is chosen to be between 10^6 and 10^7. Based on the upper mantle viscosity an increase in Ra by one order of magnitude implies a decrease of the reference viscosity by one order of magnitude. The choice of Ra is consistent with the open nature of our model as being part of a whole mantle convection system.

Our two-dimensional models show that a ratio of lower to upper mantle viscosity up to 300 is not able to prevent a subducting slab from entering the lower mantle. The geometry of the subduction related anomaly structure (both temperature and seismic anomaly) strongly depends on the viscous properties of the descending lithosphere. We also find that a change in velocity of the underthrusting plate does not affect slab geometry significantly. In summary, we conclude that the great variety observed in seismic velocity structure of subduction zones cannot be explained by variations in viscosity and plate velocity of the underthrusting plate only.

Chapter 5 is devoted to the effect of trench migration on the subduction process. Additional to the models of *Chapter 4* the overriding plate is movable. For the analysis of trench migration background mantle flow becomes important. Not only absolute plate/trench velocities, such as specified by e.g. the hotspot reference frame, but also relative motions between surface plates and the mantle fow beneath must be considered. This chapter is divided into three main parts: In the first part we investigate the change in viscosity, but contrary to chapter 4, while trench migration is present. Based on results from both *Chapter 4* and *Chapter 5* for the further study one viscosity profile is chosen. In the second part a detailed study of the effect of trench migration on the subduction process is then performed without varying the radially viscosity structure. Analysis of relative motions between lithosphere and mantle has indicated an overall eastward mantle flow relative to

the plates. This implies that there might be differences between subducting slabs dipping to the east and those dipping to the west. Comparison between west and east dipping subduction zones is the subject of the third part.

We find that in combination with trench migration the increase in upper to lower mantle viscosity ratio decreases the ability of a slab to penetrate through the 670 km discontinuity. Stiffness of the slab decreases the possibility of the downgoing slab to enter the lower highly viscous layer. An increase in trench migration, in the range of observed rates, decreases the dip angle and the ability of a slab to penetrate into the lower mantle. In our models we could observe a strong sensitivity of slab structure to even small trench migration rates (1 cm/yr). Models of higher Rayleigh number (10^7) were dominated by a strongly time-dependent behaviour. Phases of straight mantle penetration and those of a flattened slab structure changed episodically. We conclude that time-dependence and the individual tectonic setting of subduction zones can provide a great variety of subduction related seismic anomalies. Finally, the conversion from our model temperature distribution to seismic P-wave velocities shows good agreement with the shape of observed seismic anomalies.

In *Chapter 6* we study the age-dependence of subduction. Aging of the lithosphere is accompanied with cooling and densification due to thermal contraction. A characteristic feature related to aging of lithosphere is an increase in plate thickness. This implies that the age of the lithosphere at the time it starts to be subducted influences the subduction process. Two distinct focal depth ranges in subduction zones depending on the age of the subducted slab have been observed. In subduction zones consuming lithosphere younger than 70 Myr focal depths are not deeper than 300 km. Only subduction zones in which lithosphere older than 70-100 Myr is consumed exhibit earthquakes at 500-700 km depth. Old lithosphere is assumed to sink faster and to be colder in the interior than young lithosphere. In that fast moving downgoing slab, the temperature at its cold center may remain below a characteristic temperature T_{ch}. It is suggested that below T_{ch} olivine is not transformed to spinel down to about 600 km depth. The olivine-spinel tranformation occurs far from equilibrium which - according to a current hypothesis - may cause deep earthquakes with high energy release. When olivine crosses the equilibrium boundary at about 400 km depth at high temperatures, which is more likely for young and slow descending lithosphere, phase transformation occurs much closer to equilibrium.

For young and old lithosphere plate thickness is taken to be 55 and 100 km, which is consistent with ca. 20-30 Myr and 100 Myr old slabs, respectively. From our model results we conclude that the minimum temperature in the interior of old/thick subducting slabs is lower than of young/thin subducting lithosphere. This implies that phase transformation from olivine to spinel could take place within young slabs near equilibrium at about 400 km depth, whereas the trans-

formation could be suppressed within cold and old slabs. Thus our model results support the assumed explanation for the observed relationship between focal depth and age of subducted lithosphere.

The issue of *Chapter 7* is to investigate subduction processes formerly active at convergent plate margins. For example, studies of the tectonic history of the Carpathian orogenic belt imply that subduction ceased in middle Miocene time. Pliocene and Quaternary uplift of the Transylvanian basin and adjacent mountains are interpreted as the result of unloading as the subducted slab became detached from the overlying plate. Tomography results show high P-wave velocity anomalies beneath the East-European platform which are interpreted as detached part of the former subducted slab. Evidence for former subduction beneath southern Spain has also been given by tomographic imaging. Combination of the tomographic and tectonic inferences indicate that subduction in that region took place during at least part of the Oligocene followed by detachment in the early Miocene. Our model results show that - in general - detachment of the descending slab is likely to occur after cessation of subduction. The time period between cessation of subduction and slab detachment is with about 200 Myr much too long for low Rayleigh number models ($Ra = 10^6$). Geological and tomographic studies of the Carpathian arc and the Betic Alboran region indicate that slab detachment took place ca.10-15 Myr after subduction has ceased. However, results of higher Rayleigh number models ($Ra = 5 \cdot 10^6, 10^7$) are in better agreement with observations (15-40 Myr). Conversion of our model temperature to seismic velocity structure show that magnitudes of the seismic velocity anomaly decreases with time. Decreasing sensitivity of the seismic velocity to temperature anomalies with increasing depth may reduce the possibility to detect slab detachment by means of tomographic methods. We find that about 100 Myr after subduction has ceased a slab is hardly 'visible' anymore for seismic tomography.

In *Chapter 8* we apply our model to the Mariana and Izu Bonin subduction zones. Tomographic images have shown that the subducted slab beneath the Izu-Bonin arc is stagnant within the transition zone, whereas the slab beneath Mariana penetrates nearly vertically into the lower mantle. The difference in slab geometry might be explained by the tectonic history in that region. Paleogeographic reconstructions indicate that between about 30 to 17 Ma the Philippine plate was rotating clockwise. That could have caused a retrograde motion of the trench at the Izu-Bonin arc of ca. 7.5 cm/yr, and at the Mariana arc of about 3 cm/yr. As our results from *Chapter 5* have shown that trench migration can have a major effect on subduction zone geometry, we tested if the difference in trench migration during a period of 13 Myr could explain the observed features of the North West Pacific subduction zones. Our dynamical model, using the proposed plate tectonic scenario as input, predicts a present-day subduction zone structure which is in good agreement with the tomographic images.

CHAPTER 2

A review about the characteristics of subduction zones: observations and analysis

In this chapter, results from different fields of geophysics concerning subduction zones are summarized. While the most fundamental information comes from seismology, the combination of results from mineral physics, tectonophysics and geodynamics is also very important. The following review of these results provides the motivation and basis for our study.

2.1   Introduction

The relative motion of the lithospheric plates is generally considered to be thermally driven. Under mid-ocean ridges hot mantle material rises and is partially hydrated by melting on its way to the surface. During the process called sea-floor spreading the new formed oceanic lithosphere spreads laterally away from the ridge and is cooled continuously. Densification during cooling of the old oceanic lithosphere leads to an instable state. As this slab descends into the mantle it has an anomalous thermal and chemical character relative to the ambient mantle (*e.g. Irifune and Ringwood, 1993*).

During its descent the slab is heated by the surrounding mantle predominantly by conduction. Since conductive heating of the slab is a relatively slow process, negative buoyancy of the slab continues and allows it to sink further. Early simple plate models, regarding thermodynamic parameters reasonable for the upper mantle, indicated that large temperature contrasts between the slab and the ambient mantle should exist at depth of 700 km (*McKenzie, 1969*). With increasing depth, temperature and pressure increase to evoke chemical reactions within the slab. From seismological studies (e.g. *Anderson, 1967; Archambeau et al., 1969; Dziewonski and Anderson, 1981; Paulssen, 1988; Vidale and Benz, 1992*) and mineralogical work (e.g.*Ringwood and Major, 1970; Ito and Takahashi, 1989; Akaogi et al., 1989; Akaogi and Ito, 1993*) it is generally agreed that there are at least two major phase transitions: Near 400 km depth an exothermic phase transition occurs from α-olivine ($(Mg, Fe)_2 SiO_4$) to the modified β-spinel structure of olivine indicated by an increase of seismic velocities of about 5%. Near 670

km again seismic velocities increase by about 6% consistent with the endothermic phase change from spinel-structured olivine ($(Mg, Fe)_2SiO_4$) into perovskite ($(Mg, Fe)SiO_3$) plus magnesiowüstite ($(Mg, Fe)O$). Temperature within the slab is lower than in the ambient mantle which causes different phase equilibria. At the 400 km discontinuity the phase boundary is elevated within the cold descending lithosphere resulting in a downward body force, which contributes to the negative buoyancy force of the slab (*Turcotte and Schubert, 1971; Schubert et al., 1975*). At the 670 km transition zone a phase change occurs within the slab at greater depth than in the surrounding mantle due to its cooler temperature which introduces a buoyancy force that counteracts penetration of the slab (*Schubert et al., 1975*). Locally elevated and depressed phase boundaries beneath subduction zones near a depth of 400 and 670 km, respectively, have been detected by seismic studies (*Vidale and Benz, 1992; Wicks and Richards, 1993*).

Two other characteristics have been observed in subduction zones: First, internal compressional stresses are build up in the deep-focus zone of the slab oriented in down-dip direction (*Isacks and Molnar, 1971; Richter, 1979; Vassiliou et al., 1984*); and second, seismic activity terminates at a depth of about 700 km (*Richter, 1979; Isacks and Molnar, 1971*). This was originally considered to support non-penetration of slabs which was compatible with the idea of layered mantle convection. On the other hand seismological studies have shown that seismic anomalies associated with subducted lithosphere exist several hundreds of kilometers below the 670 km discontinuity (e.g. *Creager and Jordan, 1986; Van der Hilst et al., 1991*). Thus, it is of great importance to understand how the subduction process is linked to mantle convection processes. Different geophysical disciplines have had different interpretations which are in favour or against deep mantle penetration of subducting slabs. Here we will give a brief summary of some influential work and recent studies. For more information on the fate of subducting slabs the reader is referred to the review articles of *Silver et al. (1988), Jordan et al. (1989)*, and *Lay (1994)*. First, an overview is given of seismological results/observations. Of course, the observed data must undergo numerical procedures. Next, we discuss the correlation between the geoid and subduction zones. This is followed by a review of current plate motions at convergent plate margins. We then discuss the interaction between the descending slab and the Earth's mantle. Finally, the reasons for our choice of a numerical model based on the observations and modelling results are given.

2.2   Seismological constraints on the structure of descending slabs

Most of information about the evolution of subducting slabs has come from seismology which uses three major sources of information: Firstly, intermediate and deep earthquakes are identified by their very presence with the location of de-

cending oceanic lithosphere. Second, the focal mechanism of deep earthquakes reflects the deformational nature of the descending slab. And third, probably most promising, seismic waves propagated through the area of subduction zones give information about the deep structure.

2.2.1 Constraints inferred from seismic activity

In the 1960's it was recognized that intermediate and deep focus earthquakes occur in regions where cold lithospheric plates descend into the mantle (e.g. *Isacks et al., 1968*). These zones of seismic activity, known as Wadati-Benioff zones, reflect the area where physical conditions allow earthquakes to occur. What is striking is that earthquakes occur only to a depth of about 700 km. For a long time this observation was explained with slabs which could not sink into the lower mantle. However, as a consequence of conduction of heat into the slab it is likely that mechanical weakening occurs. During its descent a depth dependent critical temperature could be exceeded, beyond which the subducted lithosphere cannot sustain the stresses necessary to generate seismic events. That would imply that the absence of seismic activity at depth greater than 700 km cannot be taken as evidence that the 670 km discontinuity acts as a barrier to subducting slabs (*Wortel, 1982; 1986*). Since the thermal assimilation depends on the thickness of the subducting slab and its descent velocity v_z the age of the subducted slab at the time when subduction has started is a significant factor for the depth of seismic activity. *Vlaar and Wortel (1976)* established the relation between the age of oceanic lithosphere at the time it started to be subducted and the maximum focal depth of the earthquakes occurring within this subducted lithosphere. Only subduction zones in which lithosphere older than 70-100 Myr is consumed reveal deep-focus earthquakes, i.e. in the depth range of 500-700 km. Subduction zones consuming lithosphere younger than 70 Myr exhibit focal depth not deeper than 300 km. However, thermal assimilation alone seems not to be sufficient to explain, for example, the effects of plate age and descent rates on earthquake depth distribution (*Kirby et al., 1991; Kirby, 1995*). Furthermore, deep slab failure could occur by transformational faulting within a wedge-shaped area of the slab, where metastable olivine exists (*Sung and Burns, 1976; Burnley et al., 1991; Kirby, 1995*). This metastable olivine is formed when olivine at temperatures below a characteristic rate T_{ch} is not transformed to spinel. Thus, in a fast moving downgoing slab, the temperature at its cold center may remain below T_{ch} even down to depth in excess of 600 km thereby depressing the olivine-spinel phase boundary which is distorted downwards. When the olivine-spinel transformation is far from the equilibrium the reaction becomes implosive. This could explain the rise in frequency of deep earthquakes toward the implosion region in the lower transition zone (*Sung and Burns, 1976*). Mineralogical results predict that metastable olivine survives to depth greater than 500 km in the cold

interior of rapidly subducting old lithosphere (*Rubie and Ross, 1994*). When
olivine crosses the equilibrium boundary at 400 km depth at temperatures higher
than 700 °C, which is more likely for young and slow descending lithosphere, phase
transformation occurs much closer to equilibrium.

The location of the earthquake hypocentres give constraints on the geometry
of the subducting slabs down to the depth they occur. For example, seismic
activity in the Tonga region suggest that the Tonga slab is buckled and imbricated
(*Giardini and Woodhouse, 1986*). Studies of the Wadati Benioff zone beneath the
Andean cordillera indicate that the subduction zone geometry of the Nazca plate
varies in dip along the trench. The subducted slab can be described as having four
segments, with each segment distinguished from its neighbours by a significant
change in dip angle (*Barazangi and Isacks, 1976; Cahill and Isacks, 1992*). The
plate is sharply flexed with southward transition from flat to 30° dipping geometries
beneath southern Peru and central Chile. The southward transition from 30° slab
dip beneath Bolivia to a nearly horizontal dip in the region of 28°S and 32°S (Chile)
appears to be gradual (*Cahill and Isacks, 1992*). The very deep seismicity (deeper
than 650 km) beneath Spain and the lack of seismic activity between 100 and 650
km depth led *Buforn et al. (1991)* to conclude that a block of lithospheric material
still sufficiently cold and rigid to generate earthquakes has been detached from
shallower parts of the downgoing slab.

2.2.2   Constraints inferred from focal mechanism

Deep earthquake seismicity does not only indicate the occurrence of strain release,
but also reveals the strain orientation at the source. The stress pattern in sub-
ducted slabs changes from predominantly down-dip extension at about 200 - 400
km to predominantly down-dip compression at about 500 - 600 km (*Isacks and
Molnar, 1971; Richter, 1979; Vassiliou et al., 1984*). The tendency of deep earth-
quake focal mechanisms to be compressional has often been interpreted to imply
that the slab meets some resistance when penetrating into the lower mantle (*e.g.
Richter, 1979*). From studies of focal mechanisms in the northwest Pacific and
Tonga-Kermadec region *Zhou (1990b)* found evidence for flattening of the com-
pressional strain axes near the bottom of the upper mantle beneath the Izu-Bonin
and Tonga arcs. From his results he concluded that the slabs could be contorted or
even subhorizontal at the base of the upper mantle under Japan, Izu-Bonin, Ker-
mdadec and parts of the Tonga arc. However, there is no evidence for contortion
or flattening of slabs beneath the Mariana arc. *Vassiliou et al. (1984)* used simple
models of subducting slabs to explain the variation of seismicity with depth and
the orientation of stress axes of deep and intermediate earthquakes. Models that
matched the observed seismicity and stress required a barrier to flow at the 670 km
discontinuity. They suggested that such a barrier could be an increase in viscosity

by at least one order of magnitude or a chemical discontinuity.

2.2.3   Constraints inferred from seismic velocity structure

Slabs have other seismological properties that can be and have been used to study slab penetration into the lower mantle. Since slabs are thermally and chemically distinct from the ambient mantle, seismic waves transmitted through the slab cause amplitude and travel time anomalies. Basically, four methods are utilized to resolve the problem of detecting aseismic descended slabs: (i) travel-time and amplitude anomalies from individual events are studied; (ii) waveform distortions produced by gradients in seismic velocity structure near the deep slab are investigated; (iii) the mantle around deep earthquakes is imaged by three-dimensional tomography; and (iv) the structure and topography of the mantle discontinuity is analysed.

(i) Travel-time modelling
The fundamental idea for travel-time modelling is that the cold descended slabs should have higher elastic velocities than the surrounding mantle material. Waves following longer path lengths in the slab incur relatively early arrivals compared to waves following shorter path lengths through the slab. Seismic velocities of slabs in the transition zone are about 5 % faster than those of the ambient mantle material.

The residual sphere method, as first introduced by *Davies and McKenzie (1969)*, computes travel-time anomalies for events at different locations in the same slab relative to standard travel time tables. Results inferred from the analysis of travel time residuals for deep focus events indicated the existence of aseismic extension of subducted slabs to a depth several hundred kilometers below the 650 km seismic discontinuity, as for example, beneath the Kuril-Kamchatka, Japan, or Mariana subduction region (*Jordan, 1977; Creager and Jordan, 1984, 1986*). *Okano and Suetsugu (1992)* applied a differential residual technique which suppresses effects of deep mantle and near station lateral heterogeneities - effects, which could have been the source of erroneous results of the former residual analysis. They interpreted their results as indicating that the Kuril slab is penetrating into the lower mantle but the Mariana slab is not. The same approach was applied to the northeastern Japan arc from which it was concluded that its slab enters the lower mantle. There were some attempts to explain the observations by means other than slab penetration - such as lower mantle heterogeneities. For example, heterogeneities of about 2% velocity contrast have been detected beneath North Brazil, Venezuela, and the Carribean at depth between 1000 and 2700 km with a lateral dimension of 1000 - 2000 km (*Lay, 1983*). Another explanation could be thermal coupling between upper and lower mantle (*Anderson, 1990; Vidale and Garcia-Gonzalez, 1988*). However, the success of the slab interpretation in explaining much of the size and character of the travel-time anomaly suggest that

slab-penetration is likely.

(ii) Waveform anomalies

Independent support for the lower mantle slab penetration comes from observed waveform anomalies. In theory the high-velocity heterogeneity of slabs should evoke complex defraction, defocusing and multipathing effects such as arrival of a body-wave phase by more than one path (*Vidale, 1987; Cormier, 1989; Vidale et al., 1991*). The presence of slab-induced multipathing from events near a depth of 600 km under the Kuril arc led *Silver and Chan (1986)* to conclude that there is slab penetration beyond the 650 km discontinuity, at least 300 - 400 km into the lower mantle beneath the Sea of Okhotsk.

(iii) Seismic tomography

The studies mentioned above are most sensitive to slab properties near the earthquake epicentre down to a depth of about 1000 km (*Creager and Jordan, 1986*). If slabs continue several hundreds of kilometers below their seismic activity depth other sources of information might be helpful to track the descent of the slab. The recent three-dimensional tomographic images of the mantle appear to be an informative tool. *Aki and Lee (1976)* and *Aki et al. (1977)* presented fundamentals of the tomographic method which has been expanded to treat enormously increasing data sets and model sizes (*Spakman and Nolet, 1988*).

Seismic tomography has been applied to the Mediterranean region (*Spakman et al., 1988, 1993; Spakman, 1990, 1991*), to the northwest Pacific subduction zones (*Spakman et al., 1989; Zhou and Clayton, 1990; van der Hilst et al., 1991,1993; Fukao et al., 1992*), to the Java region (*Fukao et al., 1992; Widiyantoro and van der Hilst, 1996*), to the southwest Pacific subduction zones (*Zhou, 1990a; Van der Hilst, 1995*), and to Central America and the Carribean (*van der Hilst and Spakman, 1989*).

As an example, Figure 2.1 displays a roughly South to North cross section through the Aegean mantle revealed by tomographic imaging from *Spakman et al. (1993)*. The top panel gives a regional map for reference. Positive velocity anomalies correspond to high velocity regions. The anomalies are given in percentages of the ambient mantle velocity given by a radially symmetric P-wave velocity model, which is appropriate for the European Mediterranean mantle (see *Spakman et al., 1993*). Dots in the cross section and the map represent earthquakes. The northward dipping positive anomaly structure can be interpreted as the image of the subducting African plate.

The major results of the tomography studies for the above mentioned subduction zones are the following: High velocity anomalies below Kamchatka-Kuril indicate vertical extension of a subducted slab to a depth of about 1100 km (*van der Hilst et al., 1991, 1993*). The southern Kuril slab appears to be flattened and extended horizontally above the 660 km discontinuity (*van der Hilst et al., 1991,*
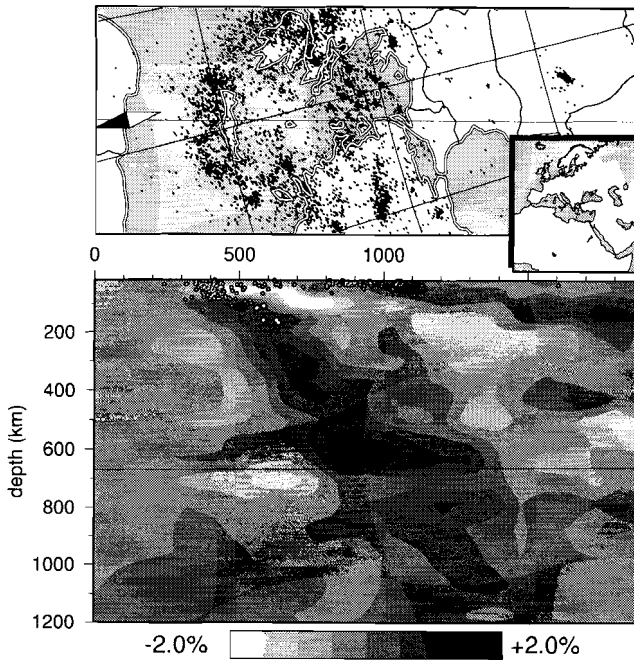
Figure 2.1 *Tomographic image of the Aegean mantle revealed by Spakman et al. (1993; EUR89B). Top panel shows a map for reference. Positive velocity anomalies correspond to high velocity regions. The anomalies are given in percentages of the ambient mantle velocity given by a radially symmetric P-wave velocity model, which is appropriate for the European Mediterranean mantle (see Spakman et al., 1993). Dots in the cross section and the map represent earthquakes. The northward dipping positive anomaly structure can be interpreted as the image of the subducting African plate.*

1993; Fukao et al., 1992). The subducted slab below central Japan seems to be thickened and as well flattened at 660 km depth (*van der Hilst et al., 1991, 1993; Fukao et al., 1992*). Tomographic images of the mantle region beneath Central Izu Bonin indicate flattening of the subducted slab above 660 km, while fast velocity slab structure at the Marianas arc appears to penetrate vertically into the lower mantle down to a depth of about 1200 km (*van der Hilst et al., 1991, 1993; Fukao et al., 1992*). The structure of lithospheric slab beneath the Sunda arc, Indonesia, inferred by tomographic imaging seem to extend down to a depth of 1500 km (*Widiyantoro and van der Hilst, 1996*). *Zhou (1990a)* found that the Tonga slab appears to end at about 550 km depth, but is underlain by a fast band at about 750

- 1000 km depths. The fast slab-like anomaly beneath the (northern) Kermadec arc tends to flatten to subhorizontal near the bottom of the upper mantle (*Zhou, 1990a*). These results could be confirmed recently by *Van der Hilst (1995)*: his tomographic images show that in the north of the Tonga trench the slab deflects in the transition zone (between 400-700km) before continuing into the lower mantle. Beneath the south Kermadec region penetration into the lower mantle occurs without a kink (*Van der Hilst, 1995*).

In addition to small scale structures of different subduction zones large scale tomographic images have also been well established. High-velocity anomalies of the lower mantle below the circum Pacific region have been detected (*Dziewonski and Woodhouse, 1987; Su and Dziewonski, 1991*). However, a direct connection between these features and slab anomalies has not been proved yet. It is particular difficult to distinguish between aseismic extension of subducted slabs and downwellings from thermally-coupled layered systems in large-scale tomography (*Lay, 1994*).

(iv) Topography of the 660-discontinuity
Further insight in deep slab structure comes from analysing the topography of the 660 km discontinuity. As the phase transformation from spinel to perovskite near 660 km is strongly endothermic, it is deflected downwards in cold downwellings (*e.g. Turcotte and Schubert, 1971*). It is assumed that the deflection could be detected. Actually, depressions of the phase boundary of approximatly 60 km have been revealed under Izu-Bonin (*Wicks and Richards, 1993*), or up to 30 km under Mariana, Izu-Bonin, Tonga and South America (*Vidale and Benz, 1992*). Topography of the 660 km discontinuity in the order of 20 km was found in regions under Indonesia, Australia, the western and central Pacific (*Revenaugh and Jordan, 1991*). Global mapping of the 660 km discontinuity performed by *Shearer and Masters (1992)* indicate depth variations of up to 30 km and suggest a correlation between regional depressions in this discontinuity and subduction zones. They found, for example, a broad depressed structure extending at least 1000 km west of southern Kuril to Izu-Bonin arcs. This feature is consistent with the tomographic images showing a flattened velocity anomaly structure in that region (e.g. *van der Hilst et al. 1991, 1993*).

2.3   Subduction zones and the geoid

Additional information on slab penetration comes from analysing geoid anomalies which are the result of lateral density variations (e.g. *Hager, 1984*). Temperature variations, phase changes, dynamic topography at the surface and the core-mantle boundary, and changes in composition provide density anomalies. Since subducted lithosphere creates positive density anomalies in the mantle, subducting

slabs become substantial, even dominant, contributions to geoid undulations (e.g. *McAdoo, 1981*). The intermediate wavelength geoid shows an excellent correlation with the location of subducted slabs. (*McAdoo, 1981; Hager, 1984*). The excess density of the cold descending slab relative to the mantle results in a strong gravity anomaly and therefore the correlation with a positive geoid signal seems likely. However, subducted slabs also cause depressions at the Earth's surface - i.e. deep ocean trenches - which amount to negative mass anomalies. Simple models of a slab in a mantle of uniform viscosity predict a net negative geoid variation (*Davies and Richards, 1992*). *Hager* (1984) concluded that the observation of geoid highs over subduction zones requires an effective mantle viscosity that increases with depth. A factor of at least 30 is required for a Newtonian, radially symmetric viscosity profile. Large mass anomalies in the vicinity of subduction zones indicate slab penetration into the lower mantle, because the density contrasts of only the seismically active parts of subducted slabs are not sufficient for the observed geoid anomalies (*Hager, 1984*). Geoid modelling indicates that substantial negative mass anomalies caused by slabs stagnant in the transition zone would cause a signal inconsistent with observations (*King and Hager, 1994*). The observed geoid however does not reveal the finer details of the slab geometry (*McAdoo, 1981*).

2.4 Current plate motions

Plate motion is a direct visible expression for the geodynamical processes in the Earth's mantle. Thus, plate velocities at the convergent plate boundaries are important for the analysis of the evolution of subduction zones. The plate motions are not only a response to the dynamics of the upper mantle, but are also coupled to the motion and behaviour of the downgoing slab. The most recent global model of relative plate motions is NUVEL-1A (*DeMets et al., 1994*) which is the modified plate motion model NUVEL-1 (*DeMets et al., 1990*) with an updated geomagnetic reversal time scale. *DeMets et al. (1994)* compared the geomagnetic timescale of *Harland et al. (1982)*, which was used for NUVEL-1, with the more recent one of *Hilgen (1991)*. They showed that ages for the geomagnetic reversals used in NUVEL-1 are systematically too young. Therefore angular speeds in NUVEL-1 are systematically too fast. Multiplying all NUVEL-1 angular velocities by a factor α of 0.9562 compensates this systematic error. NUVEL-1/NUVEL-1A differ significantly from plate velocity models P071 (*Chase, 1978*) and RM2 (*Minster and Jordan, 1978*). P071, RM2, and NUVEL-1 are incorporated respectively into the global models of plate velocities relative to the hotspots P073 (*Chase, 1978*), AM1-2 (*Minster and Jordan, 1978*), and HS2-NUVEL1 (*Gripp and Gordon, 1990*).

Table 2.1 *Current plate velocities at subduction zones For plate abbreviations, their boundaries, and location of subduction zones see Figure 2.2. Lat and lon is the latidude and longitude, respectively, of the reference position of each subduction zone taken from Jarrard (1986). v_o, v_u, and $v_c^{\ddagger}$ are based on the global model of absolute plate motions HS2-NUVEL1. $v_c^{\ddagger}$ is calculated from Euler vectors of the model of relative plate motions NUVEL-1A. For the meaning of the velocities v_o, v_u, and v_c see also Figure 2.3 .*

	subduction zone	position lat	lon	over-riding plate	under-thrusting plate	v_o mm/yr	v_u mm/yr	$v_c^{\ddagger}$ mm/yr	$v_c^{\ddagger}$ mm/yr
1	Aegean	36	22	eu	af	-9.60	-4.23	5.37	4.38
2	Sumatra	-2	98	eu	au	-2.74	52.08	54.82	54.71
3	Java	-11	112	eu	au	4.83	77.14	72.30	72.96
4	Ryukyu	25	128	eu	ph	9.92	66.19	56.27	-
5	SW Japan	33	135	eu	ph	9.43	47.06	37.63	-
6	New Zealand	-40	178	au	pa	50.87	85.12	34.25	33.57
7	Kermadec	-34	-178	au	pa	38.57	88.95	50.39	49.59
8	Tonga	-22	-174	au	pa	27.07	98.60	71.53	70.57
9	New Hebrides	-17	167	pa	au	-64.86	18.62	83.48	82.68
10	Solomon	-7	155	pa	au	-20.07	62.52	82.59	82.07
11	Marianas	17	148	ph	pa	63.65	94.79	31.14	-
12	Izu Bonin	30	143	ph	pa	37.30	87.46	50.16	-
13	NE Japan	39	144	eu	pa	7.15	96.49	89.34	89.34
14	Kurile	45	152	na	pa	10.11	87.44	77.33	76.89
15	Kamchatka	53	162	na	pa	7.09	83.23	76.14	75.64
16	Central Aleutians	50.5	180	na	pa	-2.24	51.95	54.19	53.88
17	Alaska Peninsula	60	-152	na	pa	3.91	35.28	31.36	31.10
18	Alaska	62	-149	na	pa	-3.77	47.81	51.58	51.20
19	Cascades	45	-125.5	na	jf	-16.70	18.04	34.74	-
20	SW Mexico	17	-103	na	co	-21.00	28.35	49.35	49.30
21	SE Mexico	15.5	-97	na	co	-19.72	42.61	62.33	62.35
22	Middle America	12.5	-91	ca	co	-13.82	56.70	70.52	71.09
23	Lesser Antilles	16	-59	ca	na	17.78	29.97	12.19	10.88
24	Columbia	5	-78	sa	nz	-28.98	29.01	57.99	57.05
25	Ecuador	-2	-81	sa	nz	-31.29	34.47	65.76	64.69
26	Peru	-10	-80	sa	nz	-30.52	36.50	67.02	65.94
27	North Chile	-21	-71	sa	nz	-33.62	45.13	78.75	77.47
28	Central Chile	-30	-72	sa	nz	-31.36	44.01	75.36	74.15
29	South Chile	-38	-74	sa	nz	-29.05	43.69	72.74	71.57
30	Tierra del Fuego	-49	-77	sa	an	-28.68	-8.79	19.90	20.06

The angular velocities of the latter model have to be corrected by the factor α similar to the revisions of NUVEL-1A with respect to the geomagnetic scale. The plate motions are specified by Euler vectors which give the angular velocity vectors describing the motion between two plates. Table 2.1 lists absolute and relative
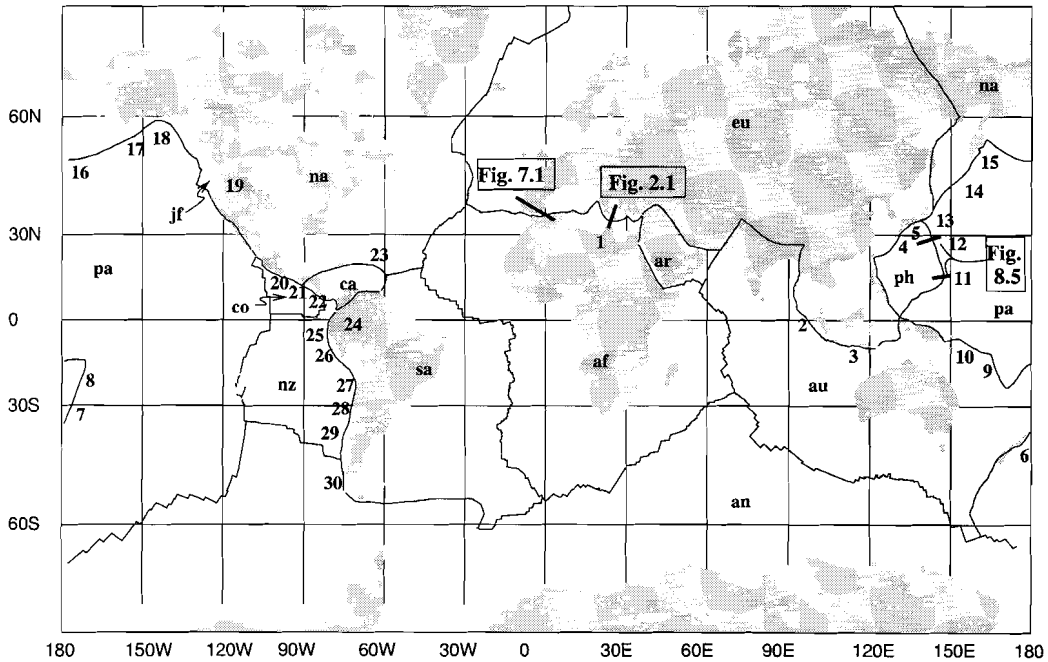
Figure 2.2 *Mercator projection of present continental outlines and major plate boundaries. Subduction zones listed in Table 2.1 are indicated by the appropriate numbers. Thick lines indicate the areas of which a tomographic image is shown in this thesis. Figure 2.1 shows a cross section through the Hellenic arc, Figure 7.1 of the Betic Alboran region, and Figure 8.5 of the Izu-Bonin and Mariana subduction zone. Plate abbreviations are: af, Africa; an, Antarctica; ar, Arabia; au, Australia; ca, Caribbean; co, Cocos; eu, Eurasia; jf, Juan de Fuca; na, North America; nz, Nazca; pa, Pacific; ph, Philippine; sa, South America.*

plate motions at 30 subduction zones based on the HS2-NUVEL1 Euler vectors and the fixed hotspot hypothesis (*Gripp and Gordon, 1990*), and NUVEL-1A Euler vectors, respectively. Major plate boundaries and the location of the subduction zones are shown in Figure 2.2. The reference position (latitude - *lat*, longitude -*lon* in Table 2.1) and their trench azimuths are from *Jarrard (1986)*. The angular velocities had been corrected by the same calibration factor $\alpha = 0.9562$ which remedies the systematic error of angular speeds in NUVEL-1 (*DeMets et al., 1994*). The velocities of the overriding plate v_o, of the underthrusting plate v_u, and the convergence velocity v_c^t and v_c^t are projections perpendicular to the trench. As with convergence rates, the overriding plate is defined as the major plate behind the arc, not the forearc region (see Figure 2.3.). The sign convention is that positive

absolute motions are toward the overriding plate. Both the African Plate and the Antarctican Plate seem to move away from its trench along the Aegean and the Tierra del Fuego subduction zone, respectively. The speed, in both cases less than 10 mm/yr, is slow enough that within the error boundaries a trenchward motion is permitted (*Gripp and Gordon, 1990*). v_c^t is based on HS2-NUVEL1 Euler vectors, whereas v_c^t is derived from NUVEL-1A angular velocities of pairs of plates sharing a boundary. Data for v_c^t are missing for subduction zones at the boundary of the Eurasian and the Philippine plate, of the Philippine and Pacific plate, and of the Juan de Fuca and the North American plate, because the authors do not list Euler vectors for these pairs of plates (*DeMets et al., 1994*). With the exception of the Aegean and the Lesser Antilles subduction zone - both of which have convergence velocities less than 13 mm/yr - the convergence velocities derived from different data sets (one for the absolute velocities, one for the relative velocities) differ by maximum 2% from each other.
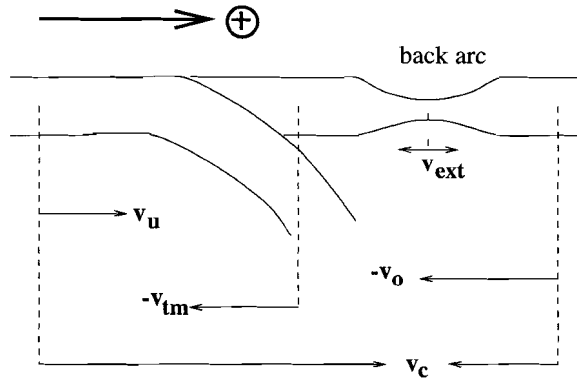

Figure 2.3 *Scheme of subduction zone geometry. v_u, v_o, v_c are the velocity of the underthrusting, the overriding plate, and the convergence velocity respectively. v_{ext} is the rate of extension in the back arc. As long as no back arc extension occurs the trench migration rate v_{tm} equals v_o. As indicated by the arrow at the top the sign convention is that positive absolute motions are toward the overriding plate. Strictly speaking, arrows of v_o and v_{tm} point in the direction of $-v_o$ and $-v_{tm}$, respectively.*

This serves as a test for transforming the Euler vectors to v_o, v_u, and v_c including all position datas of the subduction zones correctly. Note that the plate velocities given in Table 2.1 are present day rates. To interpret the seismological results in terms of the evolution of descending slabs plate motions of the past (in the order of 10 Myr) must also be taken into account. This is particularly important in the case of 'fossil' subduction zones, zones where the subduction process has ceased. For

example, evidence for former subduction beneath the Carpathian arc and beneath Southern Spain has been given by tomographic imaging (*Spakman, 1990; Blanco and Spakman, 1993*).

What matters for the correlation between plate velocities and the behaviour of subducting slabs are not only the plate velocities with respect to some absolute reference frame (e.g. the hotspot frame), but also their velocities with respect to the mantle flow beneath. *Ricard et al. (1991)* proposed a global eastward mantle flow in the order of 1cm/yr which can be important for the interpretation of slab geometry. Relative motion between lithosphere and mantle flow can explain structural differences between east and west dipping subduction zones: West dipping subduction zones (e.g. Apennines, Eastern Carpathians) are characterized by high dip of the subducting slab, small elevation of the chain and a deep foreland basin. East dipping subduction zones (e.g. Western Alps, Dinarides) have minor dip angle, greater elevation, and a shallow foredeep basin (*Doglioni et al., 1991*).

2.5   Slab-mantle interaction

Images of the seismic velocity distribution of the mantle interior provide an instantaneous view of time-dependent structures which must be interpreted in the context of dynamics and possible behaviour. Hence, time-dependent modelling is an important method to understand the long-term evolution of the subduction process. Since increasingly realistic parameter ranges have been determined great advances in numerical calculations have been made. A variety of possible influences on the dynamics of subducting slabs have been studied. There are three major factors which are critical in the long-term evolution of the downgoing slab: First, plate velocities, particularly the rate of trench migration (roll back) appears to have an important effect on slab behaviour. Second, the transition zones in the mantle at about 400 and 650 km depth affect the descent of the slabs, and third, the stratification of the lithosphere itself plays a role in slab behaviour. In the next three paragraphs a summary about the relationship between each of these factors and slab behaviour is presented.

2.5.1   Effects of trench migration

As the motion of the lithospheric plates is irregular and their generation and consumption is distributed at uneven rates there is lateral migration of subduction zones and descending slabs (*Garfunkel et al., 1986*). Absolute plate motions indicate that in general lateral trench migration is backward relative to the motion of the plate to which the subducting slab is attached. Two types of mechanism of trench migration have to be distinguished. First, the slab sinks under its own

weight so that the hinge (trench) moves backwards. This process is referred to as roll back. Second, when the overriding plate moves toward the underthrusting one, the latter is forced by the former to move backwards. Both cases lead to a net horizontal motion of the trench relative to a fixed reference frame (e.g. the hotspot frame).
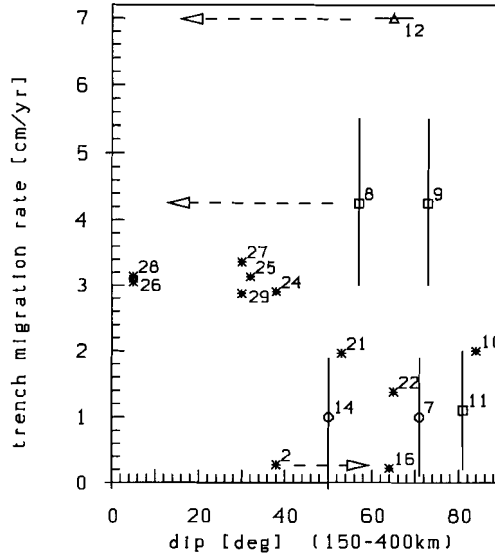

Figure 2.4 *Slab dip versus the rate of retrograde motion perpendicular to the trench. Numbers indicate the subduction zones given in Table 2.1. Dip angles are from Jarrard (1986). Trench migration rates from the HS2-NUVEL1 model (Gripp and Gordon, 1990; revised by DeMets et al. (1994)) are indicated by asterisks, those from Griffiths et al. (1995) are indicated by circles and squares. The squares indicate subduction zones where active backarc basins are present. The extremely high rate of migration of the Izu Bonin trench (triangle) has taken place 30-17 Myr BP (van der Hilst and Seno, 1993). The dashed arrow indicates that slab dip converges towards 0° at the transition zone (van der Hilst et al., 1991) as is the case for the slab beneath northern Tonga (point # 8; Van der Hilst, 1995). The small dip angle of the slab beneath Sumatra pointed out by the arrow next to point # 2 could have been reduced by dynamical rebound (Wortel and Spakman, 1992) after slab detachment (Widiyantoro and Van der Hilst, 1996).*

With our sign convention, overriding plates with negative velocities v_o listed

in Table 2.1 move toward the subducting plate and trench migration is obvious. Thus, the sign of (backward) trench migration rates is negative. In the following, an increase in trench migration rate means an increase in magnitude. The magnitudes of the retrograde movements are up to 4 cm/yr (see also *Jarrard, 1986; Garfunkel et al., 1986; Van der Hilst and Seno, 1993; Griffiths et al, 1995*). At the Izu Bonin subduction zone extremely high rates of retrograde motion of about 7 cm/yr have taken place 30-17 Myr BP (*van der Hilst and Seno, 1993*). Figure 2.4 summarizes the relationship between trench migration rate (positive magnitudes) and dip angle for 17 subduction zones. A clear trend of increase in dip angle with decreasing rate of trench migration can be seen. Most of the rates of trench migration are taken from the HS2-NUVEL1 model from *Gripp and Gordon (1990)* as revised by *DeMets et al. (1994)* (i.e. velocities v_o as listed in Table 2.1). As backarc extension is not included in the rates v_o, other data has been taken from *Griffiths et al. (1995), van der Hilst and Seno (1993)*. Dip angles are from *Jarrard (1986)*. Squares indicate subduction zones where active backarc basins are present. The extremely high rate of migration of the Izu Bonin trench (triangle) which has taken place in the past correlates well with a slab dip of nearly 0° at the transition zone, whereas the dip angle between 150 and 400 km depth is about 65°. The small dip is indicated in Figure 2.4 by the dashed arrow. *Van der Hilst (1995)* showed that beneath northern Tonga the dip angle of the slab reduces to almost zero in the transition zone (similar to Izu Bonin), which is indicated by a dashed arrow in Figure 2.4 next to point # 8. The relatively small dip of the Sumatra slab (point # 2 in Figure 2.4) could be anomalous due to a possible dynamic rebound (*Wortel and Spakman, 1992*) after detachment of the deeper part of the slab (*Widiyantoro and Van der Hilst, 1996*). The dip angle is likely to be larger if slab detachment and consequently dynamical rebound has not occurred. The possible larger dip angle is shown in Figure 2.4 by an arrow next to subduction zone number #2. If the new positions within the diagram are taken into account the relationship depicted in Figure 2.4 - decrease in dip angle with increase in trench migration rate - becomes even clearer.

Laboratory experiments (*Kincaid and Olson, 1987; Griffiths et al., 1995; Guillou-Frottier et al., 1995*) and numerical modelling (*Tao and O'Connell, 1992; Zhong and Gurnis, 1995; Christensen, 1996*) showed that the subduction process is sensitive to trench migration. Laboratory experiments indicate that, if the lateral migration of the trench is sufficiently fast, subducted slabs can stagnate above the discontinuity presented by a step increase in viscosity and density (*Kincaid and Olson, 1987*). On the contrary, when the trench is stationary with respect to the mantle below, and the ratio between lower to upper mantle density is not too large, it is likely that the slab buckles near the transition zone and penetrates into the lower mantle (*Kincaid and Olson, 1987; Gurnis and Hager, 1988*). *Van der Hilst and Seno (1993)* argue that differences in the tectonic evolution, specifically

the amount and rates of trench migration, in the Western Pacific can explain why the subducted oceanic lithosphere beneath the Izu Bonin arc is stagnant at the transition zone but penetrates into the lower mantle beneath the Mariana arc. Laboratory experiments recently performed provided considerable insight in the role of trench migration on the subduction process (*Griffiths et al., 1995; Guillou-Frottier et al., 1995*). In both kinds of experiments the 670 km disontinuity was presented by a viscosity and density increase. *Christensen (1996)* found that when trench retreat is faster than 2 - 4 cm/yr the subducting slab which encounters a phase boundary is flattened above the transition zone. At slower rates the slab is able to penetrate into the lower mantle. These results indicate that moderate changes in trench migration rate can lead to different slab morphology as observed by seismic studies.

2.5.2   Transition zones of the mantle

The two major phase transitions from olivine to the spinel structure at about 400 km depth and from γ-spinel structure to the assemblage of perovskite plus magnesiowüstite at about 670 km depth are primarily a result of the large increase in pressure with depth (*Akaogi et al., 1989*). For the expected mantle temperatures these transitions occur at pressures consistent with 400 and 670 km depth which is in agreement with the depth of observed seismic velocity discontinuities (e.g. *Bass and Anderson, 1984; Paulssen, 1988*). In the descending slab the temperature profiles and depth of the phase transitions are different from those in the sourrounding mantle. This is because the subducted slab remains cooler than the ambient mantle material, possibly as far down as the lower mantle (e.g. *Turcotte and Schubert, 1971; Schubert et al., 1975*). The nature of the discontinuities is still debated. One model proposes that the transition zone occurs in an isochemical medium (e.g. *Ito and Takahashi, 1989*), another favours an abrupt change in chemistry (e.g. *Bass and Anderson, 1984; Funamori and Yagi, 1993*). Another feature linked to the 670 km discontinuity is an increase in viscosity (e.g. *Hager and Richards, 1989*). The effects of the two transition zones, of a chemical, and a viscous layered mantle on the descending slab is discussed in the following section.
The 400 km discontinuity
Basically, at the exothermic phase change ($dp/dT > 0$) (400 km discontinuity) the transition occurs at lower pressure, hence shallower depth, within the downgoing slab. The elevated region of the denser phase within the slab evokes a gravitational force pulling the slab downward. However, *Sung and Burns (1976)* proposed that there could be a characteristic temperature T_{ch} below which the olivine is not transformed to spinel, but remains as metastable olivine possibly down to about 600 km depth. Thus, in this wedge-shaped region of metastable olivine within the coldest part of the sinking slab density would be less than that of the surrounding

mantle. Density excess - relative to mantle material - in the outer warmer parts of the slab, where the α - β-transition has already been occurred, could then partly be compensated. Numerical results of the effect of the exothermic phase transition on slab and plume penetration by near 400 km depth are controversial. While *Zhao et al. (1992)* and *Steinbach and Yuen (1992)* conclude that this phase change increases the overall prospensity to layering, *Tackley et al. (1994)* and *Solheim and Peltier (1994)* conclude that the overall degree of layering is reduced.

The 670 km discontinuity

The nature of the phase transition at about 670 km depth is endothermic ($dp/dT <$ 0; e.g. *Akaogi and Ito, 1993*). Depression of the low-density phase occurs and its buoyancy opposes the descent of the slab (*Schubert et al., 1975; Ito and Sato, 1992*). First and detailed numerical calculations including an endothermic phase transition have been done by *Christensen and Yuen (1984, 1985)*. They conclude that slab deflection by a phase change would require a negative Clapeyron slope in excess of -6 MPa/K, which they viewed as unlikely. Recent work has demonstrated that the Clapeyron slope varies from -2.8 to -4 MPa/K (*Ito and Takahashi, 1989; Ito et al., 1990; Akaogi and Ito, 1993*). Significant studies treating numerical calculations in a spherical, axisymmetric geometry of phase change modulated mantle are from *Machetel and Weber (1991), Peltier and Solheim (1992)*, and *Solheim and Peltier (1994)*. The result of these studies show intermittent layered convection which is characterized by accumulation of cold slab material above the 660 km discontinuity which catastrophically avalanches into the lower mantle. This feature is compatible with the intermittent stratification found by *Christensen and Yuen (1984)*.

Since the early studies of *Christensen and Yuen (1984)* more complete models have been applied. Three-dimensionality, higher Rayleigh numbers, and depth- and temperature-dependent parameters have been included. In three-dimensional geometry (*Tackley et al., 1993, 1994; Honda et al., 1993a,b; Yuen et al., 1994*) descending avalanches occur in cylindrical downwellings, a geometry which is not possible to model using two-dimensional geometry. These three dimensional simulations do not include temperature-dependent viscosity and surface plates, both of which are assumed to strongly influence the style of convection. On the one hand it is suggested that the stiffness of the slab will affect the ability of the phase transition to impede its descent (*Lay, 1994; Tackley, 1995*). On the other hand *Zhong and Gurnis (1995)* found in a numerical model study that an increase in slab viscosity by a factor of 10 relative to the transition zone decreases the ability of penetration and the slab needs more time to sink. Early studies on slabs simulated the interaction of a high viscosity slab (with non-linear temperature-dependent rheology) with a combined phase transition and a chemical discontinuity (*Christensen and Yuen, 1984*). Comparison of these model runs with corresponding isoviscous model runs implied that the critical Clapeyron slope

which is required to prevent the slabs from entering the lower mantle is largely insensitive to the viscosity contrast (*Christensen and Yuen, 1985*). Recent results show that highly viscous slabs with Newtonian rheology penetrate the transition zone more easily than isoviscous slabs (*Zhong and Gurnis, 1994*). In these models the descending slabs were restricted to sink at the end of the two dimensional model domain. An increase of the aspect ratio, hence lengthening the subducting plate, increased the slab's ability to penetrate the transition zone.

An increase in Rayleigh number increases the degree of layering (*Christensen and Yuen, 1985; Zhao et al., 1992; Yuen et al., 1994*). An increase in internal heating as well as the decrease of the thermal expansivity (*Zhao et al., 1992*) enhances the prospensity to layered convection (*Zhao et al., 1992; Solheim and Peltier, 1994*).

Chemical and viscous layering

Results from mineral physics experiments on silicate, perovskite, and magnesiowüstite have demonstrated that the maximum density contrast between upper and lower mantle is about 5 %, from which it was suggested that the upper and lower mantle are compositionally distinct (e.g. *Knittle et al., 1986; Jeanloz and Knittle, 1989; Stixrude et al., 1992*). Estimates are still flawed because of uncertainty in the temperature- and pressure-dependence of the thermal expansion coefficient. While experimental determination of the thermal expansivity for mantle substances suggest a decrease in expansivity by a factor between 5 and 10 across the mantle (*Chopelas and Böhler, 1989, 1992; Chopelas, 1990*), recent measurements at simultaneous high temperature and high pressure suggest less decrease of the thermal expansion coefficient with depth (*Funamori and Yagi, 1993*). Consequently, the Anderson-Grüneisen parameter, which describes the volume dependence of the thermal expansivity, would become much smaller than expected, from which the authors conclude that the mantle might be compositionally layered. Also, comparison of laboratory elasticity data with seismic velocity profiles favour a chemical stratification, because in a homogeneous medium the transition zone would spread in a wider depth range than the observed seismic velocity dicontinuities (*Bass and Anderson, 1984*). However, high-pressure transformation in the system $Mg_2SiO_4 - Fe_2SiO_4$ demonstrated that a chemical change may not be necessary to account for the sharpness of the discontinuity (*Ito and Takahashi, 1989*).

Numerical experiments of *Christensen and Yuen (1984)* showed that a 5% density contrast would be sufficient to impede slabs from penetration into the lower mantle. A density contrast between 2 and 5 % would allow slabs to impinge through the 660 km dicontinuity partially, and an increase in density less than 2 % - which is supposed to be (from mineral physics) at the lower end - would be no resistance to slabs at all. *Kincaid and Olson (1987)* could establish these results with laboratory experiments. Penetrative convection, in which a density

contrast due to chemical layering is 2 % or less, could explain a variety of scenarios observed in the deep mantle (*Silver et al., 1988*). Moderate density increase evoked chemically could provide qualitativly deep slab structures as they are detected by seismic techniques as mentioned above. However, from numerical simulations it is known that other effects than chemical stratification can cause the observed features at subduction zones. One of these influences causing slab distortion could be a viscous stratification. Geoid modelling showed that an increase in viscosity across the transition zone by a factor of 10 to 100 is required to evoke observed signals (*Hager et al., 1985; Hager and Richards, 1989; Hager and Clayton, 1989; Davies and Richards, 1992*).

A viscosity jump at the upper-lower mantle interface is able to deflect subducting slabs strongly, forcing the slab to fold in the uppermost part of the lower mantle (*Gurnis and Hager, 1988*). Thickened and flattened slab structure as presented by tomographic images can be produced by a viscous layering. Although it has to be mentioned that moderate increase in viscosity alone does not hinder downwelling slabs from penetration. However, a combination of a chemically induced density contrast and a viscosity increase can provide a geoid signal consistent with observed values.

2.5.3   Stratification of the slab

Compositional heterogeneity within lithospheric slabs also has an important effect on the subduction process. An oceanic lithospheric slab might comprise an upper layer of basalt (MORB - Mid Ocean Ridge Basalt - composition) with a thickness of about 7 km underlain by a 10-20 km thick layer of depleted harzburgite and a 40 km thick layer of mildly depleted peridotite (*Irifune and Ringwood, 1993; Ringwood, 1990; 1994*). When basaltic crust is subducted into the mantle it transforms directly to eclogite (*Ringwood, 1982*). The transformed eclogite layer has an excess density of about 5 %, the layer of depleted harzburgite underneath has a density deficit of 2 % (*Irifune and Ringwood, 1993*). Dispersion analysis suuports that at depth greater than about 80 km within the subducted lithosphere a high velocity lid of 6-15 km width exists (*Gubbins and Snieder, 1991*). Since the observed high-velocity layer has similar thickness to oceanic crust it is plausible that it can be explained by eclogite which has been transformed from gabbroic crust (*Gubbins and Snieder, 1991*). Recent seismic studies could confirm the conclusion by *Gubbins and Snieder (1991)* that a thin high-velocity layer is required to explain the seismic signals observed at New Zealand stations (*Van der Hilst and Snieder, 1996*). At higher pressures the eclogite assemblage progressively transforms to a garnetite assamblage. Garnetite is denser than the surrounding mantle material in the upper mantle. However, laboratory experiments suggest that subducted oceanic crust could remain substantially buoyant relative to the surrounding pyrolite between a

depth of about 600 to 800 km in the mantle (*Irifune and Ringwood, 1993*). The underlying harzburgite would be about 0.05 g/cm³ less dense than pyrolite in the depth interval of 700 to 800 km. These buoyancy relationships could contribute to a barrier which may prevent slabs from entering the lower mantle (*Irifune and Ringwood, 1993*).

Both the effect of a light harzburgite layer and of a dense eclogite/garnetite layer with a density inversion at the transition zone have been studied. Numerical experiments have demonstrated that separation of light slab components (harzburgite) at the transition zone is unlikely in both an isoviscous mantle (*Christensen, 1989; Richards and Davies, 1989*) and in a mantle of increasing viscosity (*Gaherty and Hager, 1994*). Slabs are thickened and flattened when penetrating the lower mantle as it has a viscosity 30 to 100 times that of the upper mantle. However, compositionally different material is not disrupted. Compositional buoyancy cannot overcome the negative thermal buoyancy effects (*Gaherty and Hager, 1994*). Recently, studies about the recycling mechanism of crustal slab components at the transition zone were performed by *Van Keken et al. (1996)*. It was found that density inversion at 670 km depth alone is not sufficient to prevent crustal recycling, but that a thin layer of warm, and therefore less viscous, peridotitic slab material can decouple the crust from the the cold inner core of the slab. Crustal material can be separated from the sinking slab and may be trapped at the bottom of the transition zone.

2.6   Summary and concluding remarks

Seismological observations have demonstrated that there is a great variety in subduction zone geometries. Subducted slabs with dip angles varying from very small (e.g. Peru; *Hasegawa and Sacks, 1981*) to nearly 90° (e.g. Mariana; *van der Hilst et al., 1991*), have been observed. Slabs can either stagnate at the bottom of the upper mantle (e.g. Izu-Bonin; *van der Hilst et al., 1991*) or can penetrate into the lower mantle (e.g. Sunda arc; *Widiyantoro and van der Hilst, 1996*) As descending slabs are part of the mantle convection system an intermediate style of mantle convection (both spatially and temporaly) rather than a strictly layered or whole mantle convection type is more likely.

The major factors which control the descent of slabs are the two phase boundaries at about 400 and 670 km depth, the plate velocities, and the nature of the slab itself. The 670 km discontinuity provides resistance to the subducting slab. It is an endothermic phase transition, probably a chemical boundary providing a few percent of density increase, and a viscosity interface with ratio of lower to upper mantle viscosity somewhere between 10 to 100. The influence of the 400 km discontinuity on the descending slab is controversial. On the one hand, the elevated phase boundary may provide enhanced buoyancy forces to the descending slab.

On the other hand, phase transition could be depressed in the coldest inner parts of the slab where metastable olivine could be formed. Thus, a downward deflection of the phase transition could evoke negative buoyancy forces counteracting the outer, warmer parts of the slab where phase transition has taken place. It could be possible that both buoyancy effects are compensated. Plate motion at convergent plate boundaries, particularly the retrograde motion of the trench, seem to have important influence on the evolution of subduction zones. Convergence velocities are up to about 10 cm/yr and trench migration rates up to ca. 4 cm/yr. When relative velocities are taken into account, an eastward upper mantle flow in the order of 1 cm/yr, as proposed by *Ricard et al. (1991)*, might be an important factor. Lithospheric slabs are compositionally stratified and more viscous than the underlying mantle material. Numerical experiments showed that compositional buoyancy effects of a harzburgitic layer with density deficit cannot overcome the negative thermal buoyancy effects (*Gaherty and Hager, 1994*). Only a thin layer of warm and therefore less viscous peridotitic layer may affect that oceanic crustal material might be delaminated and trapped in the transition zone (*van Keken et al., 1996*). The overall stiffness of the slab, however, is likely to influence the slab behaviour. Beyond the physical slab (and mantle) properties time-dependence is an important feature of the subduction process.

Given the important characteristics and results as summarized above a nummerical approach provides great advantages in understanding the subduction zone dynamics. As we want to investigate the long-term evolution of subduction zones we put the following constraints on our model: the 670 km discontinuity is a - not inpenetrable - hindrance to subducting slabs and can therefore be modelled with an increase in viscosity; plate motions are incorporated as pertinent boundary conditions; and, the possibility to include a background mantle flow is given. Since it might be possible that buoyancy effects due to phase transition at 400 km are compensated within the subducting slab the 400 km discontinuity has not been implemented. Stiffness of the plates is modelled with a temperature-dependent viscosity. The effect of the stiffness of the slabs on their descent can be analysed by varying the intensity of the temperature dependence. Since buoyancy effects induced by compositional stratification are assumed to be of minor importance when compared to thermal buoyancy effects, compositional layering is neglected.

In addition, the numerical model should meet the following requirements: 1. As we are interested in the slab behaviour near the transition zone, for a higher (grid) resolution the model domain should not span the whole mantle depth. Therefore the bottom of the model box must be 'open' in order to avoid influences from the bottom on the dynamics of the descending slab. 2. Dip angles should develop in a self-consistent way and not restricted by, for example, grid refinement in a certain region. Downwellings at the sidewall and thereby forcing the downdip angle to be 90 °, should be avoided. 3. Plates should be asymmetric, i.e. only one

plate should subduct.

As a completion to seismic images time-dependent characteristics of the subduction process can be analysed. Where subduction has ceased ('fossil' subduction zones), the upper mantle structure at convergent plate boundaries can also be investigated. Moreover, a great advantage of numerical modelling over laboratory experiments is that modelling can provide quantitative estimates of temperature anomalies evoked by the downgoing slab. This is particularly important for the expression of the subduction process in terms of the seismic velocity structure as the model temperature anomalies can then be converted to seismic velocity anomalies (e.g. *de Jonge et al., 1994; Vacher et al., 1996*), which in turn can be compared in magnitude and shape with tomography results.

CHAPTER 3

The numerical model

A numerical procedure has been employed in order to investigate the upper mantle structure at subduction zones. In this chapter we first consider the basic equations describing the convetion system in a fluid resembling the Earth's mantle material. Second, we describe the numerical methods applied to solve the basic equations.

Throughout this study a two-dimensional cartesian model domain will be used.

3.1 Basic equations

As a model system we consider a viscous fluid neglecting all effects of density changes except their buoyancy effects (Boussinesq approximation) and neglecting inertia effects due to high viscosity of the Earth's mantle (infinite Prandtl number). Under these assumptions the convection system is governed by the equations describing conservation of mass, momentum and energy:

$$\nabla \cdot \vec{v} = 0 \tag{3.1}$$

$$\nabla p - \rho \vec{g} - \nabla \cdot \underline{\underline{\sigma}} = 0 \tag{3.2}$$

$$\frac{\partial T}{\partial t} + (\vec{v} \cdot \nabla)T - \kappa \nabla^2 T = 0 \tag{3.3}$$

No internal heating is implemented throughout the experiments. Symbols are explained in Table 1. Since in our models thermal buoyancy forms the only driving force for convection, the equation of state can be approximated in a first order by:

$$\rho(T) = \rho_0(1 - \alpha(T - T_0)) \tag{3.4}$$

Inserting (3.4) into the equation of motion (3.2) and considering that the pressure is composed by a hydrodynamic and a hydrostatic pressure:

$$p = P + \rho_0 g z \tag{3.5}$$

the equation of motion can be modified to:

$$\rho_0 \alpha (T - T_0)\vec{g} - \nabla P + \nabla \cdot \underline{\underline{\sigma}} = 0 \tag{3.6}$$

Table 3.1 *Summary of parameters used. The non-dimensional quantities (primed) are revealed by a factorization scheme after Turcotte et al. (1973).*

Parameter	Name	Unit	Non-dimensional quantities
x	x-component of direction	m	$x' = x \cdot 1/d$
z	z-component of direction	m	$z' = z \cdot 1/d$
∇	$\nabla = (\partial/\partial x, \partial/\partial z)$	m^{-1}	$\nabla' = \nabla \cdot d$
$\vec{v}$	velocity vector, $\vec{v} = (u,w)^{-1}$	ms^{-1}	$\vec{v}' = \vec{v} \cdot d/\kappa_o$
t	time	s	$t' = t \cdot \kappa_o/d^2$
ρ	density	kg m^{-3}	$\rho' = \rho/\rho_o$
$\vec{g}$	accel. vector of gravity	m s^{-2}	
η	dynamic viscosity	Pa s	$\eta' = \eta/\eta_o$
κ	thermal diffusivity	m^2 s^{-1}	$\kappa' = \kappa/\kappa_o$
P	hydrodynamic pressure	Pa	$P' = P \cdot d^2/\kappa_o\eta_o$
$\underline{\underline{\sigma}}$	deviatoric stress tensor	Pa	$\underline{\underline{\sigma}}' = \underline{\underline{\sigma}} \cdot d^2/\kappa_o\eta_o$
α	thermal expansion coefficient	K^{-1}	$\alpha' = \alpha/\alpha_0$
T	temperature	K, °C	$T' = (T - T_o)/\Delta T$

$\vec{z}$ counts in direction opposing to gravity. According to *Turcotte et al. (1973)* we transform the equations (3.6),(3.3) via the scaling scheme given in table 1 to the dimensionless equations:

$$Ra T' \vec{e}_z - \nabla' P' + \nabla' \cdot \underline{\underline{\sigma}}' = 0 \qquad (3.7)$$

$$\frac{\partial T'}{\partial t'} + (\vec{v}' \cdot \nabla')T' = \nabla'^2 T' \qquad (3.8)$$

Ra is the dimensionless Rayleigh number given by

$$Ra = \frac{g\rho_o\alpha\Delta T d^3}{\eta_o\kappa_o}$$

In the following non-dimensional quantities will be used. Primes will be omitted. Introducing the scalar stream function ψ defined by

$$\vec{v} = (u,w) = \left(\frac{\partial\psi}{\partial z}, -\frac{\partial\psi}{\partial x}\right) \qquad (3.9)$$

and with

$$\sigma_{ij} = \eta\left(\frac{\partial v_i}{\partial x_j} + \frac{\partial v_j}{\partial x_i}\right) \qquad (3.10)$$

the equation of motion can be modified to the final scalar version of the equation which has to be solved:

$$\left(\frac{\partial^2}{\partial x^2} - \frac{\partial^2}{\partial z^2}\right)\eta(T,z)\left(\frac{\partial^2}{\partial x^2} - \frac{\partial^2}{\partial z^2}\right)\psi + 4\frac{\partial^2}{\partial x\partial z}\left(\eta(T,z)\frac{\partial^2}{\partial x\partial z}\psi\right) = Ra_o\frac{\partial T}{\partial x} \qquad (3.11)$$

With (3.9) one obtains for the heat transport equation:

$$\frac{\partial T}{\partial t} = -\frac{\partial \Psi}{\partial z}\frac{\partial T}{\partial x} + \frac{\partial \Psi}{\partial x}\frac{\partial T}{\partial z} + \nabla^2 T \qquad (3.12)$$

The continuity equation (3.1) is implicitly accomplished by (3.9). The numerical solution of the equations (3.11) and (3.12) will be described in the next paragraph.

3.2 Numerical method

The coupled system of non-linear partial differential equations (3.11) and (3.12) is solved numerically by a finite element method. The underlying idea of this method is to devide the model domain into finite elements, to formulate basis functions (shape functions), and to find a best approximated solution within the space spanned by these shape functions. Different types of elements are used for each of the equations. Whereas for the equation of motion a variational principle (*Zienkiewicz, 1977*) can be constructed, it is not possible to apply this method to the energy equation. To approximate the solution of the heat transport equation the method of Galerkin is applied. Next, the two different schemes to solve both of the equations (3.11), (3.12) are described.

3.2.1 Solution of the equation of motion

Variational principle

Considering the equation of motion (3.11) it can be written in the form:

$$\underline{\underline{L}}\vec{u} + \vec{b} = 0 \qquad (3.13)$$

with

$$\underline{\underline{L}} \equiv \left(\frac{\partial^2}{\partial x^2} - \frac{\partial^2}{\partial z^2}\right)\eta\left(\frac{\partial^2}{\partial x^2} - \frac{\partial^2}{\partial z^2}\right) + 4\frac{\partial^2}{\partial x \partial z}\eta\frac{\partial^2}{\partial x \partial z}$$

$$\vec{u} \equiv \Psi$$

$$\vec{b} \equiv -Ra\frac{\partial T}{\partial x}$$

Since $\underline{\underline{L}}$ is a symmetric and positive definit differential operator it can be shown that a variational principle exists. That means that a solution $\vec{u}$ for system (3.13) is equal to the solution which makes the functional

$$\Pi(\vec{u}) = \int_{\Omega}\left[\frac{1}{2}\vec{u}^T L \vec{u} + \vec{u}^T \vec{b}\right] d\Omega + boundary\ terms \qquad (3.14)$$

stationary with respect to small changes $\delta\vec{u}$ (*Zienkiewicz, 1977*). Ω is the domain on which the system of partial differential equations has to be solved. In order to minimize the functional Π its variation has to be zero:

$$\delta\Pi(\vec{u}) = 0 \qquad (3.15)$$

For $\vec{u} =$ constant (Dirichlet boundary condition), $\frac{\partial \vec{u}}{\partial \vec{n}} = 0$ (Neumann boundary condition), or $\nabla^2 \vec{u} = 0$ (free slip) the boundary terms in (3.14) vanish. By identity (3.13) equation (3.14) can be written as:

$$\Pi(\Psi) = \int_{\Omega} \left[\frac{1}{2} \Psi \left(\frac{\partial^2}{\partial x^2} - \frac{\partial^2}{\partial z^2} \right) \eta \left(\frac{\partial^2}{\partial x^2} - \frac{\partial^2}{\partial z^2} \right) \Psi + 4 \Psi \frac{\partial^2}{\partial x \partial z} \eta \frac{\partial^2}{\partial x \partial z} \Psi - \Psi Ra \frac{\partial T}{\partial x} \right] d\Omega$$
(3.16)

Green's theorem can be employed to reduce the integrand to second order derivatives. Green's theorem is given by

$$\int_{\Omega} \Phi \frac{\partial \Theta}{\partial x} \, dx \, dz = -\int_{\Omega} \frac{\partial \Phi}{\partial x} \Theta \, dx \, dz + \oint_{\Gamma} \Phi \Theta n_x \, d\Gamma$$
(3.17)

Φ and Θ are two function sets, n_x is the direction cosine between the normal and the x-direction, and $\int_{\Gamma}$ is the boundary integral. Applying Green's theorem (3.17) two times to (3.16) we obtain:

$$\Pi(\Psi) = \frac{1}{2} \int_{\Omega} \left[\left(\frac{\partial^2 \Psi}{\partial x^2} - \frac{\partial^2 \Psi}{\partial z^2} \right) \eta \left(\frac{\partial^2 \Psi}{\partial x^2} - \frac{\partial^2 \Psi}{\partial z^2} \right) + 4 \frac{\partial^2 \Psi}{\partial x \partial z} \eta \frac{\partial^2 \Psi}{\partial x \partial z} - \Psi Ra \frac{\partial T}{\partial x} \right] d\Omega$$
(3.18)

Again, the boundary terms, which arise by the application of Green's theorem, vanish.

Stiffness matrix and load vector

With the finite element process a solution will be sought in the approximate form:

$$\Psi \simeq \hat{\Psi}(\vec{a}) = \sum_{i=1}^{n} \vec{N_i} \vec{a_i}$$
(3.19)

where $\vec{N_i}$ are shape functions prescribed in terms of the independent coordinates x and z, $\vec{a}$ is the vector of unknowns $(\vec{a_1}, \vec{a_2}, ..., \vec{a_n})^T$, and n is the number of element nodes. Substituting (3.19) in (3.18) results in:

$$\Pi(\hat{\Psi}) \equiv \Pi(\vec{a}) = \frac{1}{2} \int_{\Omega} \left[\left(\sum \frac{\partial^2 \vec{N_i}}{\partial x^2} \vec{a_i} - \sum \frac{\partial^2 \vec{N_i}}{\partial z^2} \vec{a_i} \right) \eta \left(\sum \frac{\partial^2 \vec{N_i}}{\partial x^2} \vec{a_i} - \sum \frac{\partial^2 \vec{N_i}}{\partial z^2} \vec{a_i} \right) \right.$$
$$\left. + 4 \sum \frac{\partial^2 \vec{N_i}}{\partial x \partial z} \vec{a_i} \quad \eta \sum \frac{\partial^2 \vec{N_i}}{\partial x \partial z} \vec{a_i} - \left(\sum \vec{N_i} \vec{a_i} \right) Ra \frac{\partial T}{\partial x} \right] d\Omega$$
(3.20)

Applying the variational principle $\delta \Pi = 0$ (3.15) we get for every $\vec{a_i}$:

$$\frac{\partial \Pi}{\partial \vec{a_i}} = 0$$
(3.21)

This leads to the linear set of equations:

$$\underline{S}\vec{a} = \vec{f} \qquad (3.22)$$

with

$$S_{ij} = \int_{\Omega} \left[\left(\frac{\partial^2 N_i}{\partial x^2} - \frac{\partial^2 N_i}{\partial z^2} \right) \eta \left(\frac{\partial^2 N_j}{\partial x^2} - \frac{\partial^2 N_j}{\partial z^2} \right) + 4 \frac{\partial^2 N_i}{\partial x \partial z} \eta \frac{\partial^2 N_j}{\partial x \partial z} \right] d\Omega$$

$$f_j = \int_{\Omega} N_j Ra \frac{\partial T}{\partial x} d\Omega$$

Where $\underline{S}$ and $\vec{f}$ are the stiffness matrix and the load vector, respectively.

Non-conforming elements

Mathematically correct would be the use of conforming elements, which means that, when the stiffness matrix contains derivatives of m-th order, the shape functions must be C^{m-1} continuous. In our case (see 3.22) $\frac{\partial \Psi}{\partial x}$ and $\frac{\partial \Psi}{\partial z}$ should be then continuous across the element boundaries. Convergence cannot be proven rigorously for non-conforming elements, which do not fulfil the conditions of continuity. However, non-conforming elements have been applied succesfully in finite element problems (*Zienkiewicz, 1977; Schwarz, 1980*). Our model domain is divided into rectangular, non-conforming elements with four nodal points in the vertices of the element. The stream function is only C^1-continuous in the nodal points, but not on the element boundaries. In each nodal point i the vector $\vec{a}_i$ of unknowns is defined as:

$$\vec{a}_i = \left(\hat{\Psi}_i, \frac{\partial \hat{\Psi}_i}{\partial z}, \frac{\partial \hat{\Psi}_i}{\partial x} \right)^T$$

In each element the system of linear equations has to be solved for 12 unknowns - three unknowns at each of the four vertices. Thus the stream function can be expanded by an uncomplete fourth order polynomial in x and z:

$$\hat{\Psi} = \alpha_1 + \alpha_2 x + \alpha_3 z + \alpha_4 x^2 + \alpha_5 xz + \alpha_6 z^2 + \alpha_7 x^3 + \alpha_8 x^2 z + \alpha_9 xz^2 + \alpha_{10} z^3$$
$$+ \alpha_{11} x^3 z + \alpha_{12} xz^3 \qquad (3.23)$$

The system of equations is first solved for every element, then the global matrix and vector is assembled. Therefore every element is transformed into a unit square with local variables ξ and ζ. For every element we have:

$$\hat{\Psi} = \sum_{k=1}^{4} \vec{N}_k \vec{a}_k \qquad (3.24)$$

where k is the number of nodal points of each element, and

$$\vec{N}_k = (N_k, \frac{\partial N_k}{\partial \zeta}, \frac{\partial N_k}{\partial \xi})^T \qquad \vec{a}_k = (\hat{\Psi}_k, \frac{\hat{\Psi}_k}{\partial \zeta}, -\frac{\hat{\Psi}_k}{\partial \xi})^T \qquad (3.25)$$

From (3.23) it follows for the local elements:

$$\hat{\Psi}_k = f(\alpha_i, \xi, \zeta, \xi^2, \zeta^2 ...)$$

$$\frac{\hat{\Psi}_k}{\partial \zeta} = f(\alpha_i, \xi, \zeta, \xi^2, \zeta^2 ...) \qquad (3.26)$$

$$\frac{\hat{\Psi}_k}{\partial \xi} = f(\alpha_i, \xi, \zeta, \xi^2, \zeta^2 ...)$$

With (3.24) and (3.26) four local shape functions - for each element - dependent on ξ and ζ can be constructed.

3.2.2   Solution of the equation of energy

The heat advection-diffusion equation (3.12) is of the form:

$$\underline{\underline{L}}\vec{u} - \vec{f} = 0 \qquad (3.27)$$

where

$$\underline{\underline{L}} \equiv \frac{\partial}{\partial t} + \frac{\partial \Psi}{\partial z}\frac{\partial}{\partial x} - \frac{\partial \Psi}{\partial x}\frac{\partial}{\partial z} - \frac{\partial^2}{\partial x^2} + \frac{\partial^2}{\partial z^2}$$
$$\vec{u} \equiv T$$
$$\vec{f} \equiv 0$$

Since the partial differential operator is not symmetric no variational principle can be constructed to solve the heat transport equation (*Zienkiewicz, 1977*). Here a method of weighted residuals has to be applied (method of Galerkin). By inserting an approximate solution $\hat{T}$ into the differential equations (3.27) a residual R is obtained:

$$R = \underline{\underline{L}}\vec{\hat{T}} - \vec{f} \qquad (3.28)$$

The residual has to be minimized with respect to a set of weighting functions. The temperature is approximated by

$$\vec{\hat{T}} = \sum_{i=1}^{n} \vec{T}_i(t)\vec{N}_i(x,z) \qquad (3.29)$$

where $\vec{T}_i(t)$ and $\vec{N}_i$ are the vector of nodal values T_i of the temperature, and the nodal values of bilinear shape functions, respectively. With (3.29) application of the method of Galerkin to (3.27) leads to the system of differential equations:

$$\underline{\underline{B}}\vec{\dot{T}} + \underline{\underline{A}}\vec{T} + \vec{f} = 0 \qquad (3.30)$$

where

$$B_{ij} = \int_B W_j N_i \, dx \, dz$$

$$A_{ij} = \int_B \left[\left(\frac{\partial W_j}{\partial x} \frac{\partial N_i}{\partial x} + \frac{\partial W_j}{\partial z} \frac{\partial N_i}{\partial z} \right) + W_j \left(\frac{\partial \psi}{\partial z} \frac{\partial N_i}{\partial x} - \frac{\partial \psi}{\partial x} \frac{\partial N_i}{\partial z} \right) \right] dx \, dz$$

$$f_j = \int_{\Gamma B} W_j \frac{\partial T}{\partial \vec{n}} d\Gamma B = 0$$

$\vec{T}$ denotes the vector of the temperature at the element nodes, $\dot{\vec{T}}$ denotes the derivative of the temperature with respect to time, W_j are the weighting functions, B is the domain of integration, and ΓB its boundary. In the standard Bubnov-Galerkin method the weighting functions are chosen to equal the shapefunctions N_i. In order to avoid physically meaningless oscillations which can be induced by using this solution scheme the weighting functions are upwind corrected (*Heinrich et al., 1977; Hansen and Ebel, 1988*).

3.2.3   Time integration

In the energy equation (3.12) a time derivative appears. To discretize the time-dependence a second order predictor-corrector method is used. First, a predictor T'^{m+1} is determined by a fully implicit step from T^n and Ψ^n. Second, it follows a Cranck-Nicholson corrector step to obtain T^{n+1} which is used to calculate the final Ψ^{n+1} (*Hansen and Ebel, 1988*).

For accuracy reasons the timestep has been limited to half the step size Δt allowed by the Courant-Friedrich-Levy criterion (*Hansen and Ebel, 1988; Hansen et al., 1993*).

3.3 Conversion from model temperature to seismic velocity anomaly

Our model solves for the stream function (and its derivatives) and for the temperature. The latter can be compared indirectly with the seismic velocity structure, since the seismic velocity is mainly derived from the temperature structure. However, additionally to the temperature, elastic constants (as the bulk modulus and rigidity) and their depth- and temperature-dependent properties determine the seismic velocity, as well. Conversion from the model temperature to seismic velocity structure under the consideration of the elastic constants, can then be directly compared with observed seismic images. As the temperature- and depth-dependence of the elastic constants is strongly non-linear and not completely known such a transformation includes uncertainties. However, an extended study about conversion from temperature to seismic velocities under the assumption of complex mineralogy results has been done by *Vacher et al. (1996)* and to a lesser extend by *de Jonge et al. (1994)*. We are interested in geodynamical constraints on the subduction process, and intend to test our models whether their transformation to seismic velocity is consistent with observed values. Thus, in the present study the less extended method of *de Jonge et al. (1994)* is used, which will be described in the following for completeness.

We consider the P velocity v_p to be depth- and temperature- dependent due to the dependence of the elastic parameters of olivine on pressure and temperature:

$$v_p = \left[(K + \frac{4}{3}\mu)/\rho \right]^{\frac{1}{2}} \tag{3.31}$$

K is the bulkmodulus, μ the rigidity and ρ is the density following the linear equation of state as given in (3.4). From (3.31) we obtain:

$$\frac{\partial v_p}{\partial T} = \frac{1}{2v_p\rho} \left[\frac{\partial K}{\partial T} + \frac{4}{3}\frac{\partial \mu}{\partial T} + \alpha \left(K + \frac{4}{3}\mu \right) \right] \tag{3.32}$$

The sensitivity of v_p to temperature is dependent on the elastic parameters. Figure 3.1 shows the depth-dependence of $\frac{\partial v_p}{\partial T}$ as revealed by *de Jonge et al. (1994)* from laboratory data. The values of the graph are avarage values of results obtained by a Monte-Carlo evaluation of laboratory data from *Graham and Barsch (1969)*, *Mizutani et al. (1970)*, *Chung (1971)*, *Anderson et al. (1972)*, *Wang and Simmons (1972)*, *Suzuki (1975)*, *Sumino et al. (1977, 1983)*, *Dziewonsky and Anderson (1981)*, *Suzuki et al. (1981, 1983)*, *Turcotte and Schubert (1982)*, *Sawamoto et al. (1984)*, *Weidner et al. (1984)*, *Bina and Wood (1987)*, *Isaak et al. (1989)*, and *Gwanmesia et al. (1990)*. The seismic velocity anomaly is then obtained by:

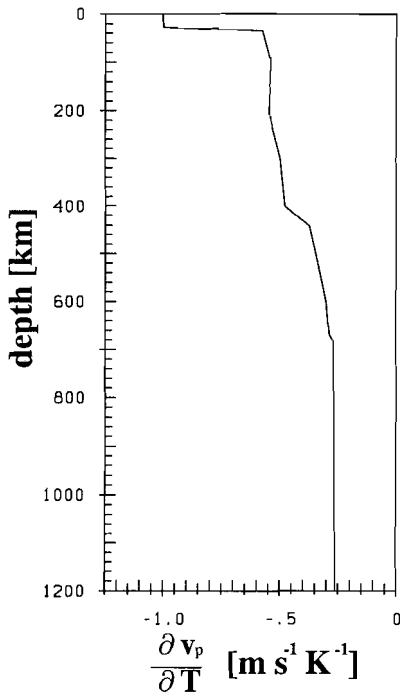$$\Delta v_p = (T - T_{ref}(z)) \frac{\partial v_p}{\partial T}\bigg|_z \tag{3.33}$$

Figure 3.1 *The depth-dependence of $\frac{\partial v_p}{\partial T}$. After de Jonge et al. (1994). For a discussion of error margins in the measurements of elastic properties see de Jonge (1995).*
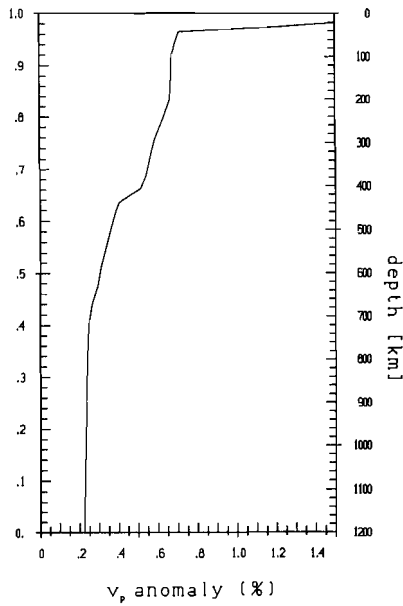

Figure 3.2 *Percentual P-wave velocity anomaly as a function of depth. The seismic velocity anomaly arises from a temperature anomaly of -100°C throughout the depth. As reference P velocity the IASP91 model from Kennet and Engdahl (1991) as shown in Figure 3.3 has been taken.*

where $T_{ref}(z)$ is the temperature of the unperturbed mantle. Since only the temperature difference between the ambient mantle and the anomaly determines the velocity anomaly, the reference temperature is not very critical (*de Jonge, 1995*). In order to demonstrate the effect of the depth-dependence of $\frac{\partial v_p}{\partial T}$ the same test has been done as shown by *de Jonge et al. (1994)*: Figure 3.2 indicates the percentual P velocity anomaly provided by a temperature anomaly of -100 °C throughout the depth of 1200 km. As reference P velocity (of the unperturbed ambient mantle) the global IASP91 model (*Kennet and Engdahl, 1991*) as shown in Figure 3.3 has been taken. The profile of Figure 3.2 shows a clear depth dependence of the seismic velocity anomaly. Although the temperature anomaly is the same throughout the depth the v_p anomaly decreases with depth.
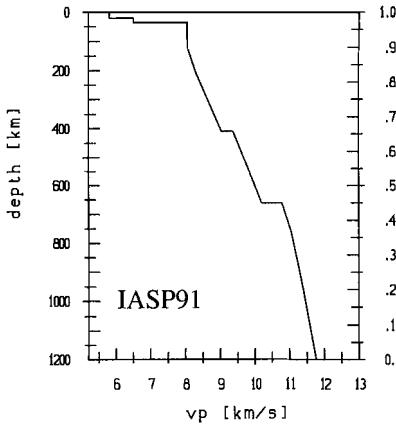
Figure 3.3 *P-wave velocity of the global IASP91 model (Kennet and Engdahl, 1991).*

CHAPTER 4

Controls of slab structure by viscosity

4.1   Introduction

The viscosity profile of the Earth is still a very debatable subject (*Ricard and Wuming, 1991; Kerr, 1996*). Viscosity at the Earth's surface might be three to four orders higher than the upper mantle viscosity (*Bills et al., 1994*). Post-glacial rebound data of Pleistocene Lake Bonneville shorelines in the Basin and Range Province indicate that the upper mantle viscosity is about 10^{19} to 1.2×10^{20} Pa s (*Bills and May, 1987; Bills et al., 1994*)). Response of meltwater loading of Pacific islands yield an estimate of somewhat lower values (*Lambeck, 1990*). Analysis of sea-level changes indicate an effective upper mantle viscosity of $1 - 5 \times 10^{20}$ Pa s and a lower mantle viscosity of about two orders of magnitude greater (*Nakada and Lambeck, 1987, 1989; Lambeck et al., 1990*). *Ricard and Wuming (1991)* inferred the viscosity structure from geoid, topography and plate velocities. In their computed radial viscosity profile no sharp discontinuity is requested at the upper-lower mantle interface. However, from mineral physics it is accepted that increasing pressure transforms the crystal structure of the mantle rock at the 670 km boundary which could explain an abrupt increase in viscosity at that depth (e.g. *Akaogi et al., 1989*). Numerical model results indicate that the viscosity increases from upper to lower mantle at least by a factor of 10 to 30 (*Gurnis and Hager, 1988*). This result is established by geoid modelling which implies that even a factor of 10 to 300 increase in viscosity may occur near the 670 km discontinuity (*Hager and Richards, 1989*). These results are only a few of a broad field of research. *Shen and Forsyth (1992)* and *Davies and Richards (1992)* are mentioned here for further references. Figure 4.1 (after *Davies and Richards (1992)*) shows a plausible viscosity profile through the mantle. The viscosity decreases across the lithosphere, increases due to pressure continuously and due to pressure-induced phase transition stepwise at 670 km depth. The dashed graph indicates the uncertainty of the low viscosity zone in the upper mantle.

Here, we want to explore the effect of the proposed discontinuity in rheological structure on the evolution of subduction zones. For that purpose we applied our two dimensional finite element model (see Chapter 3) varying the parameters which describe the viscosity. In the models discussed in this chapter the 670 km discontinuity is only represented by an increase in viscosity. No phase transition or
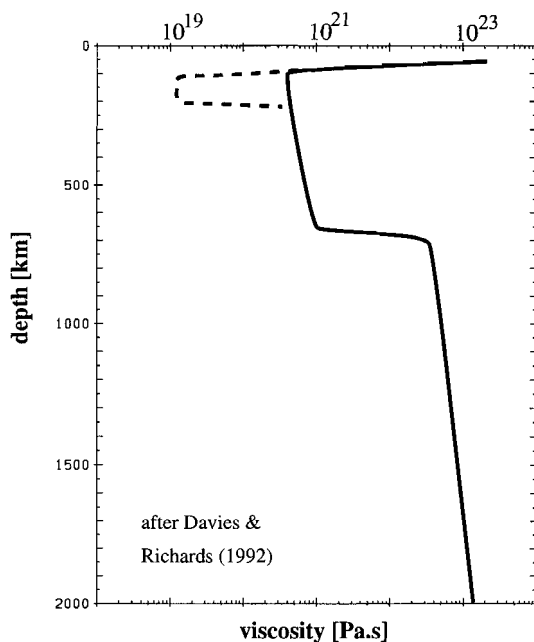
Figure 4.1 *Plausible viscosity profile through the Earth's mantle. The viscosity decreases across the lithosphere, increases due to pressure continuously and due to pressure-induced phase transition stepwise at 670 km depth. The dashed graph indicates the uncertainty of the low viscosity zone in the upper mantle. (After Davies and Richards, 1992).*

chemical boundary has been included in order to concentrate only on the effect of the viscosity interface. In earlier models including phase changes the geometry of subduction zones is limited with restriction of the downgoing slab to be vertically at the sidewalls (e.g. *Christensen and Yuen, 1984; Zhong and Gurnis, 1994*). For a better resolution subduction zone models are often not scaled deeper than to about 1500 km, thereby restricting the bottom to be closed, which might have some effect on the descent of the slab (e.g. *Christensen and Yuen, 1984; Gurnis, 1988*). The most realistic subduction zone models - but with emphasis on the effect of trench migration (see chapter 5) - have been performed by *Zhong and Gurnis (1995)* and *Christensen (1996)* with a subducting slab encountering a phase boundary. In the latter (*Christensen, 1996*) a semi-permable bottom boundary is considered. Recent laboratory experiments also provided considerable insight in the evolution of subducting slabs (*Guillou-Frottier et al., 1995; Griffiths et al., 1995*). However, the main aspect of that research was devoted to the effect of trench migration on the subduction process (see chapter 5).

4.2 The Model

For the investigation of the evolution of subduction zones we consider overriding and underthrusting plates with imposed velocities and an 'open' bottom in order to avoid influences of the bottom on the dynamics of the descending slab.
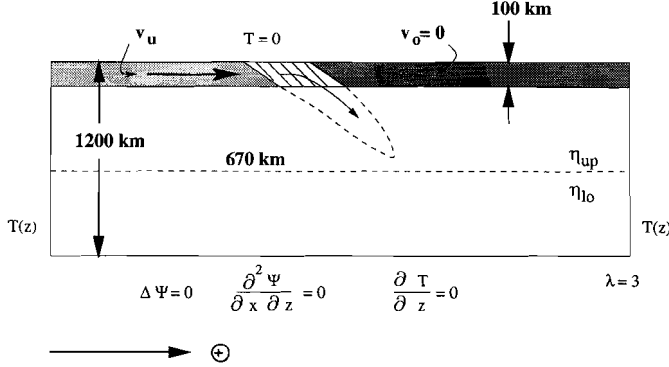
Figure 4.2 *Scheme of the model geometry. The depth is 1200 km, the width is given by the aspect ratio $\lambda = 3$. v_u and v_o are the underthrusting and overriding plate velocities, respectively. T is the temperature, ψ is the streamfunction, and η_{up} and η_{lo} are the upper and lower mantle viscosity, respectively. The arrow at the bottom marks the direction of positive horizontal velocities.*

The finite element model used is described in Chapter 3. The model domain which is illustrated in Figure 4.2 consists of a two-dimensional 3×1 box representing the uppermost 1200 km of the mantle. Solutions were obtained on 68×38 rectangular grids with aquidistant horizontal spacing and decreasing grid spacing from bottom to the top. The refinement is polynomial, i.e. every element is reduced in vertical direction by a factor α from the previous element beneath:

$$\Delta z_{i+1} = \alpha \Delta z_i$$

where Δz_i is the (vertical) thickness of the i-th element. The i-th z-coordinate is then given by:

$$z_i = \sum_{k=1}^{i} \alpha^{k-1} \Delta z_1$$

Δz_1 is the vertical element size of the bottom element which is chosen to be 0.06. Therewith the bottom element has a thickness of 72 km, the surface element is 9.9 km thick (when the model domain is scaled to 1200 km). The light and dark grey shaded area in Figure 4.2 illustrates the underthrusting and overriding plate, each of which has imposed horizontal velocity (v_u, v_o, respectively) and zero vertical velocity throughout the plates (*Lowman and Jarvis, 1995*). Plates are spanned

over 9 grid points and have a thickness of about 100 km (the exact value is 96.4 km). v_u and v_o are absolute velocities with respect to a fixed coordinate system in the deep mantle. In the present chapter a fixed position of the trench will be considered, so that v_o is taken to be zero. Since, within the hatched ca. 150 km wide area between the two plates, horizontal velocity decreases from v_u to v_o and vertical velocity is not constrained to zero, subduction is initiated. The model allows for an additional background mantle flow, which will be used in the following chapter. At the bottom free slip boundary conditions ($\nabla^2 \psi = 0$) and restriction of the horizontal velocity to the mantle flow as imposed at the sidewalls ($\frac{\partial^2 \psi}{\partial x \partial z} = 0$) are employed. These boundary conditions allow for vertical material flow through the bottom. Zero conductive heatflux ($\frac{\partial T}{\partial z} = 0$) is consistent with the absence of a thermal boundary layer at the bottom. Since vertical velocities are not implicitly zero, advective heatflux is possible.

Boundary condition for the temperature at the sidewalls and the initial temperature field are given in Figure 4.3 a and b, respectively. At the vertical boundaries temperature decreases across the upper 100 km from 0 (scaled to 0 °C) to 0.5 (scaled to 1364 °C) and stays constant to the bottom. The same boundary conditions have been used for different Rayleigh numbers. In the initial temperature field the gradient across the lithosphere is less than that of the vertical boundaries in order to yield a lower temperature (than 1364 °C) at the bottom of the lithosphere. Since the temperature is not fixed at the bottom at 1200 km depth dimensionless temperature reaches values up to 0.55 which is scaled to 1500 °C. We tested, that, when taking the profile of the initial temperature field as boundary condition, or taking the boundary condition as initial temperature field, our results and conclusions are not affected significantly.

The viscosity is parameterized as:

$$\eta(T, z) = \beta(z)\eta_o(z)exp[-b(T - 0.5) + c(1 - z)] \qquad (4.1)$$

where T is the dimensionless temperature, and z is directed contrary to gravitation. The temperature dependence supports plate like behaviour. b and c are the parameters controling the temperature- and depth dependence of the viscosity, respectively. $\beta(z)$ is a step function which is one for depths lower than 670 km, and greater or equal than one for depths greater than 670 km. Just speaking from β - in the following - means the factor by which the viscosity increases at 670 km depth. When $c = 0$ and $\beta > 1$ for z greater than 670 km a step function determines the viscosity increase with depth, whereas $c \neq 0$ and $\beta = 1$ provides a continuous viscosity increase with depth (i.e. with pressure). The reference viscosity η_0 is defined by equation 4.1 to be the viscosity in the upper mantle. We specify Rayleigh numbers on the basis of η_0. The use of Rayleigh numbers between 10^6 and 10^7, which are reasonable values for the whole mantle, is consistent with the 'open' nature of our model as being a part of a whole mantle convection system.
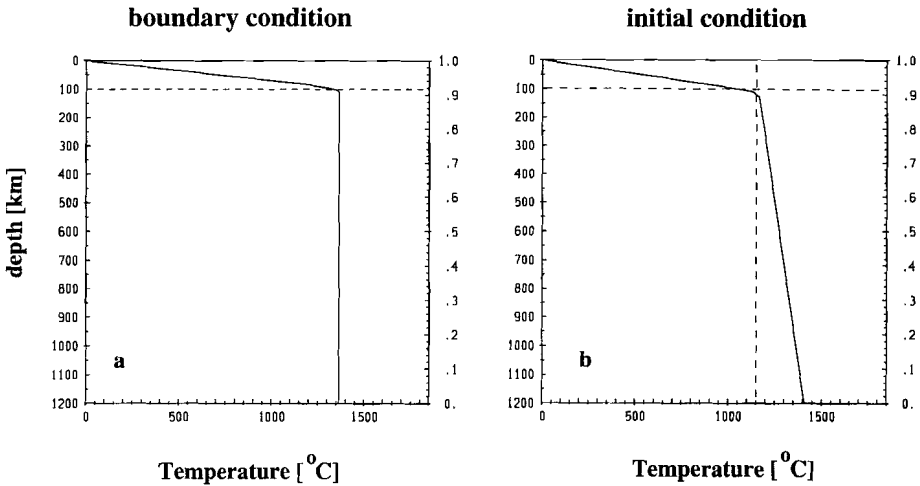
boundary condition   **initial condition**

Temperature [°C]   **Temperature [°C]**

Figure 4.3 *Boundary condition of the temperature at the sidewalls (a) and a profile of the initial temperature field (b).*

4.3   Results

Table 4.1 gives the parameters of 12 experiments discussed here. The overriding plate of each model is fixed ($v_o = 0$), and the background mantle flow has been set to zero ($v_m = 0$).

Table 4.1 *Summary of Models*

case	b	c	β	Ra	v_u (cm/yr)
4.1	0	0	1	10^6	5
4.2	0	0	10	10^6	5
4.3	0	0	100	10^6	5
4.4	7.8	0	1	10^6	5
4.5	10.6	0	50	10^6	5
4.6	10.6	0	300	10^6	5
4.7	10.6	4.6	1	10^6	5
4.8	10.6	4.6	1	10^7	5
4.9	7.8	0	1	10^6	8
4.10	10.6	0	50	10^6	8
4.11	10.6	0	50	$5 \cdot 10^6$	8
4.12	10.6	0	50	10^7	8
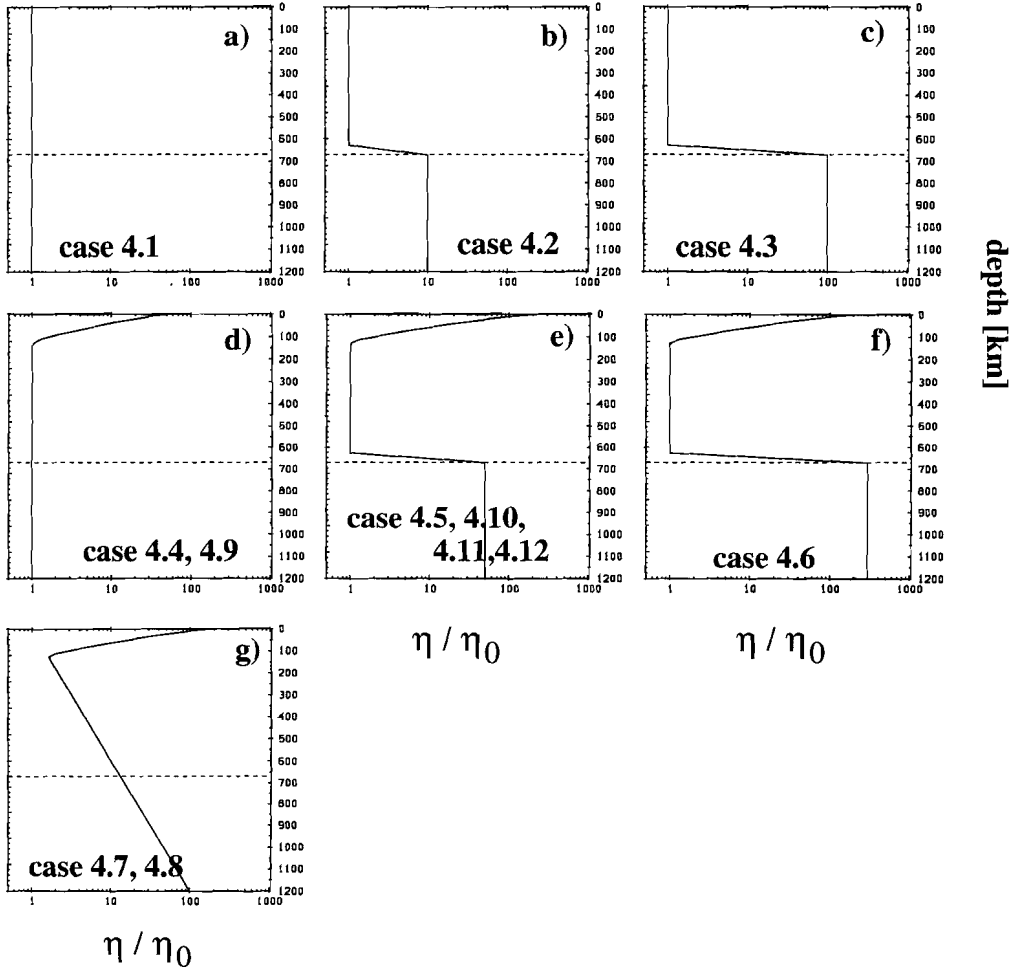
Figure 4.4 *Viscosity profiles for cases 4.1-4.12 for the temperature profile (boundary condition) as given by Figure 4.3.*

Isoviscous slabs - viscosity jump varies - (Case 4.1, 4.2, 4.3: b=0, c=0)
In the first three cases 4.1, 4.2, and 4.3 the factor β (see equation 4.1) by which the viscosity increases at 670 km depth has been varied, namely β is 1, 10, and 100, respectively. None of these three models have temperature-dependent viscosity. Thus in case 4.1 viscosity is constant over the whole model domain. The viscosity profiles of case 4.1-4.3 are shown in Figure 4.4 a,b,c, respectively. Figure 4.5 shows 5 timesteps of the temperature field of case 4.1.
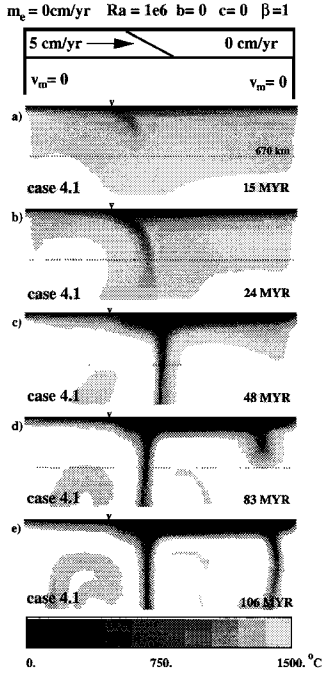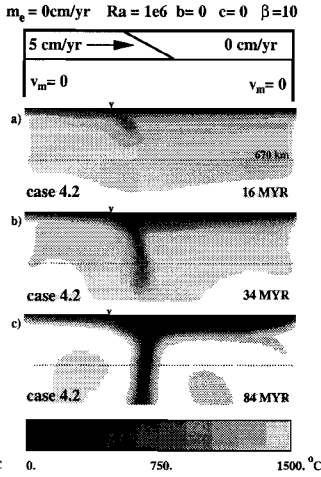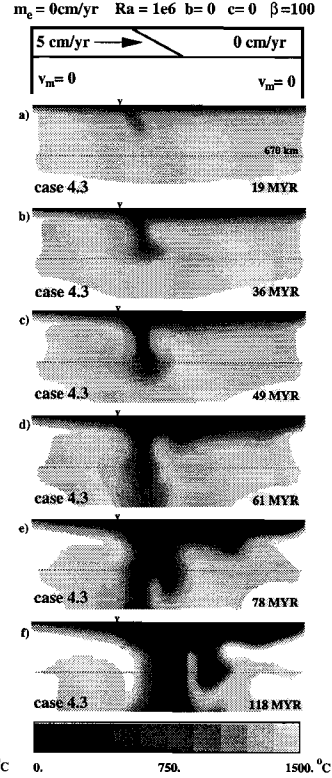
Figure 4.5   **Figure 4.6**   **Figure 4.7**

left: Evolution of the temperature field and sketch of plate velocities of case 4.1. Viscosity is constant. For viscosity profile see Figure 4.4a. The model geometry is given in Figure 4.2.

middle: Temperature field and sketch of plate velocities of case 4.2. The viscosity is constant due to temperature but increases at 670 km depth by a factor of 10. For viscosity profile see Figure 4.4b.

right: Evolution of the temperature field and plate velocities of case 4.3. Viscosity is not temperature-dependent, but increases at 670 km by a factor of 100. For viscosity profile see Figure 4.4c.

Ca. 24 Myr after subduction has started the tip of the subducting slab reaches the bottom at 1200 km depth (Figure 4.5a). The slab sinks straight into the lower mantle and the evoked temperature anomaly reaches a quasi-stationary state (Figure 4.5 c-e). Next to this first downstream, a second instability originated in the thermal boundary layer beneath the rigid plate develops sinking nearly

vertically (Figure 4.5 d-e). An increase in viscosity at the 670 km discontinuity
by a factor of 10 - as has been done in case 4.2 - does not change the angle of
penetration of the descending slab (Figure 4.6). Descent of the slab is slower than
in the first case 4.1: The tip of the slab reaches the bottom ca 10 Myr later than
in case 4.1 (Figure 4.6 b). The shape of the temperature anomaly is also changed,
it is slightly broadened. Increasing the ratio of lower to upper mantle viscosity to
a factor of 100 affects the shape and descent velocity of the subducting slab: The
slab structure becomes broader and descent velocity is reduced (case 4.3, Figure
4.7). The leading edge of the downwelling is flattened and extended horizontally
on top of the discontinuity (Figure 4.7 b). However, the slab is still able to
penetrate through the viscosity interface (Figure 4.7 c). The main descending slab
is accompanied by several other thermal boundary layer instabilities beneath the
rigid plate. The junction of of the smaller instabilities with the main downflow
leads to a major big cold temperature anomaly (Figure 4.7 d-f).
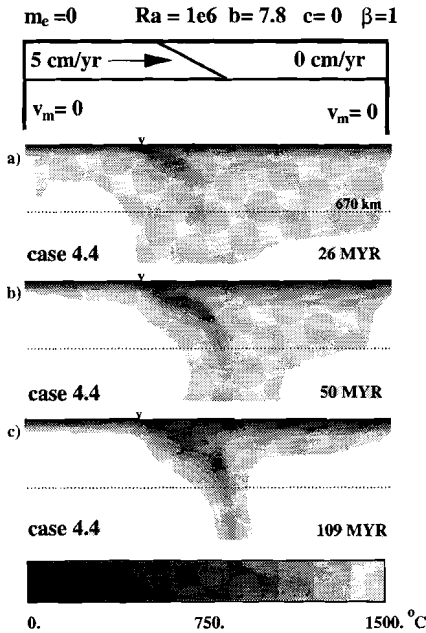
Figure 4.8 *Temperature field and sketch of plate velocities of case 4.4. The temperature dependent viscosity decreases from surface to the upper mantle by a factor of 50. The viscosity profile is shown in Figure 4.4d.*

No viscosity jump - viscosity of slabs varies - (Case 4.4: $\beta = 1$, $b = 7.8$)

In case 4.4 no increase in viscosity is employed but temperature-dependent viscosity evokes stiffness of the cold slab. Here, the viscosity decreases across the
lithosphere from surface to the mantle by a factor of 50 (Figure 4.4 d). Figure 4.8
shows the evolution of the temperature field of case 4.4. Two major differences
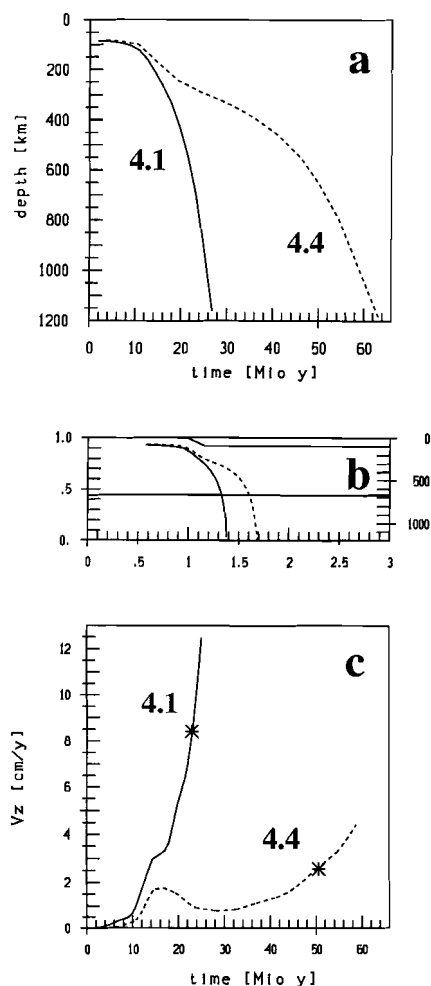can be observed between case 4.4 and case 4.1 (with constant viscosity): 1. The

Figure 4.9 *Tracer trajectory versus time (a), the trajectory of that tracer within the model domain (b), and its vertical velocity v_z versus time (c). Solid graphs indicate the trajectory of case 4.1 without stiff slab. Dashed lines represent the trajectory of case 4.4, where stiffness of the slab is given by the parameter $b = 7.8$. In the model domain b the position of the rigid plate is given. Asterisks in c indicate the time when the tracer encounters the depth of 670 km. This depth is reached by the tracer of case 4.1 ca. 28 Myr earlier than by that of case 4.4. The trajectories within the model domain (b) show that the stiff slab has a shallower dip angle in the upper mantle.*

slab stays 'horizontally' in the upper part of the upper mantle still after 100 Myr of subduction. In the previous cases (4.1-4.3), where slabs had the same viscosity as the upper mantle, the bent shape (in contrast to a straight vertical shape) which has been formed in the beginning of the descent (e.g. Figure 4.5 a,b) vanished with time (Figure 4.5 c-e). 2. The inner part of the slab is warmer than in cases with constant viscosity. The isotherms are not as densely spaced as in cases 4.1-4.3.

To be able to study flow properties of the slabs passive tracer particles are used. The algorithm for postprocessing the velocity data to obtain the trajectories of the tracer is taken from *Schmalzl and Hansen (1994)*. Only the trajectory of a single tracer was observed here: Figure 4.9 shows the depth of a single tracer versus time (a), the trajectory of that tracer within the model domain, whose starting position was within the initial plate (b), and its vertical velocity v_z versus

time (c). The solid line represents the tracer of case 4.1 with constant viscosity, the dashed graph indicates the tracer of case 4.4 with temperature-dependent viscosity. Both tracers have the same starting position. Velocity and trajectory of the tracers depend, of course, from their starting location. Comparison of other corresponding pairs of tracers gave similar results as the one presented here.

Thus, we can use the tracer trajectories for relative comparison between different cases, rather than for absolute evidence of, for example, the vertical velocity. Figure 4.9 a and c show that the tracer of the constant viscosity case 4.1 descends faster than that of case 4.4. Asterisks in Figure 4.9c indicate the time when the tracer encounters the depth of 670 km. This depth is reached by the tracer of case 4.1 ca. 28 Myr earlier than by that of case 4.4. The trajectory in Figure 4.9 b of the tracer of the stiff slab (case 4.4) is shallower than that of the constant viscous slab (case 4.1). This conclusion was already drawn from analysing the temperature structure.

Highly viscous slabs - viscosity jump varies - (Case 4.5, 4.6: b=10.6, c=0)
In cases 4.5 and 4.6 viscosity is temperature-dependent: With $b = 10.6$ the viscosity increases across the lithosphere in both cases by a factor of 200.

Case 4.5 has a 50-fold increase in viscosity at 670 km depth (Figure 4.4 e), the increase in viscosity of case 4.6 at the upper-lower mantle boundary by a factor of 300 (Figure 4.4 f) is at the upper end of expected values (*Hager and Richards, 1989*). After the slab has penetrated into the lower mantle, in both cases, the slab shows a bent structure (Figure 4.10 b and 4.11 b). The change in dip angle at 670 km depth, indicated by $\Delta\Theta$ in Figure 4.10 b and 4.11 b, is about 53° in case 4.5 and 65° in case 4.6. After another 90 Myr in both models $\Delta\Theta$ has decreased to zero which is indicated by the straight line representing the dip angle about 200 km above and below the upper-lower mantle boundary (Figure 4.10 c and 4.11 c). What is striking is that the high amount of viscosity increase even by a factor of 300 is not able to hinder the slab from penetrating through the upper-lower mantle interface. Compared to case 4.1 (no stiff slab, no viscosity jump) the shape of the temperature anomaly is broadened and the descent is about four times that slow.

Highly viscous slabs - viscosity increases continuously in the mantle - Ra varies - (Case 4.7, 4.8: b=10.6, c=4.6, β = 1)
In cases 4.7 and 4.8 increase in viscosity is not abrupt but continuously. With b=10.6 and c=4.6 the viscosity decreases across the lithosphere from surface to the mantle by a factor of 200, from there it increases exponentially. At 670 km depth the viscosity is ca. 10 times the reference viscosity η_0, at the bottom it reaches a value which is about 100 times η_0 (Figure 4.4 g). Rayleigh number is 10^6 and 10^7 in case 4.7 and 4.8, respectively. Figure 4.12 shows the time evolution of case 4.7. The descent of the slab is very slow and the temperature anomaly structure is very broad.
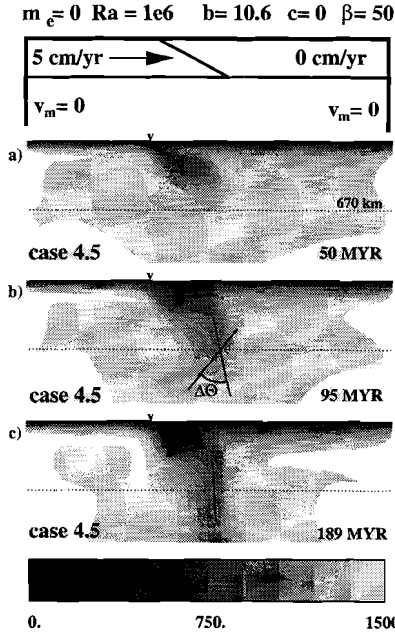
m $_e$= 0 Ra = 1e6   b= 10.6 c= 0 β= 50   m $_e$= 0 Ra = 1e6   b= 10.6 c= 0 β=300
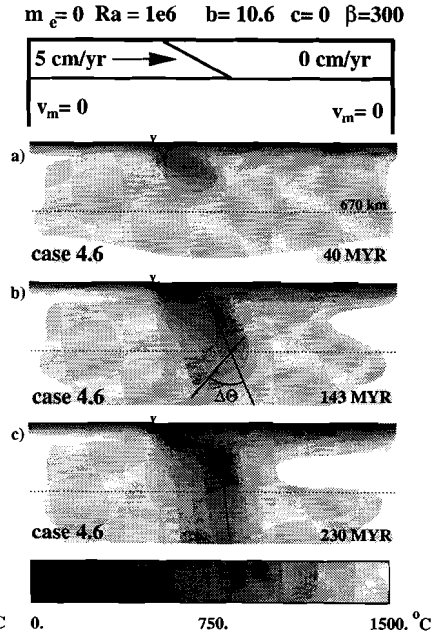

Figure 4.10   Figure 4.11

left: Evolution of the temperature field and plate velocities of case 4.5. Viscosity decreases across the lithosphere by a factor of 200, and increases at 670 km by a factor of 50. For viscosity profile see Figure 4.4e. ΔΘ indicates the change in dip angle across the 670 km discontinuity.

right: Similar to the left panel with an upper to lower mantle viscosity ratio of 300 (case 4.6). The change in dip angle at 670 km depth (ΔΘ) is greater than for case 4.5. For viscosity profile see Figure 4.4f.

The dip angle of penetration into the lower mantle does not vary significantly with time but stays constantly about 70°. The exponential increase in viscosity with depth decreases the local Rayleigh number not only in the lower but also in the upper mantle. The model run with a Rayleigh number of one order of magnitude higher (case 4.8) can be seen in Figure 4.13. The shape of the temperature anomaly is as half as thin as that of the lower Rayleigh number case 4.7. Dip angle of case 4.8 is nearly vertical. From analysing tracer trajectories (Figure 4.14) it follows that descent of the slab of case 4.8 is nearly three times as fast as that of case 4.7. A representative single tracer of case 4.8 has reached the depth of 670 km after 41 Myr, whereas the tracer of case 4.7 needs about 110 Myr to reach that depth (Figure 4.14 c). The average sinking velocity of case 4.7 is with less than 1 cm/yr

$m_e = 0cm/yr$ $Ra = 1e6$ $b= 10.6$ $c= 4.6$ $\beta= 1$

Figure 4.12

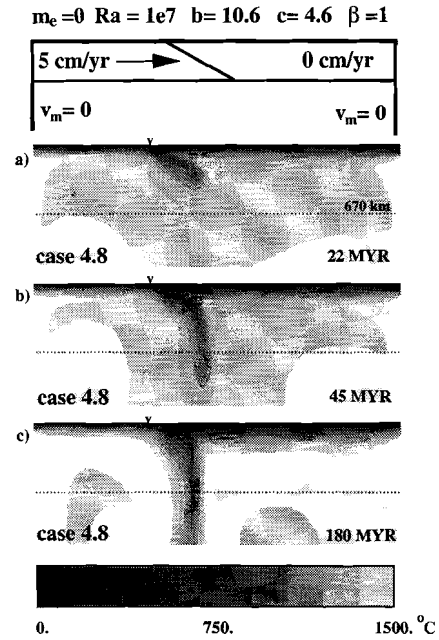$m_e = 0$ $Ra = 1e7$ $b= 10.6$ $c= 4.6$ $\beta =1$
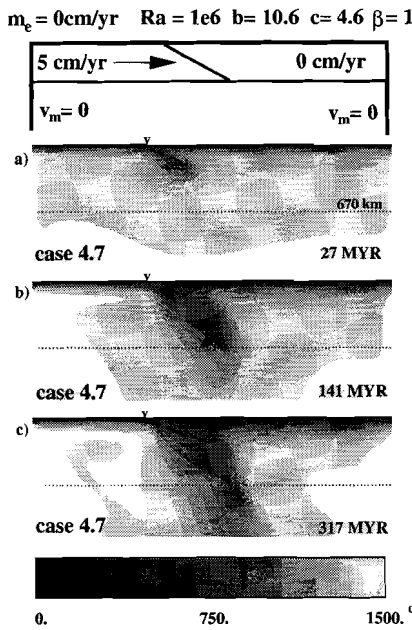
Figure 4.13

left: Evolution of the temperature field and plate velocities of case 4.7. Surface viscosity is 200 times the reference viscosity. Increase in viscosity with depth is continuous. The viscosity profile is shown in Figure 4.4g.
right: Same as left panel for Rayleigh number 10^7 (case 4.8).

too slow. In case 4.8 the tracer penetrates through the 670 km discontinuity with a vertical velocity of 3 cm/yr. The overall higher viscosity of case 4.7 - compared to case 4.8 - effects that slab descent is slower. A difference in slab geometry between cases with a viscosity jump and the cases with continuous viscosity increase with depth has not been found.

Effect of horizontal plate velocity v_u - (Case 4.9, 4.10)
Cases 4.9 and 4.10 are corresponding to the cases 4.4 and 4.5, respectively, but have a higher horizontal plate velocity which is 8 cm/yr. Case 4.9 has a stiff slab with an increase in viscosity across the lithosphere by a factor of 50, no viscosity jump at 670 km depth is implemented. The viscosity profile is shown in Figure 4.4 d. Comparing the temperature fields of case 4.9 with those of case 4.4 (see Figures 4.8 and 4.15) no significant difference in flow pattern can be observed.

Again, we observe the trajectories of single tracers - as has been done before. Figure 4.17 shows how the tracer descends with time (a), its trajectory within
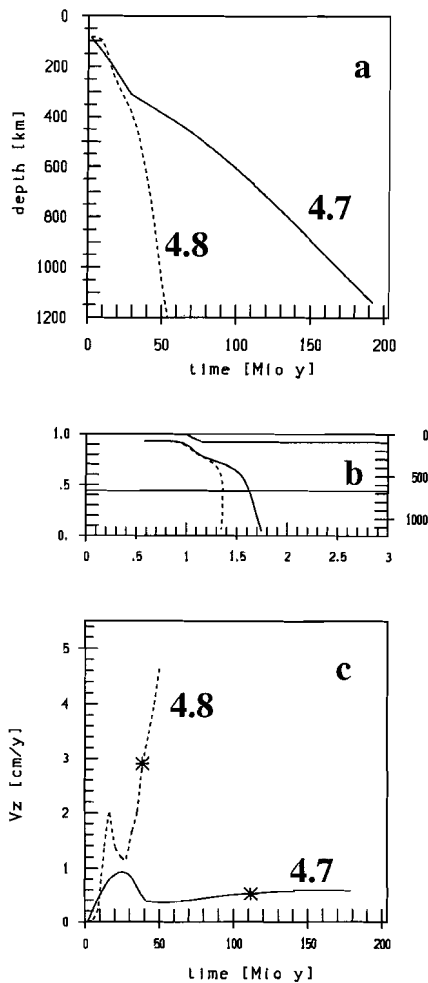
Figure 4.14 *Tracer trajectory versus time (a), the trajectory of that tracer within the model domain (b), and its vertical velocity v_z versus time (c) for case 4.7 (solid) and case 4.8 (dashed). Asterisks in (c) show vertical velocity and time when the tracer crosses the 670 km discontinuity. In both cases viscosity increases continuously with depth (below the lithosphere). Case 4.7 has a Rayleigh number (based on the reference viscosity) of 10^6, Rayleigh number of case 4.8 is 10^7. With increaseing Rayleigh number the vertical tracer velocity (c) increases.*

the model domain (b), and its sinking velocity v_z versus time (c). The solid line represents the tracer of case 4.4 with plate velocity of 5 cm/yr, the dashed graph indicates the tracer of case 4.9 with 8 cm/yr plate velocity. Hardly any difference can be seen between the two trajectories (Figure 4.17 b). Thus, the difference of 3 cm/yr in horizontal plate velocity has no major influence on the geometry of the subducting slab. The descent velocity (Figure 4.17 c) shows the difference between the two cases. Asterisks indicate the time when the tracer encounters the depth of 670 km. This depth is reached by the tracer of case 4.9 ca. 14 Myr earlier than by that of case 4.4.

The second run with 8 cm/yr plate velocity (case 4.10) is comparable (in rheology) to case 4.5. Viscosity drops in both cases by a factor of 200 across the lithosphere and increases at 670 km depth by a factor of 50. Figure 4.16 shows the temperature evolution of case 4.10. No major difference compared with case 4.5
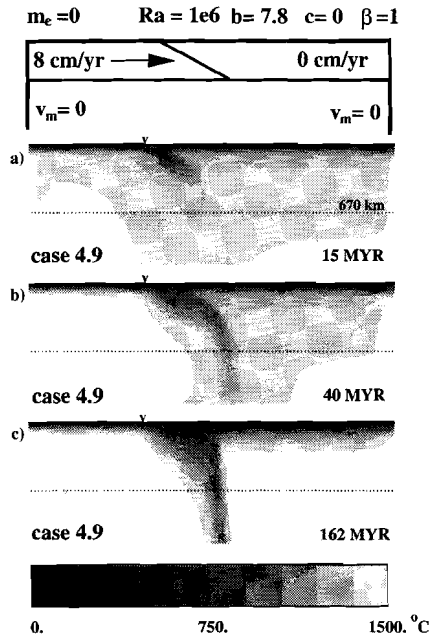
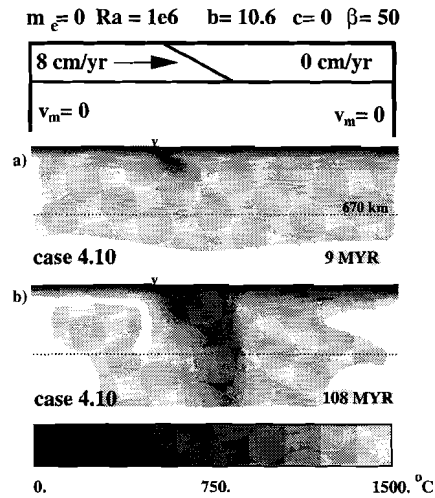$m_c = 0$ $Ra = 1e6$ $b = 7.8$ $c = 0$ $\beta = 1$

Figure 4.15

Figure 4.16

left: Temperature field and sketch of plate velocities of case 4.9, which is similar in viscosity to case 4.4, but differs in the underthrusting plate velocity ($v_u = 8\,cm/yr$). The viscosity profile is given in Figure 4.4d. The increase in plate velocity has no major effect on slab geometry.

right: Case 4.10 is similar in viscosity to case 4.5 but has a plate velocity v_u of 8 cm/yr. Figure 4.4e shows the viscosity profile. Again, the higher plate velocity has no significant influence on the subducting slab.

can be seen (cf. Figure 4.10). We again compare two single tracer trajectories of each case as described above. Figure 4.18 b shows that the trajectories on which the tracers descend are close together, but different. The trajectory is shifted ca. 100 km to the right at the upper-lower mantle boundary. Therefore the difference in vertical descent velocity is not very big: the tracer of case 4.10 reaches the 670-discontinuity only ca. 10 Myr before the tracer of case 4.5 does (Figure 4.18 c). In general the slabs of the cases 4.5 and 4.10 sink slowlier than those of cases 4.4 and 4.9 which is caused by both the higher intensity of temperature-dependence of the viscosity and a higher increase in viscosity at 670 km depth.

Effect of Ra on the descent velocity of the slab - Case 4.10, 4.11, 4.12
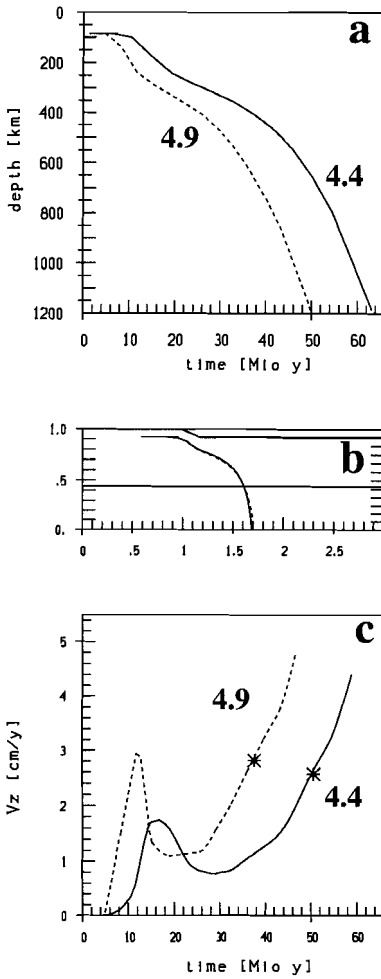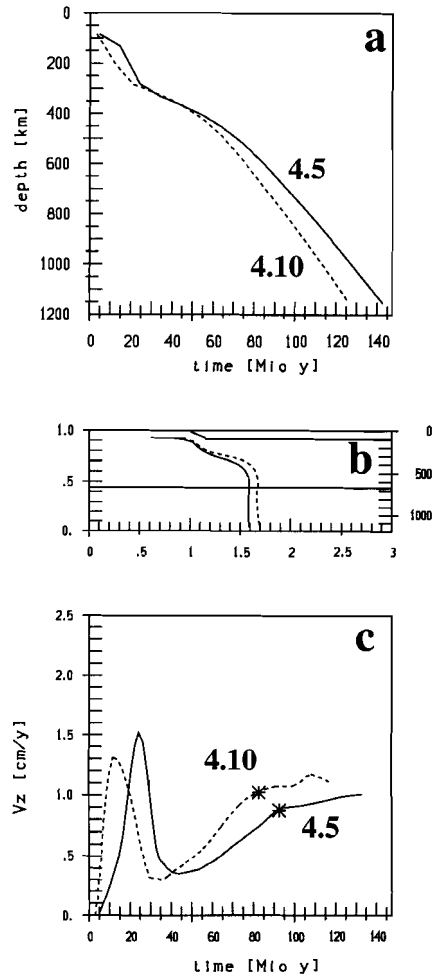The viscosity profile of case 4.11 and 4.12 is equal to that of case 4.10 (Figure 4.4

Figure 4.17   Figure 4.18

left: Tracer trajectory versus time (a), the trajectory within the model domain (b), and the sinking velocity v_z versus time (c) for a representative single tracer of case 4.4 ($v_u = 5$ cm/yr) and 4.9 ($v_u = 8$ cm/yr). Asterisks show the time and vertical velocity when the tracer crosses the 670 km depth. The later arrival of the tracer in case 4.4 at 670 km depth is caused by a later arrival at the trench (a) rather than by a lower sinking velocity (c). The tracer of case 4.4 sinks slightly slowlier than that of case 4.9.

right: Same as left panel for the cases 4.5 and 4.10, which differ in plate velocity v_u as well. Descent velocity (c) of case 4.5 with $v_u = 5$ cm/yr is slightly less than that of case 4.10 with $v_u = 8$ cm/yr (except the peak at ca. 25 Myr). The trajectory of case 4.10 (b) is shifted ca. 100 km to the right at the upper-lower mantle boundary.

c). Viscosity decreases across the lithosphere by a factor of 200 and increases at 670 km depth by a factor of 50. Underthrusting plate velocity is 8 cm/yr. The Rayleigh number is 10^6, $5 \cdot 10^6$, and 10^7 for case 4.10, 4.11, and 4.12, respectively. Temperature fields of each of the cases 4.11 and 4.12 at 37 Myr after subduction had started and at a late and quite stable stage are given in Figure 4.19 and 4.20. For the temperature field of case 4.10 see Figure 4.16. The higher the Rayleigh number the thinner and straighter is the slab structure. Figure 4.21 shows the descent of a single tracer with time (a), the tracer trajectory within the model domain (b), and the vertical tracer velocity versus time (c) for all three cases. Obviously, with increasing Rayleigh number the descent velocity of the tracer, and therewith the descent of the slab, increases. The tracer of case 4.10 ($Ra = 10^6$) penetrates into the lower mantle with 1 cm/yr, that of case 4.11 ($Ra = 5 \cdot 10^6$) with nearly 3 cm/yr, and that of case 4.12 ($Ra = 10^7$) with more than 5.5 cm/yr (Figure 4.21 c).
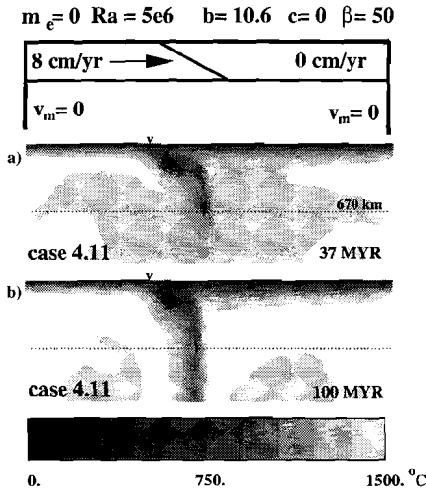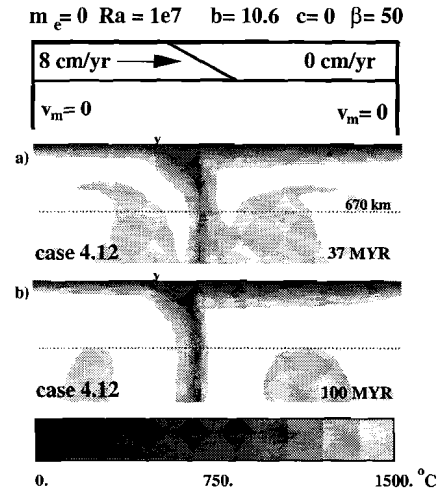

Figure 4.19   **Figure 4.20**

left: Evolution of the temperature field and sketch of plate velocities of case 4.11. Similar to case 4.10 but with a Rayleigh number of $5 \cdot 10^6$. Viscosity profile can be seen in Figure 4.4e.

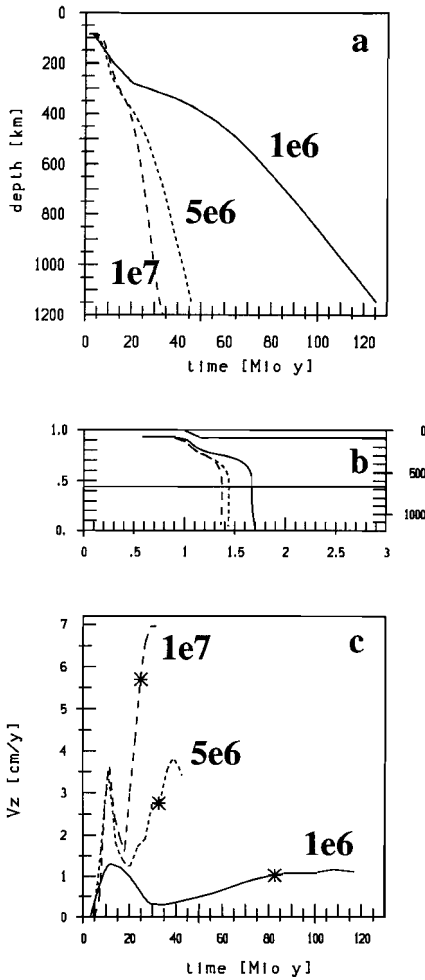*right: Similar to the left panel but with Rayleigh number of 10^7 (case 4.12).*

Figure 4.21 *Tracer trajectory versus time (a), the trajectory of that tracer within the model domain (b), and its vertical velocity v_z versus time (c) for case 4.10 (solid), case 4.11 (dashed), and case 4.12 (dashed). Asterisks in (c) show vertical velocity and time when the tracer crosses the 670 km discontinuity. With increasing Rayleigh number vertical velocity of the tracer increases.*

Seismic velocity anomaly

Two groups of experiments have been selected to be converted to the seismic P-wave velocity anomaly. With the first group we wanted to study whether the viscosity of the slabs influence the seismic velocity anomaly. Secondly, we were interested whether there is an effect of the Rayleigh number on the seismic velocity anomaly.

Cases without temperature-dependent viscosity provide lower temperature anomalies of the subducted slab than models with highly viscous lithosphere do. This must have an effect on the seismic velocity anomaly. To investigate the difference in magnitude of the seismic P-wave velocity anomaly between these models we have converted the model temperature of cases 4.1, 4.3, and 4.4 to the seismic velocity anomaly as has been described in chapter 3.3. In Figure 4.22 a,b, and c the v_p- anomalies resulting from the temperature fields illustrated in Figures
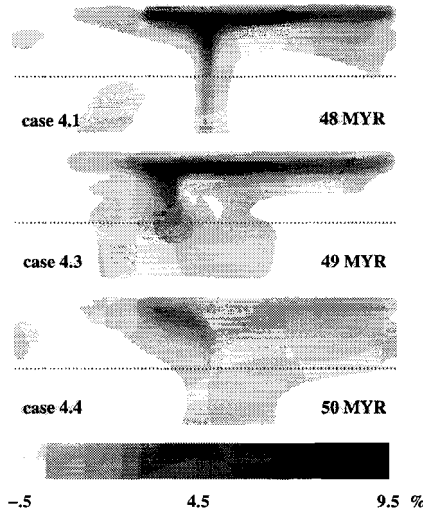
Figure 4.22 *Seismic p-wave velocity anomaly of the model temperature illustrated in Figure 4.5c, 4.7c, and 4.8b.*

4.5c, 4.7c, and 4.8b, respectively, are shown. The velocity anomalies reach 9 % in the cases 4.1 and 4.3, whereas for case 4.4 values up to 6 % (Figure 4.22c). Compared with seismic velocity images the magnitudes of the anomalies in cases, where high viscosity slabs are absent, are too high. Values up to 6 % are still high, but more suitable to observed values. However, these high magnitudes appear only at depths between 100 and 250 km, where temperature difference between the cold slab (just subducted) and the ambient mantle material is greatest. Moreover, the sensitivity of the seismic velocity anomaly to temperature decreases with depth (see chapter 3.3).

From our temperature models we found that the Rayleigh number has two major effects on the evolution of the subducting slab: With increasing Rayleigh number slab descent becomes faster and the shape of the temperature anomaly becomes thinner. Figure 4.23 shows the seismic velocity anomalies for case 4.10, 4.11, and 4.12. The corresponding temperature fields can be seen in Figure 4.16, 4.19, and 4.20 (except for case 4.10 at 37 Myr). 37 Myr after subduction penetration depth of each case is different. Whereas the slab of case 4.10 ($Ra = 10^6$) is still in the upper mantle (Figure 4.23a), the slab of case 4.11 ($Ra = 5 \cdot 10^6$) has entered the lower mantle ((Figure 4.23c), and the slab of case 4.12 ($Ra = 10^7$) has crossed the whole depth of the box (Figure 4.23e). The right panels show Δv_p at a later stage at about 100 Myr. What is striking is that amplitudes do not vary significantly. At early stages as well as at late stages, low Rayleigh number cases as well as high Rayleigh number cases show magnitudes up to 7.5 %. Again the

highest magnitudes of Δv_p are found between ca. 100 and 250 km depth. In the lower mantle seismic velocity anomalies are up to about 2.5 %.
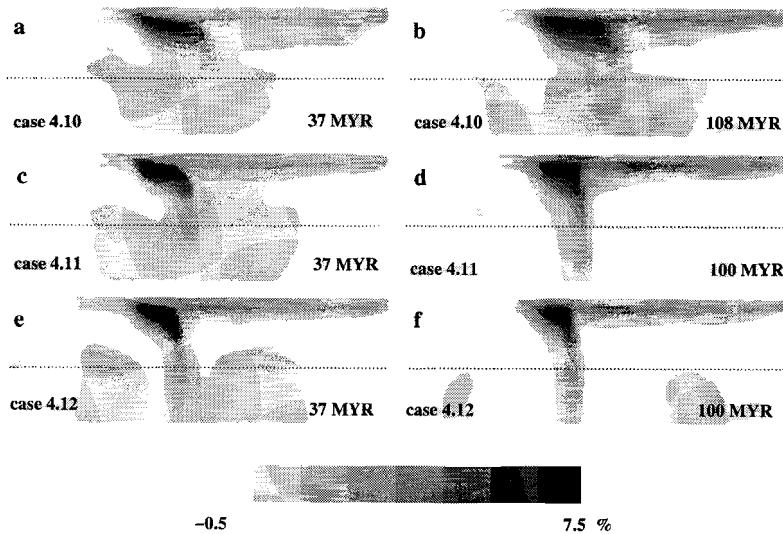

Figure 4.23 *Seismic p-wave velocity anomaly of the model temperature illustrated in Figure 4.16, 4.19, and 4.20 (no temperature field is shown for case 4.10 at 37 Myr).*

In general the values of the seismic velocity anomaly are slightly too high in the upper mantle, but consistent with observed values in the lower mantle.

4.4 Discussion

With our model runs we investigated four items: First, what is the effect of just an increase in viscosity on the downgoing slab? Second, which role does the stiffness of the slab play? Third, what are the effects of the horizontal plate velocity of the subducting plate? Fourth, what does a change in Rayleigh number (or reference viscosity) evoke? With cases 4.1-4.3 and 4.5, 4.6 we could demonstrate that a viscosity increase alone is not able to hinder a subducting slab from penetrating into the lower mantle. Even the increase in viscosity by a factor of 300 - which is at the upper end of expected values (*Hager and Richards, 1989*) - only slows down the descent of the slab, but allows it to penetrate through the transition zone nearly vertically. Shortly after penetration into the lower mantle the slab shows a kink in dip. For a lower to upper mantle viscosity ratio of 50 ($\beta = 50$) the slab dip

increases by ca 53°, for a ratio of 300 by ca. 67° (Figure 4.10b, 4.11b). The amount of change in dip angle is higher than predicted by *Gurnis and Hager (1988)*. However, this kink vanishes with time when the slab sinks 'through' the bottom (Figure 4.10c, 4.11c). *Gurnis and Hager (1988)* numerically modelled subducting slabs in a mantle with a viscosity contrast up to 100. Their two-dimensional model including temperature-dependent viscosity and a viscosity jump at 670 km depth is adequate to ours, but differs in boundary conditions. They employ no imposed plate velocities and - the main difference - do have a closed bottom. Thus, in our model, the possibility for mantle material 'to flow through the bottom' causes the decrease of change in slab dip to zero.

Stiffness of the slab due to temperature dependence of the viscosity leads to a kink in dip within the upper 400 km, but 100 km above and below the 670 km discontinuity slab dip develops to be the same. The flexured slab structure in the upper mantle is apparent whether viscosity increases with depth abrupt (case 4.5, 4.6), continuously (case 4.7, 4.8), or not at all (case 4.4). Stiff slabs sink slower into the mantle (compare case 4.1 and case 4.4) which is in agreement with results from *Zhong and Gurnis (1995)*. They found that an increase in slab viscosity relative to the transition zone by a factor of 10 decreases the ability of penetration through a phase boundary and the slab needs more time to sink. Results from studies done by *Zhong and Gurnis (1994)*, *Davies (1995)*, and *Christensen (1996)* indicated that high viscosity slabs penetrate more easily through a phase boundary.

An increase in plate velocity from 5 to 8 cm/yr increases the descent velocity of the subducting slab slightly. Representative tracer trajectories of cases with $v_u = 5$ cm/yr arrived about 10 Myr later than those with $v_u = 8$ cm/yr. However, this delay occurs, because the tracer of less horizontal velocity reaches the trench later, rather than because of different vertical velocity. The geometry is not affected strongly. This has been tested for slabs with different intensity of temperature-dependence of viscosity and different increase in viscosity at 670 km depth.

The descent velocity of the slabs is strongly influenced by the Rayleigh number - and therewith by the reference viscosity. With increasing Rayleigh number the vertical velocity of the descending slab increases. A highly viscous slab at Rayleigh number 10^6 encountering a viscosity interface - with upper to lower mantle viscosity ratio of 50 - sinks with ca. 1 cm/yr. The subducting slab of the corresponding Rayleigh number 10^7 case reaches a vertical velocity component at 670 km of nearly 6 cm/yr. Descent velocity of slabs also depends on the age and dip angle of the slab (e.g. *Wortel and Vlaar, 1988*). They vary between 2 cm/yr (e.g. Central America) and 6 cm/yr (e.g. NW Pacific; *Jarrard, 1986*). That means that for our model set up 10^6 yields a lower and 10^7 an upper limit for the Rayleigh number. Slab geometry is also affected by the Rayleigh number. With increasing Rayleigh number (decrease in reference viscosity) the subducted slab is bent closer to the trench (see tracer trajectory in Figure 4.14b and 4.21b).

Conversion of the model temperature to the seismic P-wave velocity anomaly has shown that isoviscous slabs evoke higher magnitudes than highly viscous slabs. However, with increase in intensity of temperature dependence of the viscosity (from a 50-fold to a 200-fold surface viscosity of η_0) no further decrease in maximum magnitude of Δv_p was found. The overall viscosity controled by the Rayleigh number (or reference viscosity) has no effect on the magnitude of the seismic velocity anomaly. In general, amplitudes of the slabs in the upper half of the upper mantle are with about 7% too high compared to observed values. In the lower mantle the seismic velocity anomalies are with values up to 2-3% consistent with tomography results.

Despite some differences between the model runs, the great variety observed by seismic imaging cannot be explained by varying the viscosity increase with depth, the stiffness of the slabs, or the plate velocity of the underthrusting plate (when considering a fixed overriding plate). The first three experiments (case 4.1-4.3) show that temperature-dependent viscosity should be included in the modelling of subducting plates - otherwise plume-like behaviour rather than slab-like behaviour is the result. Slab structures as provided by slabs of constant viscosity (i.e. no temperature-dependent viscosity) are not observed by e.g. tomographic imaging (cf. Figure 2.1, 7.1, 8.5).

4.5   Conclusions

From our two-dimensional modelling we found that a viscosity interface alone - even with a viscosity ratio between lower and upper mantle viscosity of 300 - is not able to prevent a subducting slab from entering the lower mantle. While entering the more viscous layer the slabs show a kink or flattening in their geometry. However, the change in dip angle across the viscosity boundary is compensated with time. Stiffness of the slabs, realized by temperature-dependent viscosity, produces a more slab-like behaviour, as e.g. the bent shape in the upper mantle. An increase of the underthrusting plate velocity from 5 to 8 cm/yr does not change slab geometry, descent velocity of the slab is slightly (ca. 0.5 cm/yr) increased. With increasing Rayleigh number (decrease in reference viscosity) vertical slab velocity increases. Slabs from $Ra = 10^7$-cases can sink about four times as fast as slabs from $Ra = 10^6$-cases. Seismic P-wave anomalies of models without stiff slabs are up to 9%, which is too high compared with seismic images. Stiff slabs (i.e. including temperature-dependent viscosity) provide seismic P-wave anomalies up to 7%, which is closer to the range of observed values. The Rayleigh number (reference viscosity) does not affect the magnitude of the seismic velocity anomaly. Thickness of the slab's temperature structure, and therewith the shape of the seismic velocity anomaly structure, decreases with increasing Rayleigh number. Observed tomography structures associated with subducted slabs are consistent

with an intermediate thickness (between structures of $Ra = 10^6$ and $Ra = 10^7$).

From these results we conclude that temperature-dependent viscosity supports slab-like behaviour - distribution and magnitude of temperature anomaly - and therefore has to be considered in the modelling of subducting slabs. Both descent velocity of slabs and the shape of the seismic velocity anomaly support that for our model set up 10^6 yields a lower and 10^7 an upper limit for the Rayleigh number. Seismic velocity anomalies are about 1-2% too high - mainly in the upper part of the slabs - compared with observed values.

Finally we can say that the great variety observed in seismic velocity structures beneath subduction zones cannot be explained by variations in viscosity, plate velocity, and Rayleigh number (reference or overall viscosity) alone. Therefore other properties have to be considered in the modelling for the understanding of the subduction process.

CHAPTER 5

Trench migration and subduction zone geometry

5.1 Introduction

In chapter 4 we showed that viscosity affects the descent velocity and the magnitude/distribution of the temperature anomaly, and therewith the seismic velocity anomaly, rather than the general penetration depth. It has been found that temperature-dependent viscosity is compulsory for the modelling of slabs. Varying the ratio of lower to upper mantle viscosity alone cannot provide the great variety observed in subduction zone geometry. As has been pointed out in section 2.4 in most of the subduction zones not only the underthrusting, but also the overriding plate moves with a few centimeters per year, which is often a retrograde motion, i.e. the trench moves towards the subducting plate. Two types of mechanism cause this net horizontal motion of the trench. First, the slab sinks under its own weight, so that the hinge (trench) moves backwards (roll back). Second, the underthrusting plate is forced to sink by the overriding plate. The trench is localized at the leading edge of the overriding plate and moves therewith towards the underthrusting one.

Van der Hilst and Seno (1993) postulated that the difference in slab structure revealed by seismic imaging beneath Izu Bonin and the Mariana arc, showing a stagnant and a penetrating slab, respectively, can be explained by the different rate of trench migration. The variation in slab geometry along the trench system in the Tonga region as revealed by tomographic images is also explained by difference in trench migration rate (*Van der Hilst, 1995*). In this chapter we demonstrate that trench migration has a major effect on the dynamics of subduction zones.

For the analysis of the effect of trench migration on the subduction process background mantle flow becomes important (*Ricard et al., 1991*). Not only absolute plate/trench velocities, such as specified by e.g. the hotspot reference frame, but also relative motions between surface velocities and the mantle fow beneath must be considered. *Ricard et al. (1991)* suggest that the mantle flow has a global eastward motion of about 1 cm/yr relative to the - westward drifting - lithosphere. This implies that subduction zone geometry might differ between east and west dipping subduction zones, particularly the dip angle of the subducting lithosphere (*Doglioni, 1990; Doglioni et al., 1991*).

This chapter is organized in the following way: After introducing the model, three result sections are presented. In the first part (5.3) we investigate the effect of variation in viscosity on subduction, but contrary to chapter 4, while trench migration is present. In the second part (5.4) we choose one viscosity profile on the base of results from chapter 4 and 5.3 to probe in detail the effect of trench migration on the subduction process. Comparison between west and east dipping subduction zones is subject of the third part (5.5). These results are then summarized in chapter 5.6.

5.2   The Model

In addition to the model already described in chapter 4.2 a background mantle flow and a movable overriding plate are included. Figure 5.1 illustrates the extended version of the model. The arrows at the vertical boundaries indicate the horizontal mantle flow (v_m) which can be imposed at the sidewalls. Our model allows a
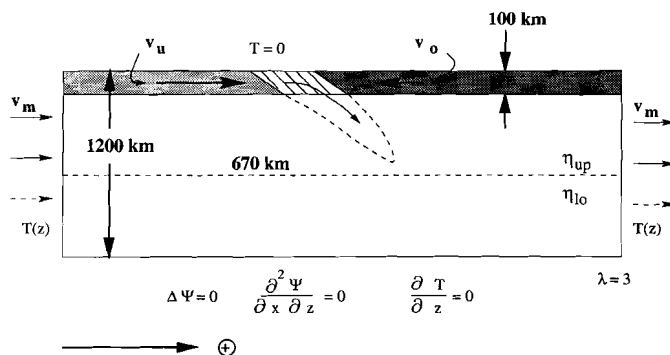
Figure 5.1 *Scheme of the model geometry. In addition to the model used in chapter 4 (cf. Figure 4.2) a background mantle flow (v_m) can be included. The arrows at the vertical boundaries indicate the horizontal background mantle flow. The dashed arrow at the lower mantle boundary indicates that the horizontal mantle flow can decrease with depth, for example, due to increase in viscosity. A second extension of the model is the movable overriding plate. Its velocity v_o is not necessarily zero. With the motion of the overriding plate trench migration is included. Since no back-arc extension is employed the trench migration rate is equal to the overriding plate velocity v_o. Additional, we define the effective trench migration rate m_e as the rate of trench migration (v_o) relative to the upper mantle flow (v_m): $v_o - v_m = m_e$. The arrow at the bottom marks the direction of positive horizontal velocities. ψ is the streamfunction. η_{up} and η_{lo} are the upper and lower mantle viscosity, respectively. For other parameters see Figure 4.2.*

decrease of the background mantle flow with depth, which is indicated by the dashed arrows along the sidewalls. A reason for the decrease in v_m could be the increase in viscosity at 670 km depth. Trench migration is included through the motion of the overriding plate. Since no back-arc extension is employed the trench migration rate is equal to the overriding plate velocity v_o. Additional, we define the *effective* trench migration rate m_e as the rate of trench migration (v_o) relative to the upper mantle flow (v_m): $v_o - v_m = m_e$ (cf. *Tao and O'Connell, 1992*).

5.3 The effect of viscosity structure on subduction under the consideration of trench migration

In this section not only the parameters controling the temperature- and depth-dependence of the viscosity are varied, but also the trench migration is included. In the next section (5.4) the effect of trench migration on the subduction zone geometry will be the major aspect.

5.3.1 Results

Table 5.1 summarizes the model runs discussed in this chapter. The convergence velocity between overriding and underthrusting plate is 8 cm/yr in any case. b, c, and β parameterize the viscosity as given by equation (4.1) in chapter 4.2. m_e, v_u, and v_o is the trench migration rate, the plate velocity of the underthrusting and of the overriding plate, respectively.

Table **5.1** *Summary of Models*

case	b	c	β	v_u (cm/yr)	v_o (cm/yr)	v_m (cm/yr)	m_e (cm/yr)	Ra
5.1	4.6	0	50	7	-1	0	-1	10^6
5.2	10.6	0	50	7	-1	0	-1	10^6
5.3	13.8	0	50	7	-1	0	-1	10^6
5.4	10.6	0	10	8	0	1	-1	10^6
5.5	10.6	0	50	8	0	1	-1	10^6
5.6	10.6	0	100	8	0	1	-1	10^6
5.7	10.6	0	1	6	-2	0	-2	10^6
5.8	10.6	4.6	1	6	-2	0	-2	10^6
5.9	10.6	0	50	6	-2	0	-2	10^6
5.10	10.6	0	10	8	0	1	-1	10^7
5.11	10.6	0	50	8	0	1	-1	10^7
5.12	10.6	0	100	8	0	1	-1	10^7
5.13	10.6	0	10	6	-2	0	-2	10^7
5.14	10.6	4.6	1	6	-2	0	-2	10^7
5.15	10.6	0	100	6	-2	0	-2	10^7

(i) Rayleigh number $= 10^6$

Effect of the stiffness of the slab, Case 5.1-5.3: $\beta = 50, c = 0$
In the first three cases 5.1-5.3 the parameter b which controls the degree of
temperature-dependence of the viscosity has been varied. In cases 5.1, 5.2 and
5.3 viscosity decreases across the thermal boundary layer from the surface to the
mantle by a factor of 10, 200, and 1000, respectively. Viscosity increase at the
670 km discontinuity is 50-fold (Figure 5.2 a). The overriding plate moves with
-1 cm/yr towards the underthrusting plate, which has a velocity of 7 cm/yr. No
background mantle flow is included so that an effective trench migration rate of
-1cm/yr takes place. Figure 5.3, 5.4, and 5.5 show the evolution of the temperature
field of case 5.1, 5.2, and 5.3, respectively. There are three characteristics which are
affected by the temperature dependence of the viscosity. First, the temperature
anomaly has a broader shape the stronger the viscosity depends on temperature.
With higher viscosity - within the cold slab - the local Rayleigh number decreases,
which is probably the reason for the observed feature. Second, with increase
in temperature dependence of the viscosity, the change in slab dip with depth
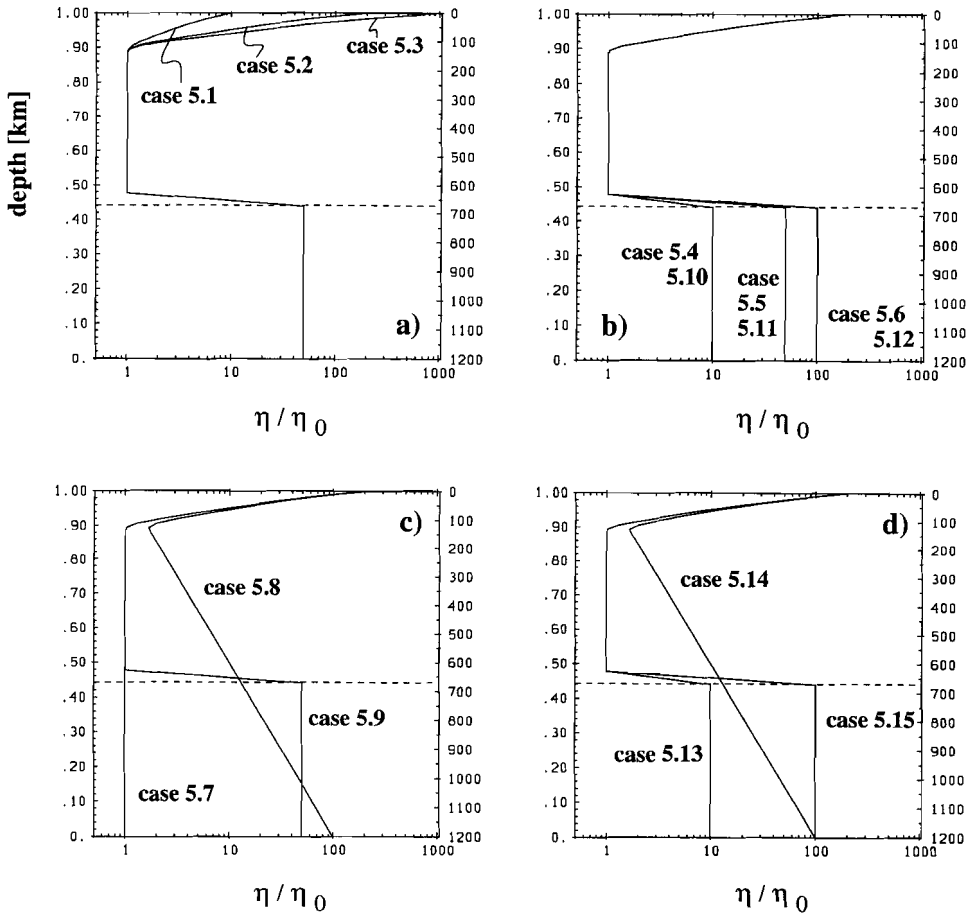becomes bigger, i.e. the slab dip becomes shallower. Figure 5.3b (case 5.1) shows a

Figure 5.2 *Viscosity profiles for cases 5.1-5.3 (a), 5.4-5.6 (b), and 5.7-5.9 (c) at a temperature profile given in Figure 4.3 (chapter 4).*

slightly 'convex' bending of the slab, whereas the slab structure of case 5.3 (Figure 5.5 b) is a 'concave' type. This means that the stiffness of the slab decreases the ability of penetration into the lower mantle. Third, the descent of the stiffer slab is slower. The effect of the stiffnes of the slabs has been already established in chapter 4. These results are not affected by the trench migration of -1 cm/yr.

Effect of increase in viscosity with depth with $m_e = -1cm/yr$, *Case 5.4-5.6*
In case 5.4, 5.5, and 5.6 the viscosity increases at 670 km depth by a factor of 10, 50, and 100, respectively. With $b = 10.6$ surface viscosity is 200 times the reference viscosity η_0 (Figure 5.2 b). The subducting plate moves in any of these three cases with 8 cm/yr towards the fixed overriding plate. A background mantle flow of 1 cm/yr is included, so that the trench migrates effectively with -1cm/yr.

$m_e = -1$ Ra = 1e6 b= 4.6 c= 0 β= 50

7 cm/yr ⟶ ⟵ -1 cm/yr

$v_m = 0$ $v_m = 0$

a)

670 km

case 5.1 22 MYR

b)

case 5.1 157 MYR

0. 750. 1500. °C

Figure 5.3

$m_e = -1$ Ra = 1e6 b= 10.6 c= 0 β= 50

7 cm/yr ⟶ ⟵ -1 cm/yr

$v_m = 0$ $v_m = 0$

a)

670 km

case 5.2 22 MYR

b)

case 5.2 165 MYR

0. 750. 1500. °C
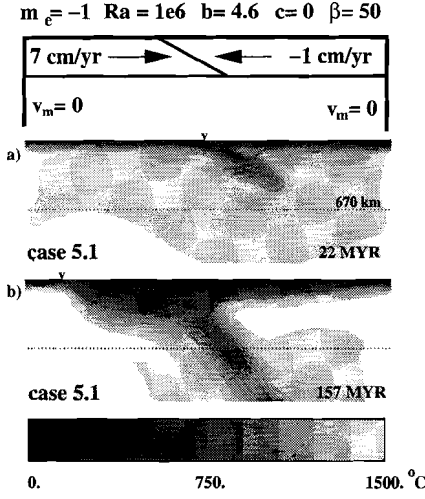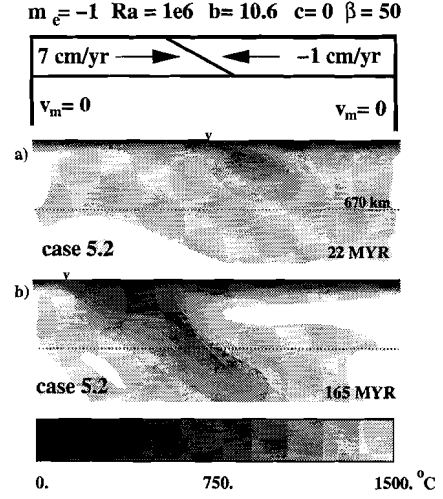
Figure 5.4

left: Evolution of the temperature field and sketch of plate velocities of case 5.1. Surface viscosity is 10 times η_0, viscosity increases at 670 km depth by a factor of 50. Rayleigh number is 10^6. Effective trench migration rate is -1 cm/yr. For viscosity profile see Figure 5.2 a. The model geometry is given in Figure 5.1.
right: As Figure 5.3 for case 5.2, where surface viscosity is 200 times η_0. (see Figure 5.2 a).

$m_e = -1$ Ra = 1e6 b= 13.8 c= 0 β = 50

7 cm/yr ⟶ ⟵ -1 cm/yr

$v_m = 0$ $v_m = 0$

a)

670 km

case 5.3 23 MYR

b)

case 5.3 189 MYR

0. 750. 1500. °C
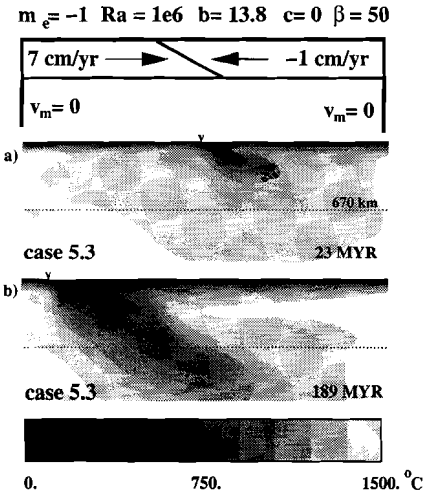
Figure 5.5 *As Figure 5.3 for case 5.3, where surface viscosity is 1000 times η_0. (see Figure 5.2 a).*

Figure 5.6 shows a sketch of plate velocities and the evolution of the temperature field of case 5.4. The slab penetrates the lower mantle with a dip angle of about 70° until the bottom is reached (Figure 5.6a). Afterwards the dip angle decreases to about 40° (Figure 5.6b). The slab of case 5.5, in which the viscosity increases at the upper-lower mantle boundary by a factor of 50, also penetrates the lower mantle, but with a smaller dip angle of ca. 40° (Figure 5.7a). During the further development the slab bends, so that the dip angle decreases to about 30° (Figure 5.7b). In Figure 5.8 the development of the temperature anomaly of case 5.6 is displayed. The ratio of lower to upper mantle viscosity is here 100. The subducting slab can still enter the lower mantle, but its descent is slower than in the previous two cases.
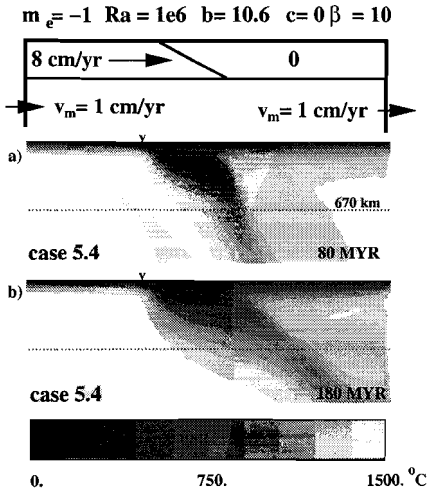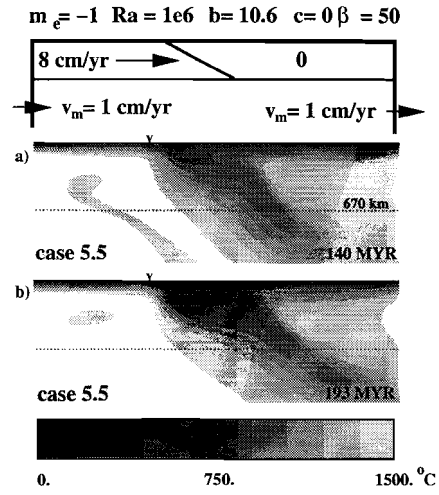
Figure 5.6 **Figure 5.7**

left: Evolution of the temperature field and sketch of plate velocities of case 5.4. Due to temperature- dependence viscosity decreases from surface to the upper mantle by a factor of 200. At 670 km depth viscosity increases by a factor of 10. Effective trench migration rate is -1 cm/yr. Rayleigh number is 10^6. For viscosity profile see Figure 5.2 b.

right: As Figure 5.6 for case 5.5. Viscosity increases at the upper lower mantle boundary by a factor of 50.

For studying the flow properties passive tracer particles have been used (*Schmalzl and Hansen, 1994*). (For description see chapter 4.) Figure 5.9 shows the depth of a single tracer versus depth (a), the trajectory of the tracer within space (b), and its vertical velocity v_z versus time (c) of case 5.4 - 5.6. The numbers in Figure 5.9 a and c give the ratio between upper and lower mantle viscosity. With increasing viscosity jump at 670 km depth the penetration angle into the deep mantle becomes

shallower and descent velocity decreases. The asterisks in c indicate the time and vertical velocity when the tracer encounters the depth of 670 km. The cases 5.4-5.6 show that with the presence of trench migration (-1cm/yr) the increase in viscosity at 670 km depth affects the slab behaviour. With increasing ratio of upper to lower mantle viscosity the dip angle of the subducting slab becomes smaller. Without trench migration (see chapter 4) a change in viscosity ratio did not affect the dip angle significantly.
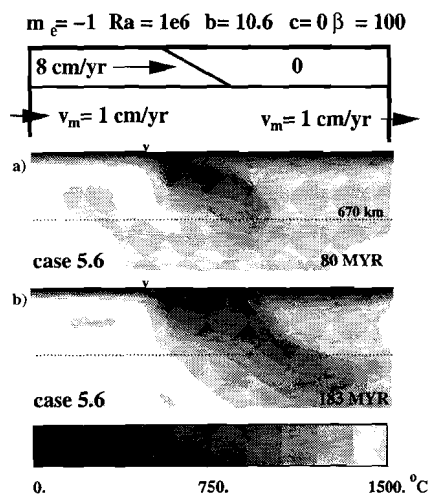

Figure 5.8 As Figure 5.6 for case 5.6. Viscosity increases at 670 km depth by a factor of 100.

Effect of increase in viscosity with depth with $m_e = -2cm/yr$, Case 5.7-5.9
In the cases 5.7-5.9 the increase in viscosity with depth varies. With $b = 10.6$ in any of the three cases the viscosity decreases across the initial lithosphere by a factor of 200. Viscosity profiles of each of these three cases is shown in Figure 5.2 c. The underthrusting plate has a velocity of 6 cm/yr, the overriding plate moves with -2 cm/yr towards the former. Since no background mantle flow is included, an effective trench migration of -2 cm/yr takes place. In case 5.7 the viscosity is only temperature dependent. No viscosity increase at the upper lower mantle boundary is applied. In case 5.8 a smooth viscosity increase is given through the factor $c = 4.6$, whereas no viscosity jump occurs. At 670 km depth the viscosity is about 10 times the reference value η_0. The increase in viscosity of case 5.9 is stepwise by a factor of 50 at 670 km depth (Figure 5.2 c). Figure 5.10 shows the temperature field of case 5.7 at different time steps. The evolution of the temperature structure is strongly time-dependent. In the first phase the slab can penetrate into the lower mantle (Figure 5.10 a,b). The anomaly is then stretched and thinned. This
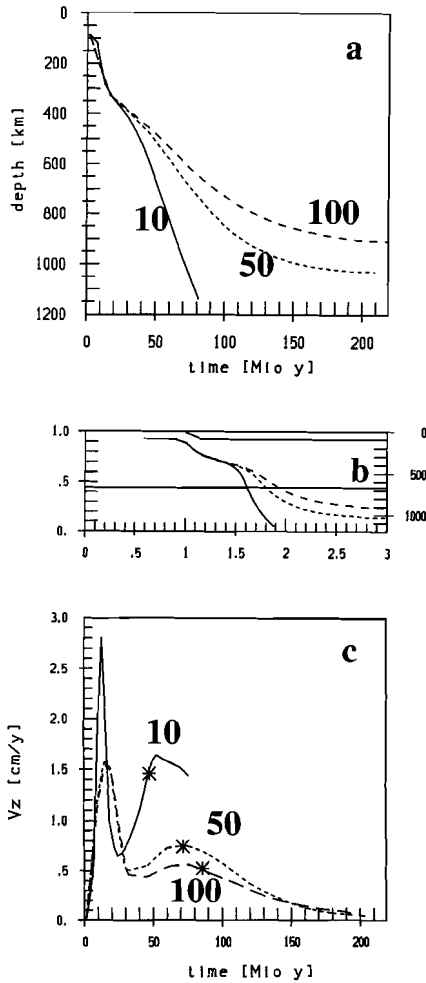
Figure 5.9 *Tracer trajectory versus time (a), the trajectory of that tracer within the model domain (b), and its vertical velocity v_z versus time (c) for case 5.4 ($\eta_{lo}/\eta_{up} = 10$), case 5.5 ($\eta_{lo}/\eta_{up} = 50$), and case 5.6 ($\eta_{lo}/\eta_{up} = 100$). ($\eta_{lo}/\eta_{up}$ is given in (a) and (c). In the model domain b the position of the rigid plate is given. Asterisks in c indicate the time when the tracer encounters the depth of 670 km. This depth is reached by the tracer of case 5.4 nearly 40 Myr earlier than by that of case 5.6. With increasing lower to upper mantle viscosity ratio dip angle decreases (b).*

thinned part of the anomaly becomes nearly horizontal until it is nearly detached (Figure 5.10 c,d). During that process a new instability is formed which becomes unstable and descends in a flushing event (Figure 5.10 d). In both the cases 5.8 and 5.9 (Figure 5.11 and 5.12, respectively) the coupled effect of trench migration and viscosity increase lead to a shallow dip angle of the descending slab. The temperature anomaly is accumulated near the upper-lower mantle boundary and can hardly penetrate it. Even the continuous increase in viscosity of case 5.8 does not allow the slab to sink into the lower mantle.

Effect of trench migration, Case 4.10 (chapter 4), 5.2,5.5, 5.9
The cases 4.10 (from chapter 4), 5.2, 5.5 and 5.9 have all the same rheology: Surface viscosity is 200 time the reference visosity and viscosity increases at 670 km depth by a factor of 50. However, they differ in trench migration rate and absolute plate
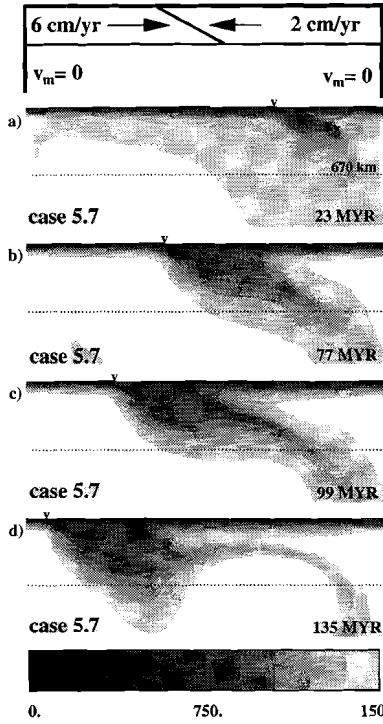
$m_e = -2cm/yr$ Ra = 1e6 b= 10.6 c= 0 β= 1

Figure 5.10

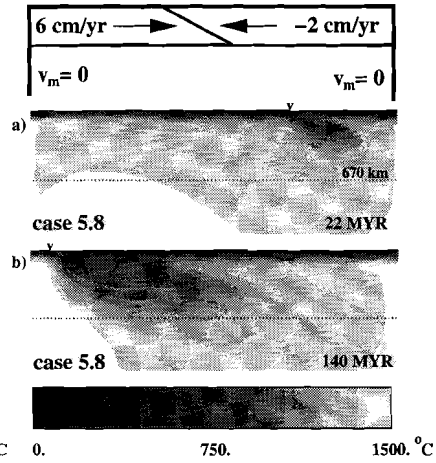$m_e = -2$ Ra = 1e6 b= 10.6 c= 4.6 β = 1

Figure 5.11

left: Evolution of the temperature field and sketch of plate velocities of case 5.7. Surface viscosity is 200 times η_0, viscosity is constant with depth. Rayleigh number is 10^6. Effective trench migration rate is -2 cm/yr. For viscosity profile see Figure 5.2 c.
right: As Figure 5.10 for case 5.8, where viscosity increases with depth continuously. At 670 km depth viscosity is about 10 times η_0. (Figure 5.2 c).

velocities. The descending slab of case 4.10, where no trench migration takes place, enters the lower mantle nearly perpendicular (Figure 4.14b). Cases 5.2 and 5.5 have both an effective trench migration rate of -1 cm/yr, but different absolute plate velocities (see top panel of Figure 5.4 and Figure 5.7 for case 5.2 and case 5.5, respecively). Note that in case 5.5 a background mantle flow of 1 cm/yr is included which evokes the effective trench migration rate. These two cases have a similar - but not identical - temperature structure, despite the different absolute plate velocities. An increase in trench migration rate to -2 cm/yr as in case 5.9 decreases the dip angle of the descending slab significantly. Figure 5.12 shows that
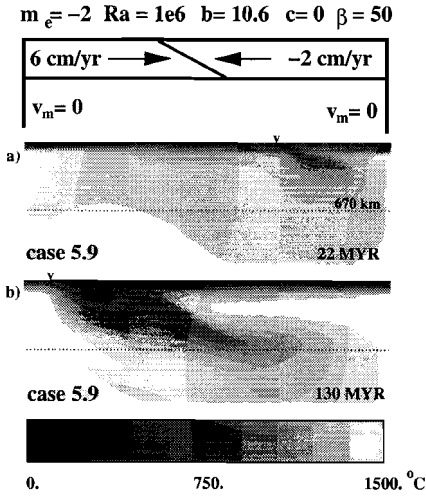
$m_e = -2$ Ra = 1e6 b= 10.6 c= 0 β = 50

case 5.9

Figure 5.12 *As Figure 5.10 for case 5.9. Lower to upper mantle viscosity ratio is 50 (Figure 5.2 c).*

the slab cannot entirely penetrate through the 670 km discontinuity.

(ii) Rayleigh number $= 10^7$

Effect of η_{lo}/η_{up} *with* $m_e = -1$ *cm/yr,* $Ra = 10^7$ *- Case 5.10 - 5.12*

Cases 5.10, 5.11, and 5.12 have a highly viscous slab (surface viscosity is $200\eta_0$), a Rayleigh number of 10^7, and an upper to lower mantle viscosity ratio of $10, 50$, and 100, respectively (Figure 5.2 b). Velocity of the underthrusting plate is 8 cm/yr, the overriding plate is fixed, and the background mantle flow is imposed to 1 cm/yr at the sidewalls. Hence, the effective trench migration rate is -1 cm/yr. Figure 5.13-5.15 shows the evolution of the temperature field of the three cases. Each of the subducting slabs penetrates into the lower mantle, but dip angle decreases with increasing viscosity jump at 670 km depth. Figure 5.16 shows the depth of a tracer versus time (a), the trajectory within the model domain (b), and the descent velocity (c) representative for case 5.10, 511, and 5.12. As indicated by the tracer trajectory (b) slab geometry is less effected by the increase in lower mantle viscosity than for Rayleigh number 10^6-cases (cf. Figure 5.9). Only a small decrease in dip angle with increase in upper to lower mantle viscosity ratio has been found (Figure 5.16 b). However, the tracer trajectories represent the first 40 Myr of subduction. The evolution of the temperature field show that, later on, the dip angle of the subducting slab decreases. The amount of decrease increases with increasing η_{lo}/η_{up} (Figure 5.13-5.15). Figure 5.16 c shows that descent velocity decreases with increasing factor η_{lo}/η_{up}.

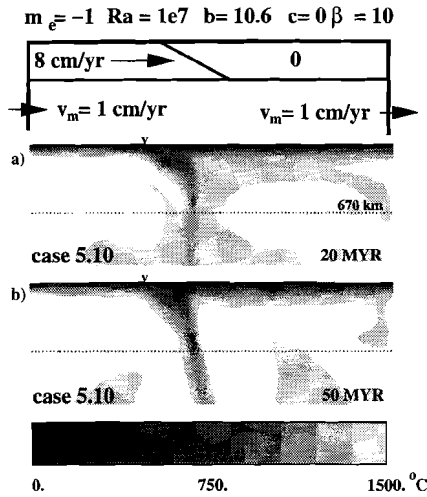$m_e = -1$ Ra = 1e7   b= 10.6   c= 0 β = 10

Figure 5.13 *Evolution of the temperature field and sketch of plate velocities of case 5.10. Rayleigh number is 10^7. Effective trench migration rate is -1 cm/yr. Surface viscosity is 200 time η_0. Viscosity increases at 670 km depth by a factor of 10.*
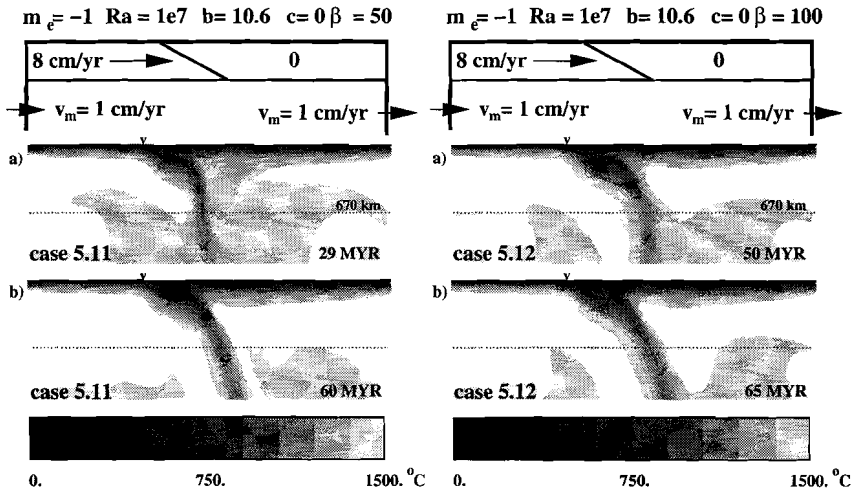
$m_e = -1$ Ra = 1e7   b= 10.6   c= 0 β = 50 $m_e = -1$ Ra = 1e7   b= 10.6   c= 0 β = 100

Figure 5.14   **Figure 5.15**

left: As Figure 5.13 for case 5.11. Viscosity increases at the upper lower mantle boundary by a factor of 50.
right: As Figure 5.13 for case 5.12. Viscosity increases at 670 km depth by a factor of 100.
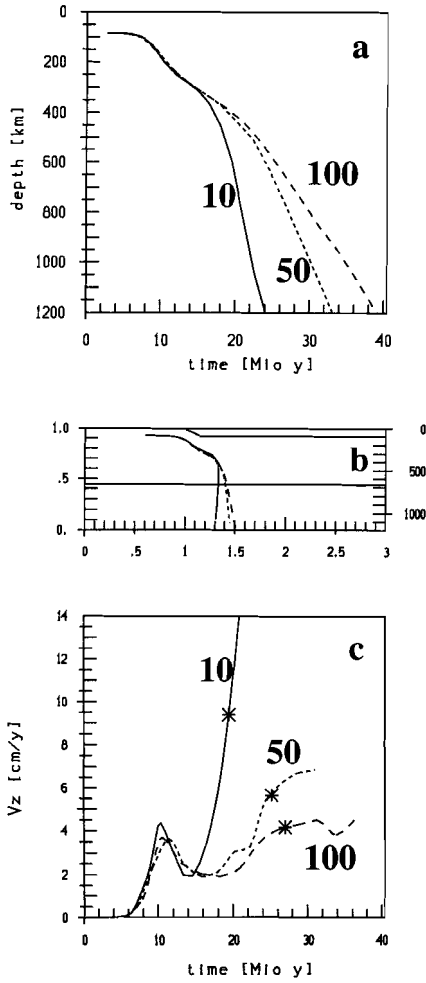
Figure 5.16 *Same as Figure 5.9 for case 5.10 ($\eta_{lo}/\eta_{up} = 10$), case 5.11 ($\eta_{lo}/\eta_{up} = 50$), and case 5.12 ($\eta_{lo}/\eta_{up} = 100$). Rayleigh number of these cases is 10^7.*

Effect of increase in viscosity with depth with $m_e = -2$ cm/yr, $Ra = 10^7$ - Case 5.13-5.15

Figure 5.2 d shows that the high viscosity slab (surface viscosity is 200 time η_0) penetrates into the lower mantle of 10-fold viscosity (case 5.13), of continuously increasing viscosity (case 5.14), and of 100-fold viscosity (case 5.15). The temperature field of both case 5.13 and 5.14 (Figure 5.17 and 5.18, respectively) show that the subduction process is strongly time-dependent. First, the slab penetrates into the lower mantle (Figure 5.17 a, 5.18 a). Second, the dip angle of the slab decreases in the upper mantle (Figure 5.17 b, 5.18 b). Third, the slab is stretched and thinned while cold material is piled near the trench (Figure 5.17 c, 5.18 c). This accumulated material descends quickly by an 'avalanche event' (Figure 5.17 d, 5.18 d). As the viscosity increases continuously with depth the overall Rayleigh number is decreased. Broader temperature anomaly structure is one consequence.

Another effect is the smaller descent velocity. An increase in viscosity at 670 km depth by a factor of 100 (case 5.15) stabilizes the slab structure - in terms of slab geometry through time. The initial deep mantle penetration is steep. The dip angle decreases with time to about 60° (Figure 5.19).
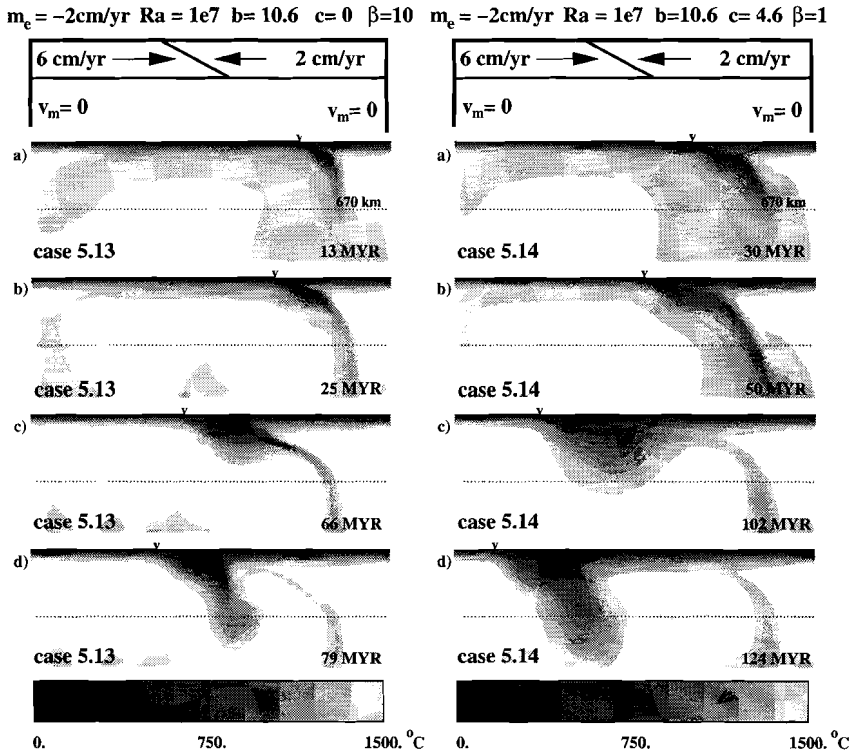

Figure 5.17   **Figure 5.18**

left: Evolution of the temperature field and sketch of plate velocities of case 5.13. Surface viscosity is 200 times η_0, increase in viscosity is 10-fold at 670 km depth. Rayleigh number is 10^7. Effective trench migration rate is -2 cm/yr. For viscosity profile see Figure 5.2 d.

right: As Figure 5.17 for case 5.14, where viscosity increases with depth continuously. At 670 km depth viscosity is about 10 times η_0. (Figure 5.2 d).

$m_e = -2cm/yr$ Ra = 1e7 b=10.6 c= 0 β=100
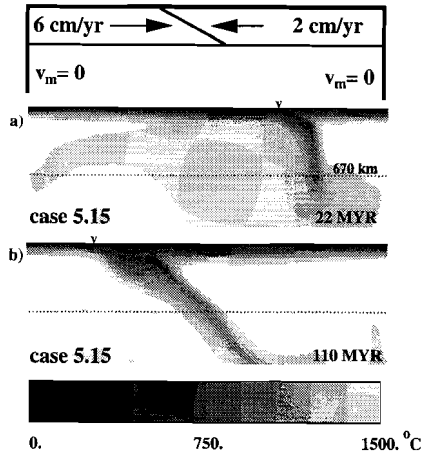

case 5.15

Figure 5.19 *As Figure 5.17 for case 5.15, where viscosity increases at 670 km depth by a factor of 100. (Figure 5.2 d).*

5.3.2   Discussion

High viscosity slabs tend to sink later into the lower mantle and (slightly) tend to decrease the ability of lower mantle penetration than those of a smaller viscosity contrast between slab and ambient mantle material. The increase in intensity of temperature-dependence of viscosity shows the same results on slab behaviour whether trench migration (-1 cm/yr) is present or absent - as has been studied in chapter 4. This is consistent with earlier results from *Zhong and Gurnis (1995)*. In their numerical model the plate margin (trench) changed in response to the mantle flow and the subducting plate encounters a phase boundary. However, results from *Zhong and Gurnis (1994)* and *Christensen (1996)* indicate that highly viscous slabs penetrate a phase boundary more easily. In the model of *Zhong and Gurnis (1994)*, however, dip angles were restricted to be perpendicular, since downwellings occurred only at the sidewalls.

While in the cases of chapter 4 the amplitude of increase in viscosity at the upper lower mantle interface did not make a difference whether the slab could penetrate through it or not, the viscosity contrast has a significant effect when trench migration is included. In chapter 4 it has been showed that, under consideration of a a stationary trench, an increase in viscosity at 670 km depth does not change slab geometry significantly. Once the slab has penetrated through the discontinuity, the dip angle becomes about 90°. However, when trench migration is present, an increase in lower to upper mantle viscosity ratio decreases the dip angle of the subducting slab, and therewith the ability of lower mantle penetration. The trench migration (to the left) or the background mantle flow (to the right)

increases the resistance, which the slab experiences on its back side (left), against the mantle flow. The dip angle of the slab decreases if this resistance is high enough. Additionally, with increasing viscosity jump at the upper-lower mantle boundary the descent of the slab becomes slower. Hence, the slab experiences that force for a longer time period until it encounters the bottom. As a result of an increase in visccosity with depth the dip angle of the slab is decreased. With a viscosity increase by a factor of 50 the descending slab cannot even penetrate through the 670 km discontinuity when the trench migrates with -2 cm/yr and $Ra = 10^6$. At least until the trench has reached the left vertical boundary the slab could not penetrate the lower mantle entirely. An isoviscous mantle, however, leads to a strongly time-dependent penetration style (such as in Figure 5.10, case 5.7). Phases change between penetration and thinned and stretched temperature structures mainly located in the upper part of the mantle. The viscosity increase by a factor of 50 stabilizes the slab structure (Figure 5.12, case 5.9). In case 5.8, where viscosity increases exponentially with depth, the slab is also hindered from penetrating the lower mantle. In average the mantle viscosity of case 5.8 is higher than in case 5.7 and 5.9. With a value of nearly η_0 in the upper mantle and a viscosity increase to the bottom to a value which is 100 times that of η_0 (Figure 5.2 c) the local Rayleigh number is smaller than in cases 5.7 and 5.9. The effective higher Rayleigh number in the lower mantle of case 5.7 ($\eta_{lo}/\eta_{up} = 1$) could be the reason for the strongly time-dependent behaviour. This explanation is supported by the results of the higher Rayleigh number models ($Ra = 10^7$), which showed a time-dependent penetration style at a higher trench migration rate (-2 cm/yr) combined with small increase in viscosity in the lower mantle. Decreasing dip angle with increase in η_{lo}/η_{up} was also found at Rayleigh number of 10^7.

As a general result we find, that with increasing rate of trench migration the dip angle of the slab and the ability of lower mantle penetration decreases. Effective trench migration is evoked by movement of the plate margin or by including a background mantle flow. Comparable cases (case 5.2 and 5.5) show similar temperature structure but they are not identical. The velocities at the boundaries relative to each other are the same (i.e. add 1 cm/yr to v_u, v_o, and v_m of case 5.2 and you get v_u, v_o, and v_m of case 5.5). But for a time-dependent dynamical system that does not mean, that relative velocities of the entire field are the same.

Since, here, the major aspect was to investigate the effect of rheology under consideration of trench migration, the influence of trench roll back itself will be studied in the next paragraph in more detail. Therefore the following experiments will be performed with only one viscosity profile. The surface viscosity will be 200 times the reference viscosity. Viscosity at the Earth's surface may be three to four orders higher than upper mantle viscosity (e.g. *Bills et al., 1994*) but because of numerical problems, caused by high viscosity contrasts across small distances

within the thermal boundary layer, in the following, surface viscosity is taken to be 200 times η_0. (Case 5.3, which has a higher increase in viscosity across the lithosphere, had to be restarted several times to overcome this problem.) Our results have showed that an increase in surface viscosity from 200 η_0 to 1000 η_0 has not such a dominating effect on the subducting slab as, for example, a change in trench migration rate. This allows us to use in the following models the relatively low surface viscosity of 200 times η_0, when comparing it to observed estimates. Our model results (including trench migration) provided already a broad variety in subduction zone geometry at a viscosity increase at 670 km depth by a factor of 50. Since this value is an average value for lower to upper mantle viscosity ratio (according to e.g. *Davies and Richards (1992)*, it has been chosen to be used in the following models. Furthermore, the effect of a different viscosity ratio can then be estimated on the base of the previous models.

5.4 Detailed study of the effect of trench migration on subduction

Whereas the influence of the viscosity in combination with trench migration was the subject of the previous section (5.3), here, a detailed study about the effect of the trench migration on the subduction process is presented. Therefore only one viscosity profile will be used: Based on the previous results both of chapter 4 and 5 surface viscosity is taken to be 200 times the reference viscosity η_0 and viscosity increases at 670 km depth by a factor of 50. Such a viscosity profile is given in Figure 5.2 a for e.g. case 5.2.

5.4.1 Results

Table 5.2 gives an overview over the model runs which will be dicussed in the following. The first four cases have been already treated in the previous sections. Case 4.10 is an experiment from chapter 4 without trench migration, which has here the function as a reference case due to the effect of trench migration. Cases 5.2, 5.5, and 5.9 have been considered in chapter 5.3.1, but for the detailed study of the effect of trench migration on subduction zones they are incorporated in the series of models discussed in this paragraph. $v_m = 1/0$ (see Table 5.2) indicates that the background mantle flow as imposed at the vertical boundaries decreases from 1 cm/yr to zero at 670 km depth. The decrease in mantle flow with depth may be implied from an increase in viscosity. The chosen range of trench migration - between -1 and -4 cm/yr - is consistent with observed values (see chapter 2.5.1) The convergence velocity $(v_u - v_o)$ is 8 cm/yr throughout the experiments.

Table 5.2 *Summary of Models*

case	v_u (cm/yr)	v_o (cm/yr)	v_m (cm/yr)	m_e (cm/yr)	Ra
4.10	8	0	0	0	
5.2	7	-1	0	-1	10^6
5.5	8	0	1	-1	
5.9	6	-2	0	-2	
5.16	7	-1	1	-2	
5.17	7	-1	1/0	-2	
5.18	5	-3	1	-4	
5.19	5	-3	1/0	-4	
5.20	7	-1	0	-1	
5.21	7	-1	1	-2	10^7
5.22	5	-3	1	-4	
5.23	5	-3	1/0	-4	

Reference model, Case 4.10
Figure 4.16 (chapter 4) shows two timesteps of the 'reference model' with zero trench migration and no background mantle flow. Hence m_e =0. The diagram above the temperature fields gives the plate velocities and the mantle flow at the vertical boundaries. The increase in viscosity by a factor of 50 at 670 km depth does not hinder the slab from penetrating into the lower mantle. The slab enters the lower mantle nearly vertically. The upper mantle structure established 108 Myr after subduction has started (Figure 4.16 b) is stable and does not change significantly with time. Of course, before reaching that stable stage, the penetration depth of the descending slab depends on time.

Case 5.2 and 5.5, $m_e = -1cm/yr$
These two cases have been discussed already in chapter 5.3.1. For completenes, the results obtained are repeated here. Both cases have an effective trench migration rate of - 1cm/yr. Velocities are 7, -1, and 0 (case 5.2, Figure 5.4) and 8, 0, and 1 cm/yr (case 5.5, Figure 5.7) for the underthrusting and overriding plate, and the background mantle flow, respectively. We found that the descent of the slab of case 5.2 (Figure 5.3) looks very similar - but not identical - to the temperature structure of case 5.5 (Figure 5.6). Figures 5.3 and Figure 5.6 show clearly a decrease in slab dip compared to case 4.10 (Figure 4.16) caused by trench migration. Similarity of these cases indicate that the decisive parameter is m_e rather than the absolute plate velocities v_u and v_o.

Case 5.9, 5.16, 5.17: $m_e = -2 \, cm/yr$:
Increasing the magnitude of the trench migration rate to 2 cm/yr (case 5.9 and 5.16)

decreases the dip angle to such an extent that the subducting slab is prevented from penetrating through the 670 km discontinuity (Figure 5.12 and 5.20). These cases with different plate velocities but the same m_e show again similar temperature structures. However, assuming that the high viscosity in the lower mantle causes a decrease in horizontal velocity with depth, we tested this effect in case 5.17 with a simple decrease in v_m at the vertical boundaries from 1 cm/yr above 670 km depth to zero below 670 km (see diagram above temperature fields of Figure 5.21). Then, trench migration of -2 cm/yr relative to the upper mantle flow is not able to preclude the slab from penetrating the lower mantle (Figure 5.21).
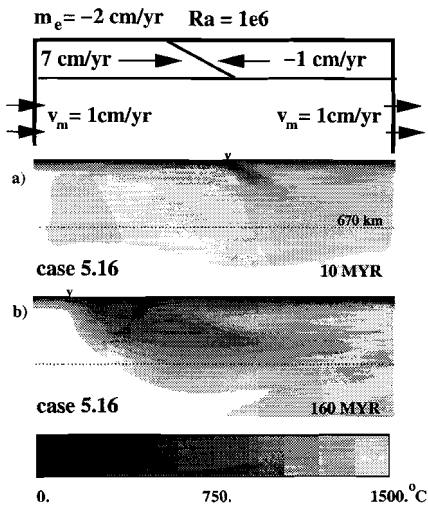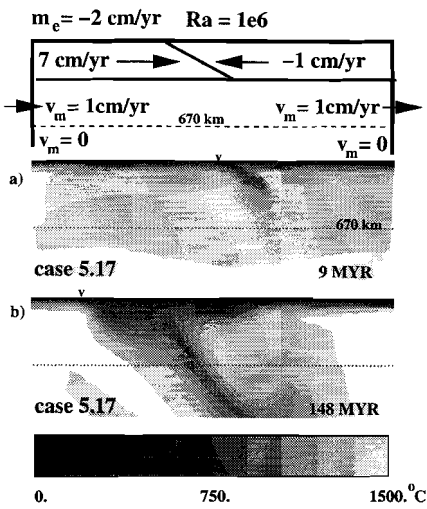
Figure 5.20   **Figure 5.21**

left: Evolution of the temperature field and sketch of plate velocities of case 5.16. Surface viscosity is 200 times η_0, viscosity increases at 670 km depth by a factor of 50. Rayleigh number is 10^6. Effective trench migration rate is -2 cm/yr.
right: As Figure 5.20 for case 5.17. The background mantle flow decreases at 670 km depth from 1 cm/yr to zero.

Case 5.18 and 5.19: $m_e = -4$ cm/yr:
Cases 5.18 and 5.19 have both an effective trench migration rate of -4 cm/yr. The absolute plate velocities for subducting and overriding plate are 5 and -3 cm/yr, respectively. As indicated in the top panel of Figure 5.22 the background mantle flow of case 5.18 is imposed to be 1 cm/yr down to 1200 km, whereas it decreases at 670 km depth from 1 cm/yr to zero in case 5.19 (Figure 5.23). The evolution of the temperature field shown in Figure 5.22 and 5.23 for case 5.18 and 5.19, respectively, indicate that the trench migration rate of $m_e = -4$ cm/yr is high enough to prevent

the slab from penetrating the lower mantle. The descending slab is trapped above
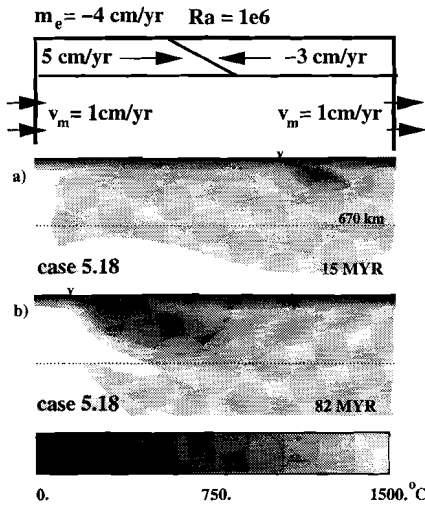the 670 km discontinuity for both types of mantle flow.
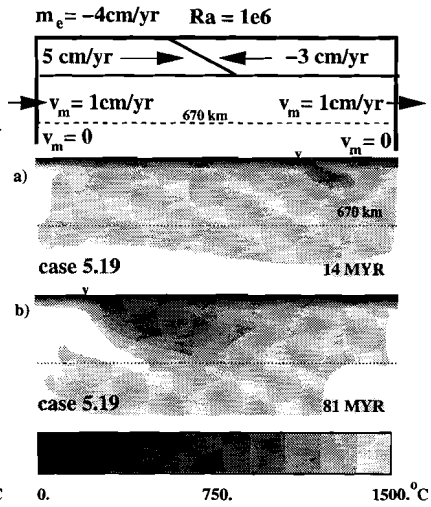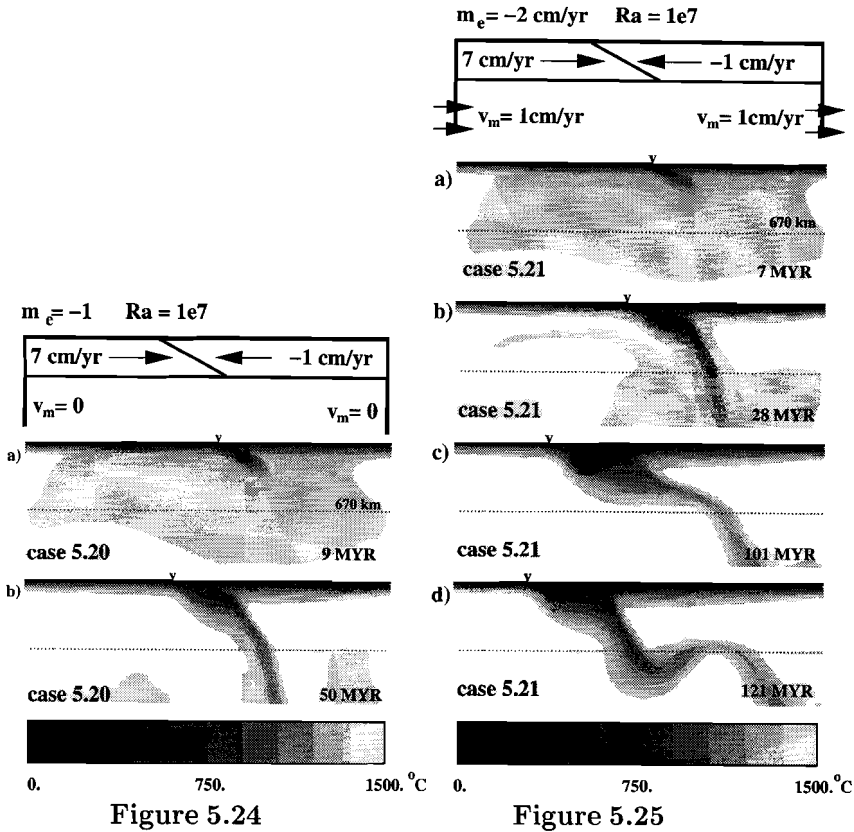

Figure 5.22   **Figure 5.23**

*left: Evolution of the temperature field of case 5.18. Effective trench migration rate
is -4 cm/yr.*

*right: Temperature field of case 5.19. Effective trench migration rate is -4 cm/yr.
The background mantle flow decreases at 670 km depth from 1 cm/yr to zero.*

Case 5.20-5.23 : Ra = 10⁷:

In these four cases the Rayleigh number is increased to 10^7, which can be inter-
preted as the decrease of reference viscosity by one order of magnitude. Figure
5.24 illustrates the evolution of the temperature anomaly caused by the subducting
slab moving with 7 cm/yr towards the overriding plate which has a velocity of -1
cm/yr. No background mantle flow is included, thus the trench migrates with -1
cm/yr. The dip angle of the slab is steeper than the corresponding low Rayleigh
number case 5.2 (Figure 5.4), the temperature anomaly is more as half as thick,
and slab descent is faster. Apart from case 5.20, where trench migration rate is -1
cm/yr, the higher Rayleigh number models show time-dependent characteristics
which are clearly different from most of the lower Rayleigh number models. (Case
5.7 with $Ra = 10^6$ shows strongly time-dependent characteristics.) In Figure 5.25
the development of case 5.21, with trench migration rate of -2 cm/yr, can be seen.
In the first phase (Figure 5.25a,b) the slab descends with a dip angle of about
45° to the 670-discontinuity and penetrates through it. In a second phase (Figure
5.25c) the dip angle is flattened in the upper mantle by trench migration. The

Figure 5.24   **Figure 5.25**

left: Evolution of the temperature field of case 5.20. Effective trench migration rate is -1 cm/yr. Rayleigh number is 10^7.
right: Temperature field of case 5.21. Effective trench migration rate is -2 cm/yr.

slab is stretched and thinned until it is nearly detached. After detachment a new instability develops, which leads to penetration into the lower mantle with a steep dip angle (Figure 5.25d). We observe the change in the dip angle (Figure 5.25c,d) three times. It is interesting to see that this 'avalanche effect' occurs even at the high trench migration rate of -4 cm/yr as in case 5.22 (Figure 5.26). Also a decrease of background flow to $v_m = 0$ in the lower mantle (case 5.23, Figure 5.27) does not change that time-dependent evolution in flow pattern. Comparable instabilities have been observed at high trench migration rates by *Griffiths et al. (1995)*. The time-dependence of the subduction process at higher Rayleigh number makes it more difficult to describe a straight forward relationship between slab behaviour and trench migration. However, the influence of the trench migration rate on the
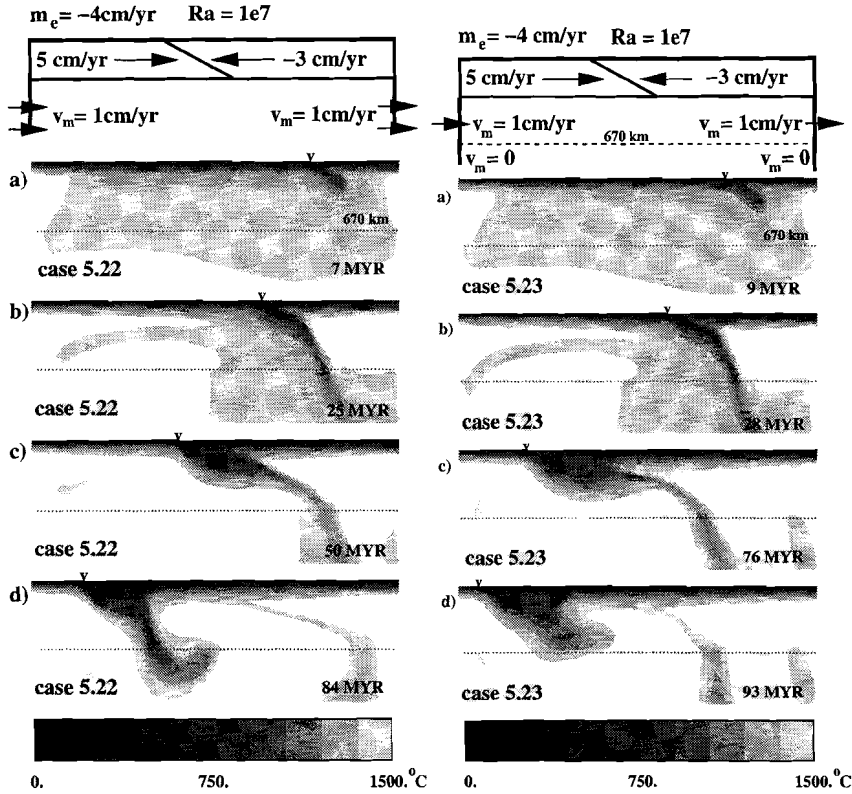
Figure 5.26   Figure 5.27

left: Evolution of the temperature field of case 5.22. Effective trench migration rate is -4 cm/yr. Rayleigh number is 10^7.
right: Temperature field of case 5.23. Effective trench migration rate is -4 cm/yr. The background mantle flow decreases at 670 km depth from 1 cm/yr to zero.

descent of the slab can be evaluated by contrasting case 5.20 where $m_e = -1$ cm/yr (Figure 5.24), with a stabilized slab structure penetrating the lower mantle to cases 5.21-5.22-5.23 ($|m_e| > 1$ cm/yr) which have phases in which the temperature anomaly shows a flattened structure above the 670-discontinuity (such as in Figure 5.25c).

Seismic velocity anomaly
Figure 5.28 and 5.29 show the seismic velocity anomaly corresponding with cases 5.21 and 5.23, respectively, by conversion from the model temperature as described

in section 3.3. The corresponding temperature fields are shown in Figures 5.25 b-d and 5.27 b-d. Within the upper 200 km the maximum amplitudes are with values up to 7 % slightly higher than observed magnitudes. In the lower mantle amplitudes are up to 2 %. The three different stages of the slab (straight penetration, flattening, and detachment accompanied with the repeated descent of accumulated cold material) are clearly to see. Especially the detached part in the lower mantle produces a positive seismic P-wave velocity anomaly.
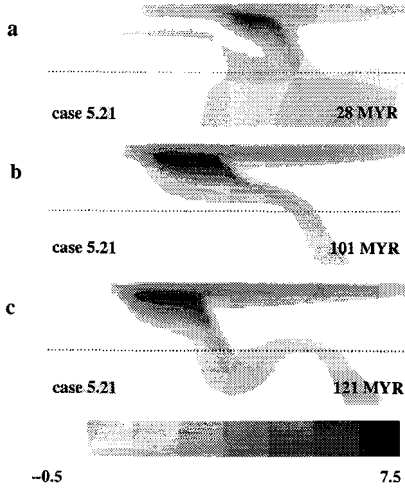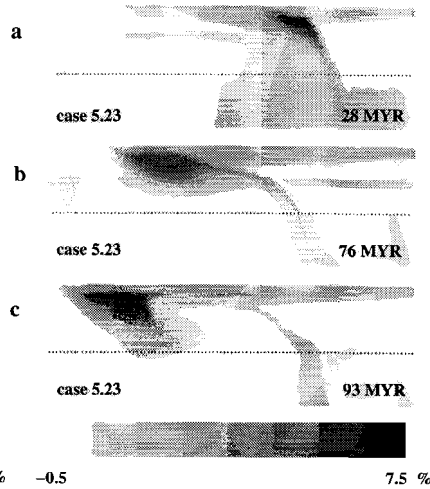
Figure 5.28   Figure 5.29

left: Seismic P-wave velocity anomaly of the model temperature illustrated in Figure 5.25 b-d.
right: Seismic P-wave velocity anomaly of the model temperature illustrated in Figure 5.27 b-d.

5.4.2   Discussion

Our numerical simulations indicate that trench migration at a rate of observed values affects the subduction process significantly. With increasing rate of trench migration, dip angle of the subducting slab and the ability of deep mantle penetration decreases. The correlation between slab dip and trench migration is in good agreement with numerical experiments done by *Christensen (1996)*, where slabs encountered a phase boundary, as well as with laboratory experiments done by *Griffiths et al. (1995)*, *Guillou-Frottier et al. (1995)*, and - earlier by *Kincaid and Olson (1987)*. In the latter study trench migration rates where not prescribed, but

resulted from the style of penetration of the descending slab. From their results *Kincaid and Olson (1987)* concluded that the dynamics of the sinking slab near the transition zone could control the geometry at convergent plate boundaries. Our approach is the other way round: we conclude that small differences in trench migration rates can affect the overall slab behaviour.
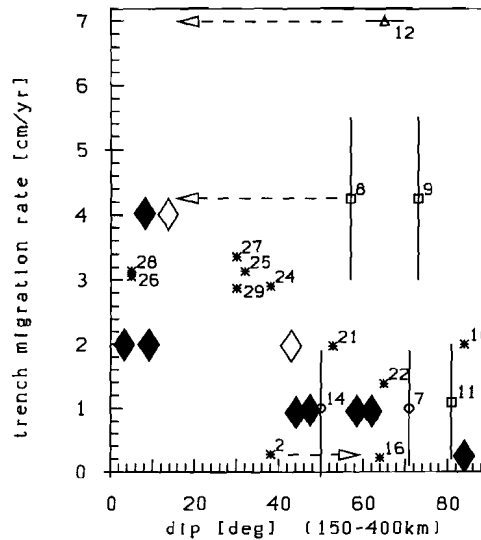

Figure 5.30 *Same as Figure 2.4, but additionally model results are included. Diamonds represent our model results. Dip angles are considered at ca 400 km depth from slabs which have been subducted for ca. 100 Myr. Black diamonds indicate models 4.10, 5.2, 5.5, 5.9, 5.11 (Ra = 10^7), 5.16, 5.18, and 5.20 (Ra = 10^7); white diamonds represent case 5.17 and 5.19, which include a decrease of the background mantle flow from 1 cm/yr to zero at the upper-lower mantle boundary.*

Figure 5.30 summarizes the relationship between trench roll-back and dip angle for 17 subduction zones as earlier displayed in Figure 2.4 (section 2.5.1). Additionaly, here, the model results are included. Diamonds represent our model results. Dip angles are considered at ca 400 km depth from slabs which have been subducted for ca. 100 Myr. Black diamonds indicate case 4.10, 5.2, 5.5, 5.9, 5.11, 5.16, 5.18 and 5.20, white diamonds represent cases 5.17 and 5.19, which include a decrease of the background mantle flow from 1 cm/yr to zero at the upper-lower mantle boundary. High Rayleigh number cases with time-dependent variation in dip angle have not been included in Figure 5.30. Our results are consistent with the relationship between dip angle and trench migration rate of observed subduction zones. Taking into account that individual subduction zones are affected by other parameters such as slab age (*Vlaar and Wortel, 1976; Wortel and Vlaar, 1988*) or a complex trench system (e.g *Widiyantoro and Van der Hilst, 1996*), it is striking

that the results obtained from the simplified two-dimensional model calculations agree quite well with observed values. Moreover, our models do not include back-arc extension. Strictly taken, our results do not apply to subduction zones where spreading in the back-arc region occurs. This, however, is not considered to be a major limitation of the modelling, since it is unlikely that back-arc extension affects slab behaviour in the deeper part of the upper mantle, in which we are most interested.

Results of whole mantle convection models including phase transitions indicate that propensity to layered convection increases with increasing Rayleigh number (*Zhao et al., 1992; Yuen et al., 1994*). In our study, model runs of Ra = 10^7 show a quasi-periodical penetration of the slab through the 670 discontinuity even at high rates of trench migration. The corresponding lower Rayleigh number cases display descending lithosphere trapped above 670 km depth. Thus, in our experiments lower Rayleigh number cases tend to lead to layered convection which is consistent with results from *Christensen (1996)*.

Similar structures as provided by the strongly time-dependent models have been found by tomographic imaging. Seismic velocity anomalies indicate that beneath the Tonga arc the Pacific plate descends into the mantle at an angle of about 50°, becomes subhorizontal in the transition zone, and penetrates several hundred kilometers further west into the lower mantle (*Van der Hilst, 1995*). Those subducting slabs with strongly time-dependent behaviour, which are in a phase when the slab is flattened within the upper mantle, show also this characteristic structure (such as in Figure 5.25 c).

5.5   East and west dipping subduction zones

As shown in the previous section the backgound mantle flow plays an important role, more specifically through its relative velocity with respect to the plates and the trench. According to *Ricard et al. (1991)* the lithosphere rotates with a global westward drift with a relative velocity of about 1 cm/yr within the so-called hotspot reference frame. Hence, they propose a global eastward mantle flow beneath the plates. *Doglioni et al. (1991)* and *Ricard et al. (1991)* assume that this relative motion causes a difference in dip angle of subducting slabs between west and east dipping subduction zones: West dipping subduction zones (e.g. Apennines, Carpathians) are characterized by high dip of the subducting slab, small elevation of the chain and a deep foreland basin. East dipping subduction zones (e.g. Western Alps, Dinarides) have minor dip angle, greater elavation, and a shallow foredeep basin (*Doglioni, 1990; Doglioni et al., 1991*).

In the models studied in the previous sections, the direction of the under-thrusting plate and that of the background mantle flow, if included, were the

same. If we assume that this background mantle flow corresponds to an east-
ward mantle flow as proposed by *Doglioni (1990)*, then, implicitly, our subduction
models (which include a mantle flow) are eastward dipping. When analysing the
relationship between plate velocities/trench migration and slab dip, the difference
between east and west dipping lithosphere must be considered. Here, we want to
present a few results upon that topic.

5.5.1   Results

In the following numerical experiments, the global westward drift of the lithosphere
as inferred by *Ricard et al. (1991)* is implemented as an eastward flow of the
underlying upper mantle. Two groups of experiments have been carried out. First,
we consider a situation with a fixed overriding plate with absolute zero velocity. An
eastward mantle flow is opposite to the (horizontal) direction of the underthrusting
plate. Hence, the slab dip is westward. And second, models with different dip
direction (east, west) but with the same effective trench migration rate will be
compared.

Table 5.3 summarizes the models discussed in the following. E and W indicate
east- and westward dip of the descending slab. Only the models with a west
dipping slab are new. The other cases are taken from the previous two sections (5.3
and 5.4), but listed here for a better classifying of the new models. The viscosity
profile is equal to that chosen in chapter 5.4: Surface viscosity is 200 times the
reference viscosity and viscosity increases at 670 km depth by a factor of 50. The
model geometry is shown in Figure 5.1.

Table 5.3 *Summary of Models*

case	v_u (cm/yr)	v_o (cm/yr)	v_m (cm/yr)	m_e (cm/yr)	Ra	Dip
5.5	8	0	1	-1	10^6	E
5.24	8	0	-1	+1	10^6	W
5.11	8	0	1	-1	10^7	E
5.25	8	0	-1	+1	10^7	W
5.16	7	-1	1	-2	10^6	E
5.9	6	-2	0	-2	10^6	-
5.26	5	-3	-1	-2	10^6	W

For the westward dipping subduction zones the - eastward - background
mantle flow has been imposed to flow in opposite direction than the horizontal

motion of the underthrusting plate. (Thus opposite to the arrows indicating v_m in Figure 5.1.) According to our sign convention v_m is negative in westdipping subduction zones.

(i) West dipping subduction zone
Figure 5.31 a and b shows the temperature structure of the west dipping slab (i.e. direction of underthrusting is westward) of case 5.24 with Rayleigh number of 10^6 and of case 5.25, with Rayleigh number of 10^7, respectively. Since the overriding plate is fixed in terms of the absolute reference frame, trench migration relative to the mantle flow is positive (i.e. not retreating). In both of the cases 5.24 and 5.25 the slab is strongly bent by the mantle flow. Note that such a slab structure has not been found and is just artificial. Models with the same absolute plate velocities but opposite mantle flow can be seen in Figure 5.7 (case 5.5) and Figure 5.14 (case 5.11). Dip angles of case 5.24 and 5.5 and of case 5.25 and 5.11 are comparable, but mirror-imaged.
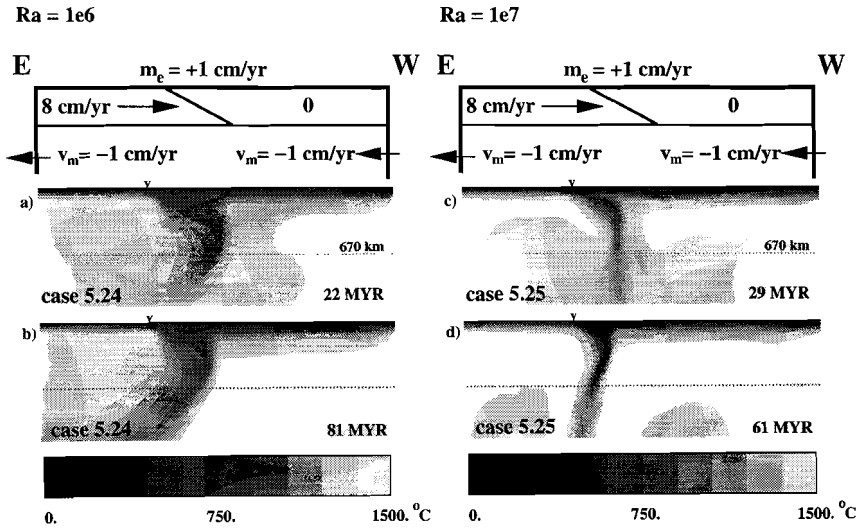
Figure 5.31 *West dipping subduction zones. Since the overriding plate/trench is fixed in the absolute reference frame (e.g. hotspot frame) the effective trench migration rate is +1 cm/yr relative to the eastward mantle flow. Both slab structures of case 5.24 (Ra = 10^6) on the left and of case 5.26 (Ra = 10^7) on the right are not realistic, i.e. not observed.*

(ii) Comparison between east, 'neutral', and west dip at same m_e
Figure 5.32 shows an east dipping subduction zone (case 5.16), a 'neutral' ($v_m = 0$) subduction zone (case 5.9), and a westdipping zone (case 5.26). Cases 5.9 and 5.16

have already been shown in the previous two sections. For a better comparison they are displayed here again. Relative velocities $v_u - v_m$ and $v_o - v_m$ are kept constant to be 6 cm/yr and -2 cm/yr, respectively. Note, that the latter is equal to the effective trench migration rate m_e. It can be seen that the mantle flow effects the slab geometry. The dip angle of the west dipping slab is higher than the east dipping slab. The dip angle of the 'neutral' case (case 5.9) with $v_m = 0$ fits good between them.
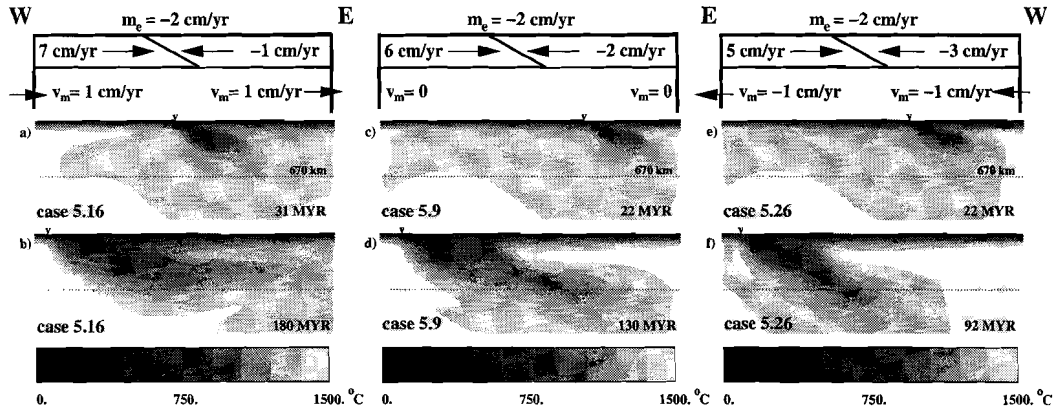
Figure 5.32 *Three models with same effective trench migration rate of -2 cm/yr, but different direction of the subducting slab relative to the eastward mantle flow. **E** and **W** indicate east and west, respectively. left: east dipping subducting slab; middle: 'neutral' dip in terms of zero mantle mantle flow; right: west dipping subduction zone. Dip angle increases from left to right.*

5.5.2   Discussion

Our model results have shown that east and west dipping subduction zones in presence of an eastward mantle flow differ in slab geometry. The eastward background mantle flow of 1 cm/yr flattens the structure of an east dipping slab, whereas it increases the dip angle of a west dipping slab. Slab structures revealed from cases with forward migrating trench (same direction as underthrusting plate) show dip angles greater than 90 degrees, which is an unrealistic feature. In our models the trench system is not allowed to react on the dynamics of the slab (cf. *Kincaid and Olson, 1987; Zhong and Gurnis, 1995*). This restriction could explain the artificial slab structures.

The second group of models showed that in spite of the same trench migration rate of -2cm/yr, the west dipping slab had penetrated the mantle with a dip angle of about 20 degrees higher than the eastward dipping slab. This is in good agreement with the proposed difference in slab structure of east and west dipping subduction zones (*Ricard et al., 1991; Doglioni et al., 1991*). A similar experiment had been done with a smaller trench migration rate of -1cm/yr (not shown). Only a slight difference in dip angle was found.
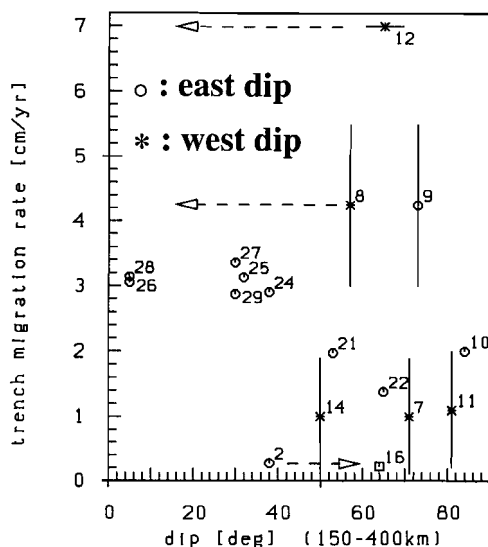
Figure 5.33 *Relationship between dip angle of subducting slabs and trench migration rate as already established in chapter 2 (Figure 2.4). Subduction zones have been divided into east dipping (circles) and west dipping (asterisks) subduction zones. Numbers indicate location of subduction zones as given in Table 2.1 (Chapter 2.4). The Central Aleutians subduction zone (# 16) is directed northward and therefore marked by a square.*

Eastward mantle flow reduces and increases the effective trench migration rate of west and east dipping subduction zones, respectively. In the relationship between observed trench migration and dip angle as established in Chapter 2.5.1 (Figure 2.4) the effect of the mantle flow is not considered. The hypothesis proposed by *Doglioni et al. (1991)* predicts that at similar trench migration rate west dipping slabs should have higher dip angles than eastward subducting slabs. Thus, if there was a general effect on slab geometry, west dipping subduction zones should have a higher trench migration rate to yield a similar dip angle as east dipping subduction zones. I.e. at similar trench migration rate west dipping slabs should have higher dip angles than eastward subducting slabs. Figure 5.33

shows that such a relationship was **not** found. Similar to Figure 2.4 dip angles
are related to the (absolute) trench migration rate. Subduction zones have been
devided into those which are east dipping (indicated by circles) and those whose
dip is towards the west (indicated by asterisks). The Central Aleutians subduction
zone (# 16 in Figure 5.33) is directed northward and therefore marked by a square.
A possible explanation for the independence of the globally observed dip angles
on the direction of dip (E, W) could be that in three dimensions (real Earth) the
mantle flow can turn aside below and beside the subducting slab. This would
reduce the resistence of the descending slab towards the opposing mantle flow.
Once the slab had reached the bottom within our two-dimensional model there is
at least no possibility for the mantle flow to surround the slab at the sides. For
example, in case 5.25 the slab penetrates the deep mantle vertically until the slab
has reached the bottom (Figure 5.31 c). After the tip of the slab had disappeared
'through the bottom' the dip angle increases (Figure 5.31 d).

Probably the local geometry as the lateral width along the strike of a sub-
duction zone might be decisive for the effect of the mantle flow on subduction
zone geometry. Only three-dimensional modelling could provide insight into this
subject.

5.6   Summary

This section concerns all results of the previous sections (5.3-5.5). We summarized
the modes of slab structure in a regime diagram given in Figure 5.34 for Rayleigh
number 10^6 and in Figure 5.35 for Rayleigh number 10^7. The horizontal axis
denotes the viscosity jump at the upper-lower mantle boundary (β or η_{lo}/η_{up}),
at the vertical axis the effective trench migration rate is given. A few more
experiments than have been discussed in chapter 5.3 and 5.5 have been performed
to complete the diagram for clearness. In all model runs represented in this
diagram temperature dependence of the viscosity is given by $c = 10.6$ (i.e. surface
viscosity is 200 times η_0). Symbol 1 and 2 (in Figure 5.34 and 5.35) indicate that
slab penetrates the lower mantle with a dip angle greater and smaller than 60°,
respectively. Symbol 3 represents that the slab is prevented from deep mantle
penetration, and symbol 4 stands for strongly time-dependent behaviour of the
slab with change in slab dip accompanied by an avalanche effect.

The experiments with Rayleigh number of 10^6 (Figure 5.34) delineate three
different modes of slab geometry: (i) nearly horizontal temperature anomaly struc-
ture above the 670 km discontinuity (symbol 3); (ii) strongly time-dependendent
slab behaviour where slabs are detached and thinned followed by a flushing event
(symbol 4); and (iii) penetrating slabs with a quite stable dip angle (symbol 1 and
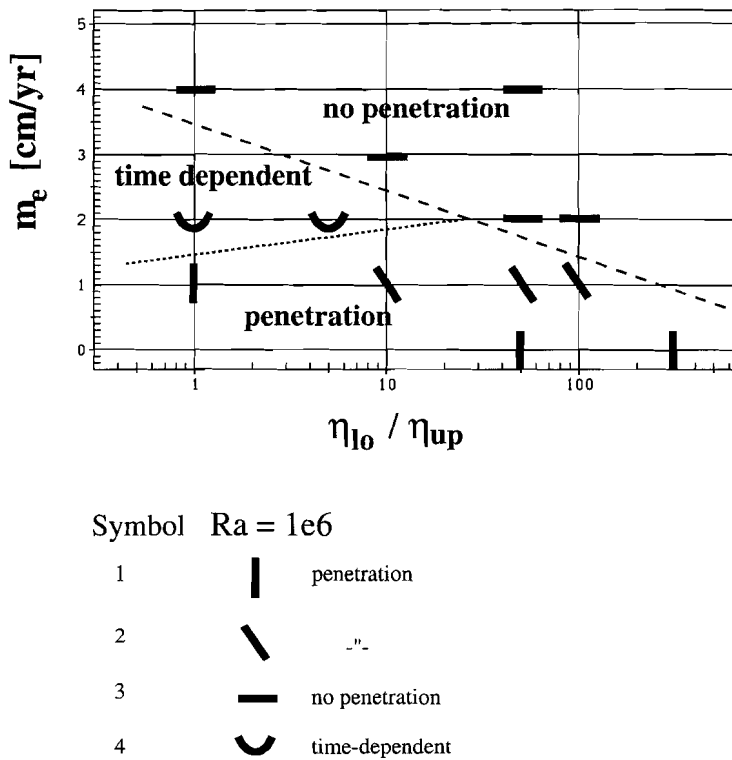2). The dashed line clearly divides the models into two areas: one without any

Figure 5.34 *Diagram of different penetration styles observed in viscosity layered experiments. The vertical and horizontal axis give the effective rate of trench migration and the ratio between lower and upper mantle viscosity, respectively. Symbol 1 and 2 indicate penetration through the 670 km discontinuity, with a dip angle greater or smaller than 60°, respectively. Cases represented by symbol 3 are charactarized by a slab accumulated nearly horizontally in - or above - the transition zone. Symbol 4 stands for the strongly time-dependent slab behaviour, where dip angle varies dynamically with time. The dashed line divides the penetrative from the non-penetrative style. The dotted line delineates the time-dependent mode from the stable penetration mode.*

(upper right area) and the other with penetration (lower left area). The dotted line within the area of penetration could be the border between those models with strongly time-dependent slab behaviour and those with a stabilized slab structure. For ratios of lower to upper mantle viscosity up to about 20 the time-dependent mode with varying dip angle is the transition from straight penetration at small trench migration rates to the non-penetrative style at high migration rates. A probable reason for the strongly time-dependent slab behaviour could be the local Rayleigh number, which is higher the smaller the (lower mantle) viscosity

is. An increase in viscosity jump at 670 km stabilizes the slab structure. The diagram in Figure 5.34 indicates the effect of the increase of the viscosity ratio at the upper-lower mantle boundary: Without trench migration slabs penetrate the lower mantle at viscosity ratios up to 300 with a dip angle of about 90°. At trench migration of 1 cm/yr, with increasing upper to lower mantle viscosity ratio the dip angle becomes slightly more concave towards the overriding plate, which decreases the ability of deep mantle penetration. At a higher trench migration rate of 2 cm/yr the increase of the viscosity jump leads to a change from the strongly time-dependent mode (partly penetration) to the non-penetrative style. Thus, in summary, as long as trench migration takes place, the ability of deep mantle penetration of the descending slab decreases along the x-axis to the right (i.e. increase of the viscosity ratio η_{lo}/η_{up}). In turn this can be expressed as: With increasing trench migration rate (m_e) smaller viscosity increase (η_{lo}/η_{up}) is sufficient to prevent slab penetration.
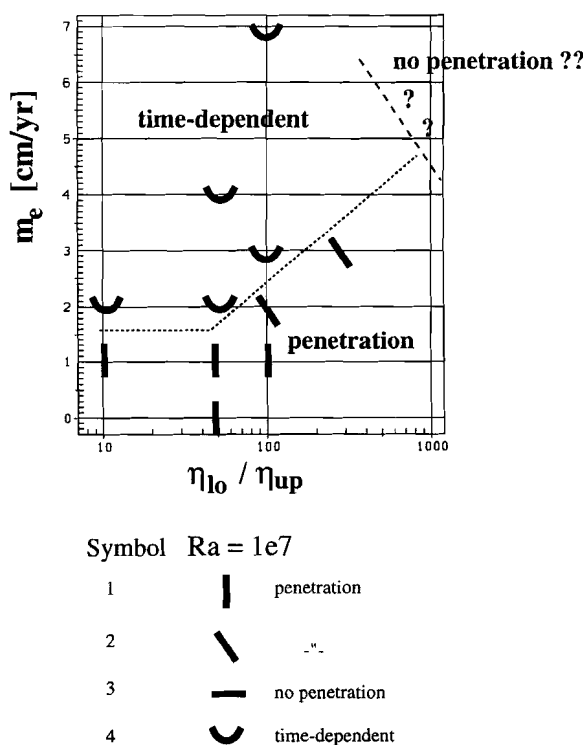

Figure 5.35 *As Figure 5.34 but for cases of Rayleigh number of* 10^7. *The question marks indicate that the transition from the time-dependent dominated regime to the non-penetrative regime is uncertain. The dashed line is a suggestion for this change.*

Within the 'window' given by the range in viscosity increase by a factor between 10 and 100, and by the trench migration rate between 1 and 3 cm/yr, which are ranges realistically for the Earth, every of the three modes can exist.

For the higher Rayleigh number cases of 10^7 (see Figure 5.35) the modes of

slab geometry are shifted to the right (i.e. higher viscosity increase) and to the top (i.e. higher trench migration rates). The very high trench migration rate of 7 cm/yr could not prevent the slab from entering the lower layer where viscosity is 100 times larger than in the upper layer. Strongly time-dependent behaviour is dominant for $Ra = 10^7$ (left of the dotted line). This is consistent with the result that time-dependent type of subduction occurred at Rayleigh number 10^6 only at small values of lower mantle viscosity which is associated with higher local Rayleigh numbers. An assumption is made where the dashed line, adequate to the dashed line of Figure 5.34 dividing the area into the regime with and without penetration, could be. We did not performe more experiments to investigate this precisely, because both the ranges of the axis would be much too high for values applicable to the Earth. Probably resistance to slab penetration into the lower mantle due to an increase in density and a phase transition at 670 km depth would result in a shift of the regime areas toward the left and the bottom.

A model with $Ra = 10^6$ is more sensitive to variations in trench migration rate and the depth-dependent viscosity. This could explain the great variety observed with e.g. seismic tomography. On the other hand, descent velocity of slabs is in general too slow at $Ra = 10^6$. Vertical slab velocity of $Ra = 10^7$-cases agree better with observed values. Therefore, the strongly time-dependent type of subduction dominates at reasonable values for trench migration and viscosity increase with depth. This supports the result from chapter 4 that, for our model set up, 10^6 and 10^7 yield a lower and upper limit for the Rayleigh number, respectively.

5.7   Conclusions

In the present chapter we first have studied the effect of the slab stiffness and the ratio of upper to lower mantle viscosity in combination with trench migration rate. Second, the influence of trench migration (without further variation in viscosity) has been investigated in detail. Third, east and west dipping subduction zones were studied.

The stiffness of the slab decreases the ability of the downgoing slab to enter the lower high viscosity layer. However, a slight difference in slab geometry could be observed between the cases where surface viscosity was 1000 and 200 times the reference viscosity, respectively, due to the great difference in temperature dependence of the viscosity. From that we conclude that our modelling with relatively low surface viscosity (*Bills et al., 1994*), which is only two orders higher than the upper mantle viscosity, still can provide useful results. In combination with trench migration it has been found that the increase in upper to lower mantle viscosity ratio decreases the ability of the slab to penetrate through the 670 km discontinuity.

The model calculations showed clearly that with increasing rate of trench migration, in the range of observed rates, dip angles and the ability of slab penetration into the lower mantle tend to decrease. Even without any viscosity interface at 670 km depth a trench migration rate of 4 cm/yr was sufficient to prevent the descending slab from penetrating the deep mantle. The results concerning the effect of trench migration are in good agreement with the tectonic setting and slab geometry in several subduction zones. In our models we could observe a strong sensitivity of slab structure to even small trench migration rates (1 cm/yr). We find that, when the horizontal background mantle velocity decreases (discontinuously) with depth, higher rates are needed to prevent slab penetration.

The strongly time-dependent cases show the possibility of an 'avalanche' event of a descending cold instability as has also been detected in global mantle convection models with symmetrical downwellings (*Tackley et al., 1993; Steinbach and Yuen, 1994*). That means, that depending on the elapsed time since subduction has started, the subducted slab may be in a stage with slab material mainly accumulated above the 670 km discontinuity, or it may be in a phase (shortly after the flushing event) where penetration through the discontinuity would be observed. Thus, we conclude that the intrinsic time-dependence and the particular tectonic setting of subduction zones can provide a great variety of subduction related seismic anomalies. Finally, the conversion from our model temperature distribution to seismic P-wave velocities shows good agreement with the shape of observed seismic anomalies. However, magnitudes of converted seismic velocity anomalies are in general a few % too high, particularly in the upper 200 km of the subducted slab where values up to 7% are obtained.

Ricard et al. (1991) and *Doglioni et al. (1991)* proposed that an overall westward drift of lithosphere causes a difference in dip angle of subducting slabs between west and east dipping subduction zones. In principle, this is supported by our model results. However, a detailed analysis of 17 subduction zones could not confirm the expected result, i.e. east dipping subducting slabs did not show in general smaller dip angles than those with westward dip - at similar trench migration rate. The discrepancy between hypothesis and observations casts doubt upon the existence of an overall eastward mantle flow. However, the predicted mantle flow by *Ricard et al. (1991)* is globally eastward, but may vary locally in both direction and magnitude. These regional differences could be a reason that a global relationship between dip direction of subduction zones (east, west) and the dip angle cannot be observed.

CHAPTER 6

Age-dependence of subduction

6.1 Introduction

At mid-ocean ridges new oceanic lithosphere is produced. Aging of the lithosphere is accompanied with cooling and densification due to thermal contraction. This process is expressed, for example, by a change in topography and heatflow. This implies that the age of the lithosphere at the time it starts to be subducted influences the subduction process. *Vlaar and Wortel (1976)* established the relationship between the age of subducted lithosphere and the maximum focal depth within that slab. Only subduction zones in which lithosphere older than 70-100 Myr is consumed exhibit deep-focus earthquakes, i.e. in the depth range of 500-700 km. At subduction zones consuming lithosphere younger than 70 Myr focal depths are not deeper than 300 km (*Vlaar and Wortel, 1976; Wortel, 1980; Wortel and Vlaar, 1988*). According to the hypothesis put forward by *Sung and Burns (1976)* these two distinct focal depth ranges could be explained by mineral physical processes (see also *Kirby et al., 1991; Kirby, 1995*). Old lithosphere is thicker and is assumed to sink faster than young lithosphere. It is expected that for both reasons old lithosphere is colder in the interior than young lithosphere. In that fast moving downgoing slab, the temperature at its cold center may remain below a characteristic temperature. The low temperature could depress the olivine-spinel phase transformation which would be distorted downwards. The phase change could then occur far from equilibrium, which might cause deep earthquakes of high energy release. As olivine within young and slowly descending slabs would cross the equilibrium boundary at about 400 km depth at higher temperatures, phase transformation occurs much closer to equilibrium, i.e. arround 400 km depth (*Rubie and Ross, 1994*). If a characteristic temperature exists below which phase transformation from olivine to spinel is depressed and above which the phase transition is allowed, it is assumed to be about 600-700 °C (*e.g. Rubie and Ross, 1994*).

Recent two-dimensional thermo-kinetic modelling showed that slow and warm slabs will not significantly influence the structure of the phase boundary between olivine and spinel (*Däßler et al., 1996*). However, their models predict the correlation between fast subducting slabs and concentration of deep-focus earthquakes at around 600 km depth due to transformation of metastable olivine at this depth

range. Descent velocity was imposed to be 3 cm/yr and 10 cm/yr for the slow and the fast slab, respectively.

The evolution of the temperature in subducting lithosphere seems to play a key role for the mineral physical processes in the descending slab. Therefore we applied our model in order to compare the development of young and old subducting slabs.

6.2   Model set up and results

As lithosphere becomes thicker with increasing age, we model young subducting slabs by taking the thermal plate thickness to be 55 km. This is consistent with an age of about 20-30 Myr (e.g. *Wortel and Vlaar, 1988*). Plate thickness of the models discussed in the previous chapters was taken to be 100 km which is consistent with ca. 100 Myr old slabs.
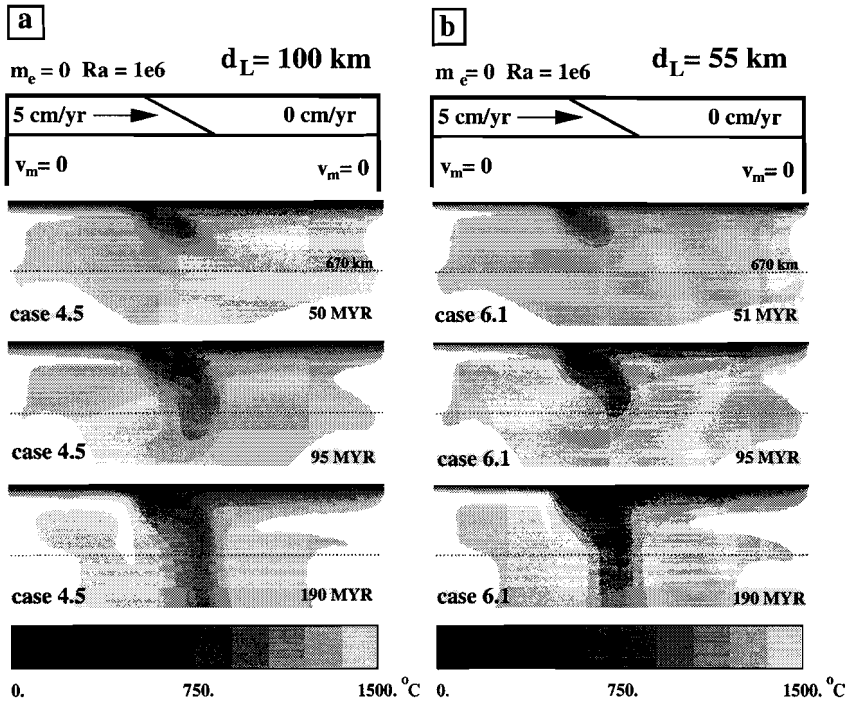
Figure 6.1 *Subduction of old 100 km thick lithosphere (a) and of young 55 km thick lithosphere (b). Slab geometry is rather similar. The interior of the old slab is colder.*

Table 6.1 *Summary of Models*

case	m_e (cm/yr)	Ra	d_L (km)
4.5	0	10^6	100
6.1	0	10^6	55
4.12	0	10^7	100
6.2	0	10^7	55
5.2	-1	10^6	100
6.3	-1	10^6	55
5.20	-1	10^7	100
6.4	-1	10^7	55

Boundary and initial conditions for the temperature have been chosen appropriately to the plate thickness of the subducting slab: The layer over which temperature increases from the 0°C surface temperature to mantle temperature is also 55 km thick (see chapter 4.2). Table 6.1 summarizes the models. Models have been performed with Rayleigh number of 10^6 and 10^7. Both a fixed trench and a trench migrating effectively with -1 cm/yr are considered. d_L is the thermal thickness of the lithosphere. Model 4.5 and 4.12 are taken from chapter 4, model 5.2 and 5.20 are taken from chapter 5.

Trench migration rate $m_e = 0$
Figure 6.1 shows the temperature field evoked by subduction of old lithosphere (case 4.5) and of young lithosphere (case 6.1). In both cases the underthrusting plate moves with 5 cm/yr towards the fixed overriding plate. %The temperature anomalies of the subducted slab differ in magnitude but only slightly in thickness. The dip angles of both of the slabs are similar. Within the old lithosphere (case 4.1) isotherms penetrate deeper into the mantle than within the young subducted slab (case 6.10). For comparison of the descent velocity representative tracer particles are studied. (For description see chapter 4.3.) Figure 6.2 shows the depth of a single tracer versus time (a), the trajectory of that tracer within the model domain (b), and its vertical velocity v_z versus time (c).

The starting position of each of the tracers is within the surface plate. The dashed and solid graph indicates the tracer trajectory of case 4.5 (100 km thick lithosphere) and of case 6.1 (55 km thick lithosphere), respectively. What is striking is that trajectories and descent velocities from both cases are very similar. For a detailed analysis of the temperature structure horizontal temperature profiles were considered.

Figure 6.3 shows the temperature profile at 400 km depth through the old and young slab. The top panels belong to the temperature fields at 95 Myr, the lower panels to the temperature fields at 190 Myr after subduction had started. Temperature difference of the minimum slab temperature between the young and
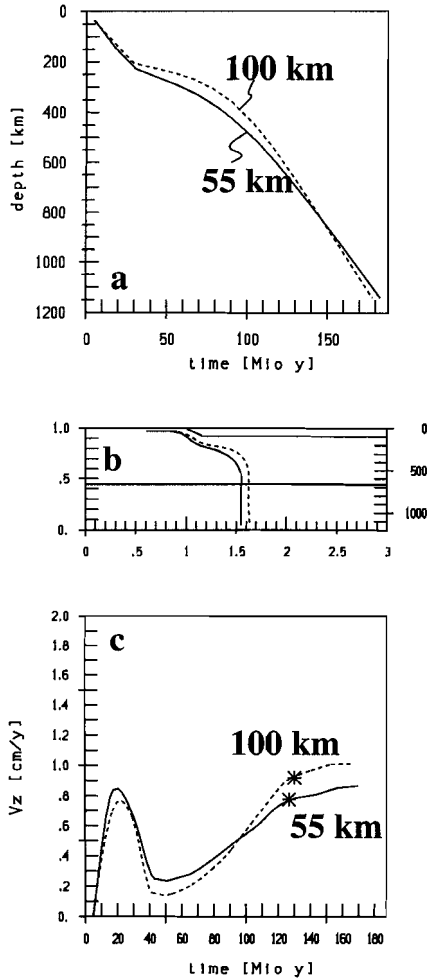
Ra = 1e6   m$_e$= 0

Figure 6.2 *Tracer trajectory versus time* *(a), the trajectory of that tracer within the model domain (b), and its vertical velocity v_z versus time (c). Solid graphs indicate the trajectory of the young lithosphere (case 6.1, $d_L = 55km$). Dashed lines represent the trajectory of the old lithopshere (case 4.5, $d_L = 100km$). In the model domain b the position of the rigid plate is given. Asterisks in c indicate the time when the tracer encounters the depth of 670 km.*

old lithosphere is about 140 °C at the 95 Myr stage, and ca. 70 °C at 190 Myr. Thus, the interior of the older lithosphere is colder after the same time of subduction than it is of the younger lithosphere.

In the next two cases Rayleigh number has increased to 10^7. Plate velocity of the underthrusting plate is here 8 cm/yr. Figure 6.4 shows the temperature fields of case 4.12 and case 6.2, representing an old and a young subducting lithosphere, respectively. Subduction zone geometry seems not to be affected by the thickness of the lithosphere. In Figure 6.5 tracer trajectories of each of the cases 4.12 and 6.2 are compared. The trajectories of the representative tracers are nearly along the same path (b). The descent velocity of the tracer of the old lithosphere (dashed) is slightly higher than that of the young slab (c). Sinking velocity is higher than
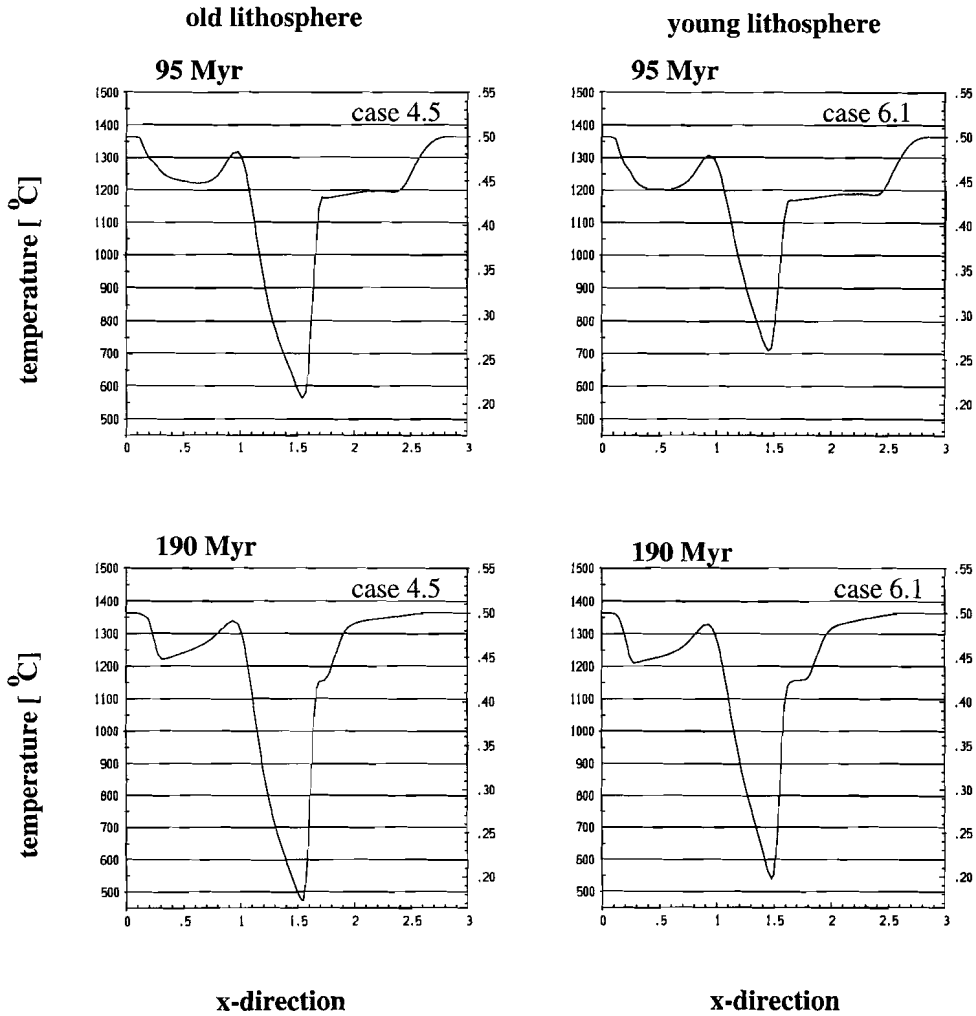
$$Ra = 1e6 \quad m_e = 0$$

Figure 6.3 *Horizontal temperature profile at 400 km depth. Left panels show the temperature for the old lithosphere (case 4.5), right panels show the temperature for the young lithosphere (case 6.1), top panels at 95 Myr, and lower panels at 190 Myr. The minimum temperature within the old lithosphere is colder than within the young lithosphere at the corresponding time.*

in the previous two cases with lower Rayleigh number. In Chapter 4 we showed that this is not only caused by the higher plate velocity, but mainly an effect of the higher Rayleigh number.
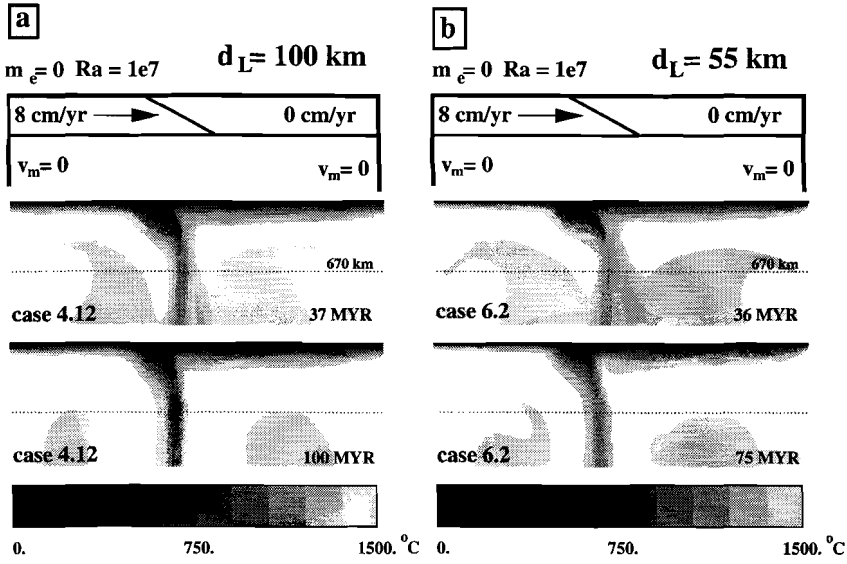
Figure 6.4 *As Figure 6.1 for case 4.12($d_L = 100$ km) and case 6.2 ($d_L = 55$ km).*
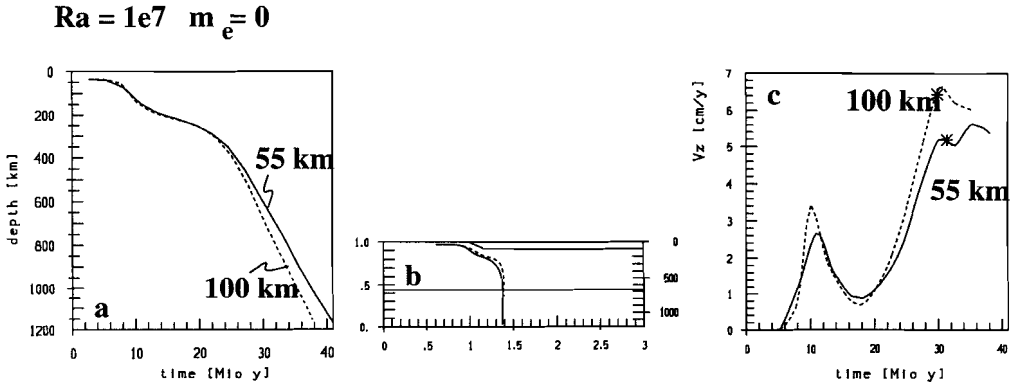
Figure 6.5 *As Figure 6.2 for case 4.12($d_L = 100$ km) and case 6.2 ($d_L = 55$ km).*

Horizontal temperature profiles at 400 km are shown in Figure 6.6. Left and right panels show the profiles for the old lithosphere and young lithosphere, respectively. At 37 Myr, when the tip of the old slab has passed through the depth of the model domain (Figure 6.4 top), the interior of the slab is about 500 °C. At the corresponding time the minimum temperature of the young slab is more

Ra = 1e7 m$_e$ = 0
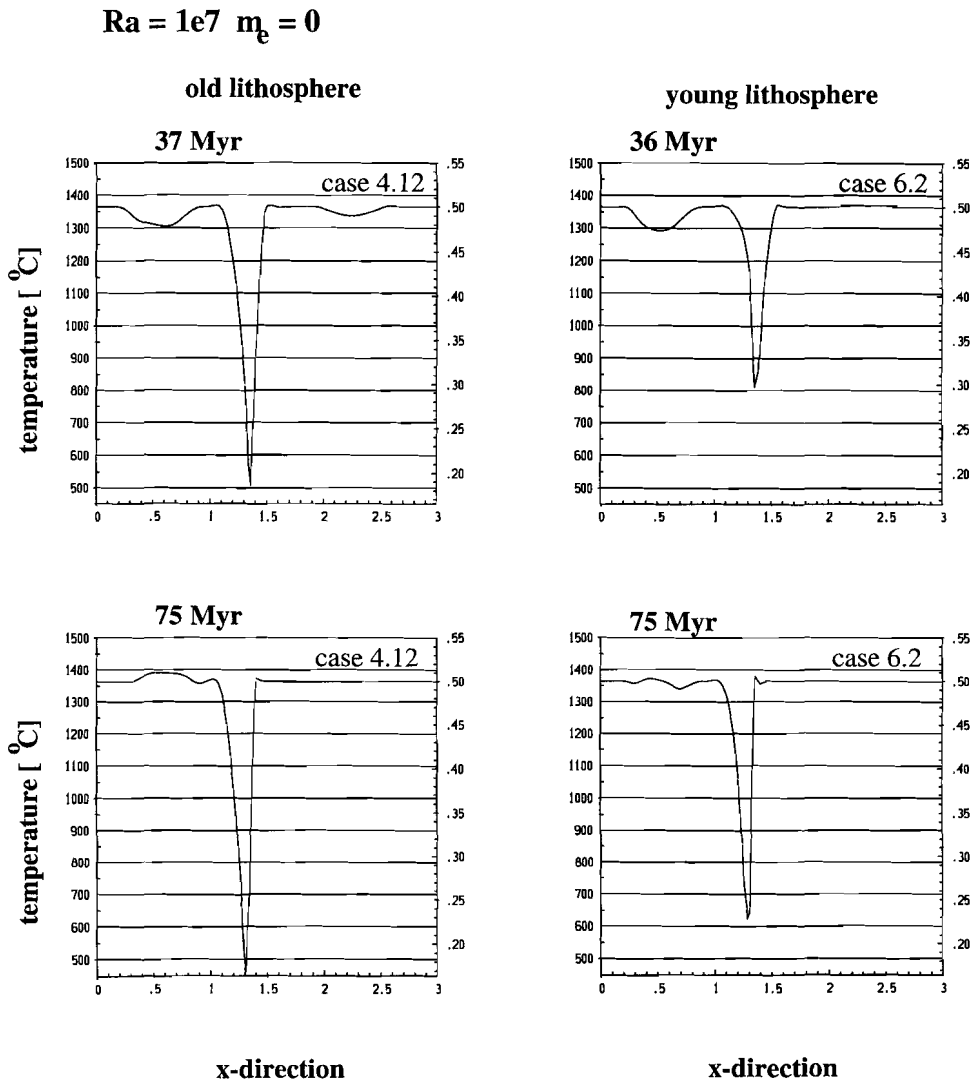
Figure 6.6 *As Figure 6.3 for case 4.12(d_L = 100 km) and case 6.2 (d_L = 55 km).*

than 800 °C. During further subduction more cold slab material is transported into the mantle and minimum temperature decreases within the slabs to about 450 °C whithin the old slab and to about 620 °C within the young slab. Further significant drop in temperature with time was not found.
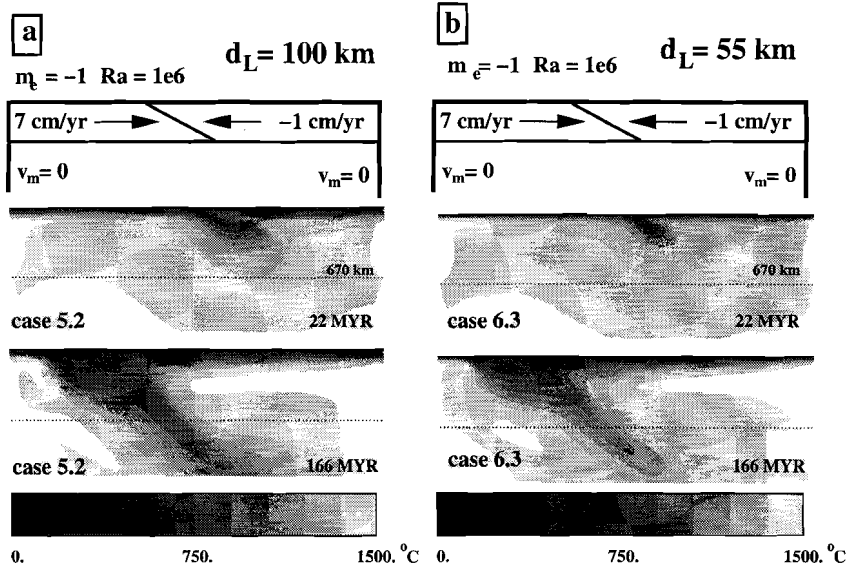
Figure 6.7 *As Figure 6.1 for case 5.2($d_L = 100$ km) and case 6.3 ($d_L = 55$ km).*

Trench migration rate $m_e = -1$ cm/yr
Within the next four experiments trench migrates effectively with -1cm/yr and the convergence velocity is 8 cm/yr. The evolution of the temperature field of case 5.2 with a 100 km thick lithosphere and of case 6.3 with a 55 km thick lithosphere is shown in Figure 6.7. Both cases have a Rayleigh number of 10^6. It can be seen that the slab interior of the old lithosphere is colder than of the young slab, but slab geometry looks again rather similar. By analysing the tracer trajectories (Figure 6.8) we found that the descent of the young lithosphere is even faster during the first 110 Myr of subduction. The temperature profiles at 400 km depth at 166 Myr show that minimum temperature of the old and young slab is about 480 °C and 620 °C, respectively (Figure 6.9).

In the following two models trench migration rate is also -1 cm/yr. Rayleigh number is increased to 10^7. The geometry of the temperature anomalies of the old (case5.20) and young (case 6.4) lithosphere shown in Figure 6.10 differ only slightly. Isotherms penetrate within the old lithosphere deeper into the mantle
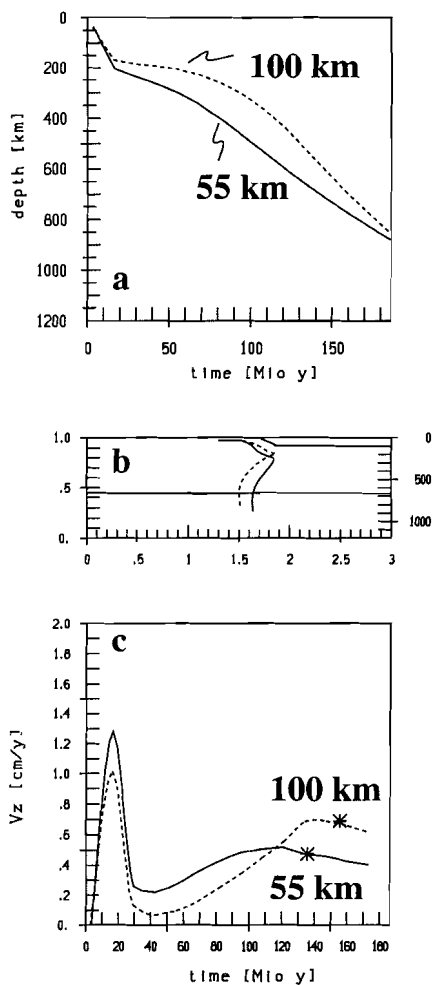
Ra = 1e6   m$_e$ = -1 cm/yr

Figure 6.8 *As Figure 6.2 for case 5.2 ($d_L = 100$ km) and case 6.3 ($d_L = 55$ km).*

than isotherms of the same value in the young slab do. However, the tracer trajectories indicate that descent velocities of both slabs are rather similar (Figure 6.11). The difference in temperature bewtween the old and young lithosphere can be seen in Figure 6.12, which shows the temperature profiles at 400 km depth. The minimum temperature of the old slab is at 50 Myr after subduction about 530 °C. At the same time the minimum temperature at 400 km depth is ca. 670 °C within the young slab.
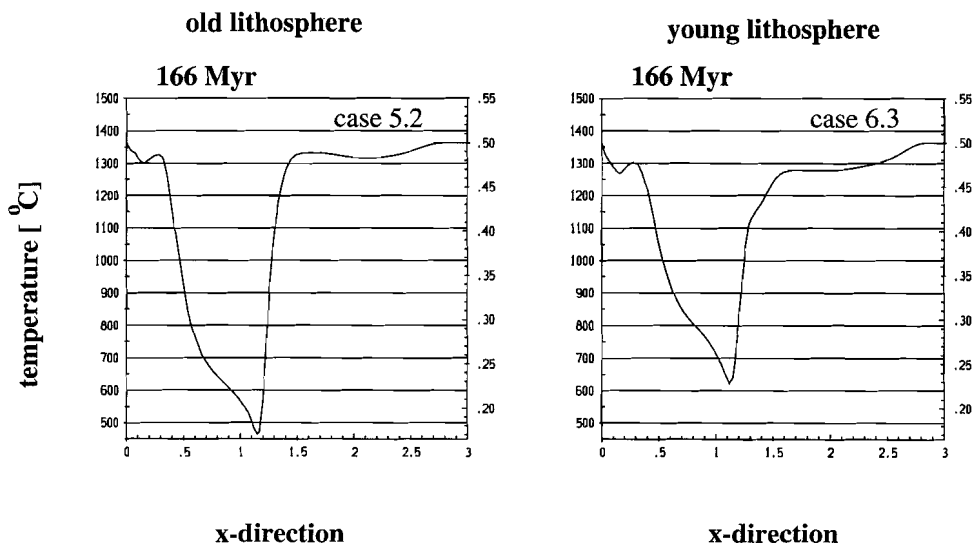
Ra = 1e6 m_e = -1 cm/yr

Figure 6.9 *As Figure 6.3 for case 5.2(d_L = 100 km) and case 6.3 (d_L = 55 km).*
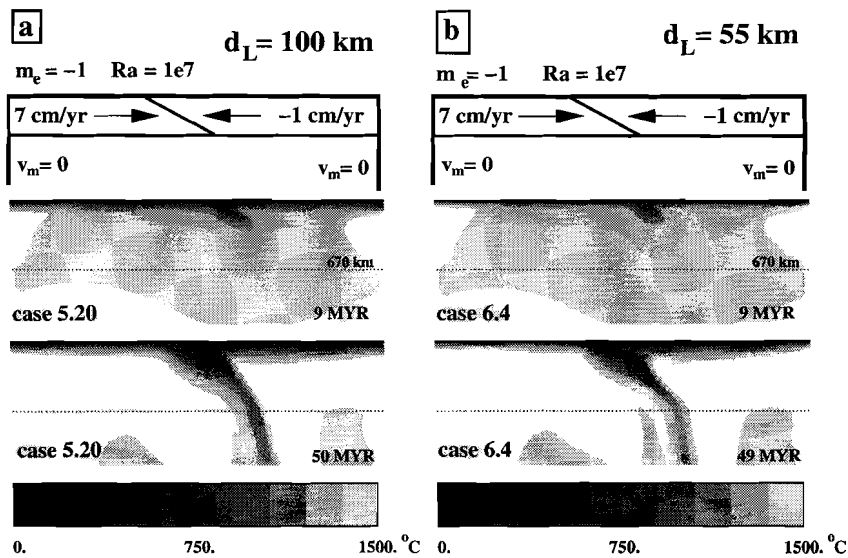
Figure 6.10 *As Figure 6.1 for case 5.20(d_L = 100 km) and case 6.4 (d_L = 55 km).*
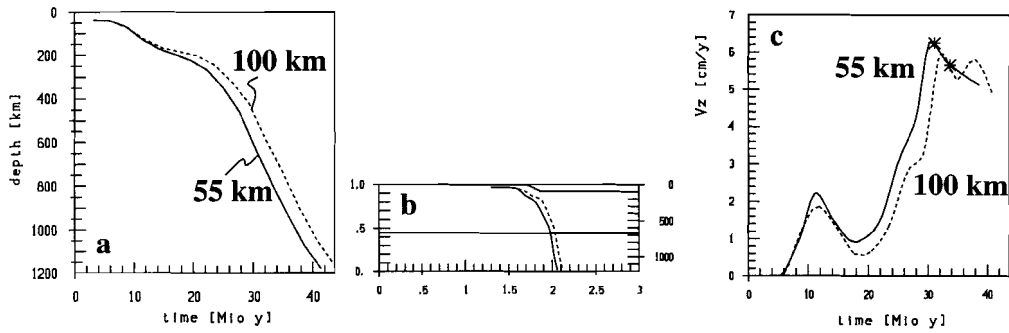
Ra = 1e7 m $_e$=-1 cm/yr

Figure 6.11 *As Figure 6.2 for case 5.20(d_L = 100 km) and case 6.4 (d_L = 55 km).*

Ra = 1e7 m$_e$ = -1 cm/yr

old lithosphere   **young lithosphere**

50 Myr   **49 Myr**
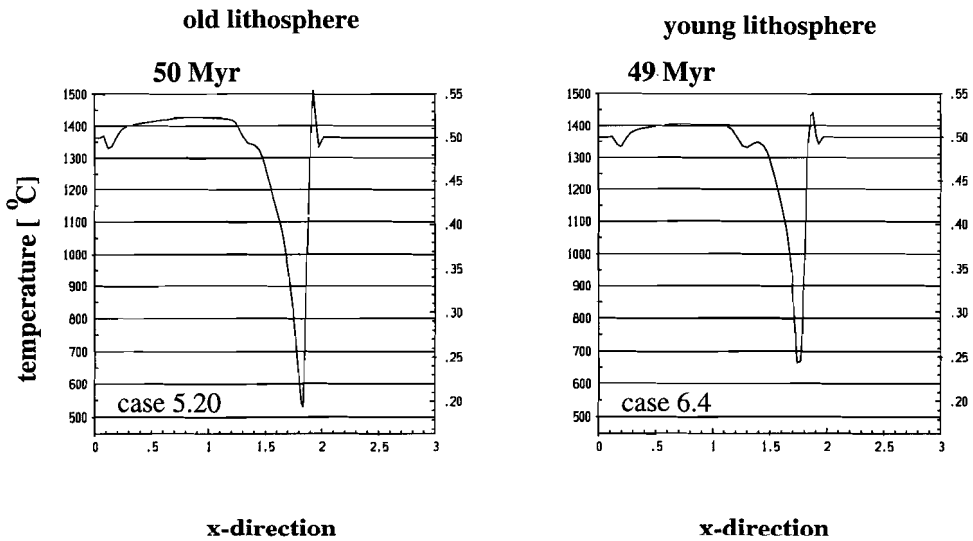

x-direction   **x-direction**

Figure 6.12 *As Figure 6.3 for case 5.20(d_L = 100 km) and case 6.4 (d_L = 55 km).*

6.3   Discussion

Our model results have shown that slab geometry seems not to be affected by the age/thickness of the lithosphere. The descent velocity and trajectories of representative tracer particles, which were included within the surface plate of young and old lithosphere at initiation of subduction, were also very similar. *Vlaar and Wortel (1976)* proposed that the penetration depth of subducted lithosphere increases with increasing age. Their result was based on the relationship between focal depth and age of the slab at the time it started to be subducted. Our results of the tracer trajectories, which represent material flow, seem to be contrary to that. The tracer trajectories indicated that descent velocity and path of the slabs are not affected by the age/thickness of the subducting plate. However, the penetration depth of the temperature isotherms is age-dependent. Horizontal temperature profiles at 400 km depth showed that the minimum temperature within the slab at that depth is higher in old than in young lithosphere. The temperature difference varies between 70 and 300 °C. By the time the tip of the slab had reached the depth of 1200 km the young subducted slabs (apart from case 6.1) had at 400 km depth a minimum temperature higher than 600 °C. The minimum temperature of old lithosphere was at the corresponding time and depth always lower than 600 °C. This is in good agreement with the relationship between focal mechanism and age of subducted slabs. It is assumed that, when olivine crosses the expected phase boundary at 400 km depth at temperatures higher than a characteristic temperature T_{ch}, phase transformation occurs at that depth. If a slab passes the theoretical phase boundary at lower temperatures than T_{ch}, which is expected to happen for old lithosphere, it might be possible that olivine is not transformed to spinel. The existence of metastable olivine could be responsible for deep earthquakes (e.g. *Kirby et al., 1991*). *Rubie and Ross (1994)* proposed that this characteristic temperature is about 700 °C. If such a critical temperature exists, our models support that it would be 600 ± 50°C.

Our model results indicate that there is no significant difference in subduction zone geometry and vertical velocity between subduction zones consuming young and old lithosphere. However, the vertical velocity could be affected by two features which we did not include in our models.

(i) Phase boundary distortion within the slab
Distortion of the phase boundary may affect the dynamics of the descending slab. On the one hand, it is assumed that the phase boundary at 400 km depth is elevated within a cold subducting slab relative to the ambient mantle, which causes a negative buoyancy force (e.g. *Turcotte and Schubert, 1971*). On the other hand, if the interior of an old slab remains that cold that within the inner slab the phase transformation is suppressed, the metastable olivine (at depth greater than 400 km) would be then less dense then the surrounding mantle material, which
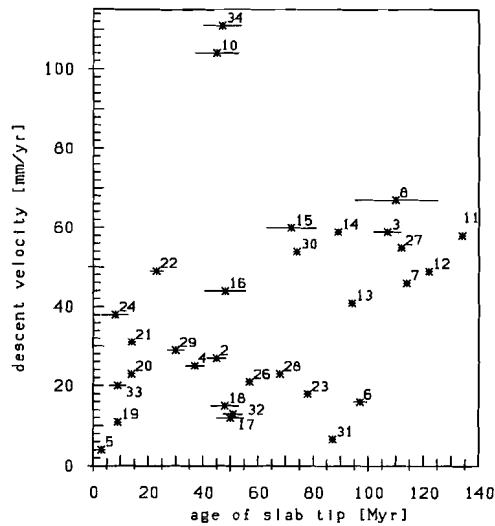
Figure 6.13 *Relationship between age of the tip of subducted slabs and their descent velocity. Datas are taken from Jarrard (1986). Descent velocity is obtained by dividing the vertical slab extent by the time since the tip of the slab had subducted (see Table 1 of Jarrard (1986)). The numbers up to 30 indicate subduction zones listed in Table 2.1 (chapter 2.4). # 31 - # 34 represent Makran, Andaman, North Sulawesi and New Britain subduction zone, respectively. Two exceptions are the Solomon (# 10) and New Britain (# 34) subduction zone. However, the overriding plate for the New Britain and Solomon trench is not known with certainty (Jarrard, 1986). Velocity rates and estimation for the age of these subducted slabs could then also be uncertain.*

already has been transformed to spinel. This would cause a positive buoyancy effect (*e.g. Kirby, 1995*). Both gravitational forces could be then compensated, but, in general, an uncertainty concerning the dynamic effect of the phase change remains.

(ii) Compositional structure of the lithosphere

Oceanic lithosphere consists of a crustal layer of about 7 km thickness, underlain by a 10-20 km thick layer of harzburgite, with a layer of depleted peridotite beneath (*Ringwood, 1994*). Both the crustal and the harzburgitic layer have a density deficit relative to the mantle material (*Irifune and Ringwood, 1993*). In young and thin lithosphere the thickness ratio between light (crust and harzburgite) and dense (peridotite) material is higher than in old and thick lithosphere. This could result in less gravitational force of young lithosphere. Consequently, if young lithosphere is forced to be subducted, horizontal layering ('lithospheric doubling') of an overriding upper lithosphere on top of the young subducted lithosphere, which is too stable to descend deep into the mantle, could be formed (*Vlaar, 1983*).

However, compositional buoyancy of the oceanic crust is likely to be removed after subduction by conversion to eclogite at a depth less than 100 km (*Oxburgh and Parmentier, 1977; Gubbins and Snieder, 1991; Irifune and Ringwood, 1993*). Once crustal material enters the lower mantle (670 km) it has again a density deficit and might be trapped at 670 km depth (*van Keken et al., 1996*). Numerical models showed that the compositional buoyancy effects due to the density deficit of harzburgite cannot overcome thermally induced negative buoyancy (*Gaherty and Hager, 1994*). These results indicate that the introduction of a compositional structured lithosphere probably would not affect our results significantly.

Figure 6.13 shows the relation between age of the tip of subducted slabs and their descent velocity. Datas are taken from *Jarrard (1986)*; see also *Wortel (1980)*. Descent velocity is obtained by dividing the vertical slab extent by the time since the tip of the slab had subducted (see Table 1 of *Jarrard (1986)*). Although a clear trend of increasing vertical velocity of the subducting slab with increasing age can be seen the data are widely spread. This implies that slabs which differ greatly in age could have similar descent velocity as occurred in our model runs. The numbers up to 30 indicate subduction zones listed in Table 2.1 (chapter 2.4). # 31 - # 34 represent Makran, Andaman, North Sulawesi and New Britain subduction zone, respectively. Two exceptions are the Solomon (# 10) and New Britain (# 34) subduction zone. However, the overriding plate for the New Britain and Solomon trench is not known with certainty (*Jarrard, 1986*). Velocity rates and estimation for the age of these subducted slabs could then also be uncertain.

6.4   Conclusions

From our model results we conclude that the minimum temperature in the interior of old/thick subducting slabs is lower than of young/thin subducting lithosphere. This implies that phase transformation from olivine to spinel could take place within young slabs near equilibrium at about 400 km depth, whereas the transformation could be suppressed within cold and old slabs. Metastable olivine possibly responsible for deep earthquakes of high energy release could be present. Thus our model results, combined with the *Sung and Burns (1976)* hypothesis concerning the role of metastable olivine in deep earthquake generation, are in agreement with the observed relationship between focal depth and age of subducted lithosphere. If a characteristic temperature exists below and above which phase transformation between olivine and spinel is suppressed and allowed to occur, respectively, our study indicates that this temperature could be $600 \pm 50°C$.

CHAPTER 7

Fossil subduction zones

7.1   Introduction

Upper mantle seismic velocity structure show positive velocity anomalies related to convergence zones which are no longer active. Beneath Spain, for example, reduced magnitudes of P-wave velocity anomalies relative to the active Aegean region are observed (*Blanco and Spakman, 1993*). For interpretations we need insight in the evolution of anomalies.

The issue of the present chapter is to investigate subduction processes formerly active at convergent plate margins. It is assumed that non-stationary aspects, such as thermal relaxation or tectonic processes, dominate when the subduction process ceases. Cessation of subduction can occur when thick buoyant continental crust enters the subduction zone (*Royden, 1993*). For example, the early Miocene history of the Carpathian thrust belt involved deepwater oceanic or thinned continental crust. When thicker crust of the European plate entered the trench system in middle Miocene time, the thrust belt became inactive and subduction ceased (*Royden, 1993*). Pliocene and Quaternary uplift of the Transylvanian basin and adjacent mountains are interpreted as the result of unloading as the subducted slab became detached from the overlying plate (*Royden et al, 1983*; see also *Wortel and Spakman, 1992*). Tomography results show high P-wave velocity anomalies beneath the East-European platform (*Spakman, 1990*). These high velocity structures may result from the proposed subducted slab below the Carpathians.

Evidence for former subduction beneath southern Spain has been given by tomographic imaging (*Spakman et al., 1993; Blanco and Spakman, 1993; de Jonge et al., 1994*). Figure 7.1 displays a cross section of the seismic structure beneath the Betic Alboran region/southern Spain. Tomography results are from *Spakman et al. (1993)*. Magnitudes are shown in percentage of the ambient mantle for P-waves given by the regional reference model. The high P-wave velocity structures (positive anomalies) below the Betic-Alboran region between 200 and 700 km depth can be interpreted as the image of former subducted, but now detached, lithosphere. Geodynamic consequences of slab detachment, including uplift, have been discussed by *Wortel and Spakman (1992)*. *Platt and Vissers (1989)* interpreted uplift in the early Miocene in the Betic region as the dynamic response of the crust-lithosphere system to convective removal of a cold
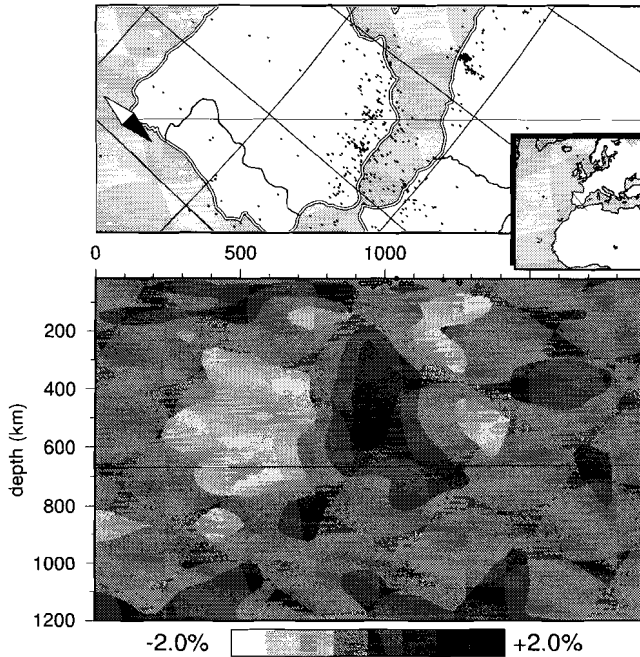
Figure 7.1 *Cross section of the mantle beneath the Betic Alboran region/S Spain as revealed by seismic imaging. Tomography results are from Spakman et al. (1993; EUR89B) Magnitudes are shown in percentage of the ambient mantle for P-waves given by the regional refference model. The high P-wave velocity structures (positive anomalies) below the Betic-Alboran region between 200 and 700 km depth can be interpreted as the image of former subducted lithosphere (Blanco and Spakman, 1993).*

lithospheric root. The dynamic consequences of the latter process, in particular uplift, are expected to be very similar to those of slab detachment.

The tomographic results are also consistent with earlier observations of deep seismic activity (at about 650 km depth) in this region, which is decoupled from the intermediate-depth activity and thus might correspond to the remnant of a former subduction zone *(Buforn et al., 1988)*. Combination of the tomographic and tectonic inferences suggest that subduction in the Alboran region took place during at least part of the Oligocene followed by detachment in the early Miocene *(Platt and Vissers, 1989; Blanco and Spakman, 1993)*.

With the following numerical calculations we want to study the processes

involved with cessation of subduction, as, for example, possible slab detachment, evolution of the slab geometry, and the thermal relaxation. It must be mentioned that our model is only two-dimensional. Three-dimensional effects such as a lateral propagating tear in a partly detached slab can not be considered (*Yoshioka and Wortel, 1995*).

7.2   The model

The model used here is equal to that described in the previous chapters 4 and 5. The model geometry is shown in Figure 5.1 (chapter 5). To realize cessation of subduction the velocity of the underthrusting plate (v_u) and of the overriding plate (v_o) vary with time. Figure 7.2 shows a sketch of the time evolution of the plate velocities. After the underthrusting plate has subducted for a few tens of million of years both the magnitudes of v_u and v_o and therewith the convergence velocity v_c start to decrease. Concerning our sign convention the velocity of the overriding plate is here negative (see Figure 5.1). In the following we note by the term 'decrease of the overriding plate velocity' a decrease of the absolute value. After the time period Δtc as indicated in Figure 7.2 the convergence velocity v_c has become zero and subduction has ceased. The time period between cessation of subduction and slab detachment is defined as Δtd. t_{pc} is defined as the time elapsed since subduction has ceased.
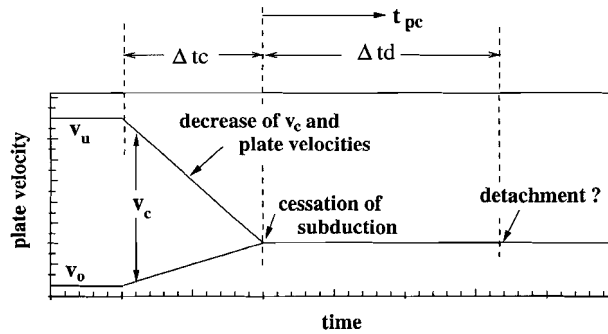

Figure 7.2 *Sketch of time evolution of plate velocities. v_u and v_o are the velocities of the underthrusting and overriding plate, respectively. v_c is the convergence velocity $v_u - v_o$. Δtc is defined as the time during which plate velocities decrease to zero. Δtd is the time period between cessation of subduction and slab detachment. t_{pc} is defined as the time elapsed since subduction has ceased.*

The viscosity is temperature- and depth-dependent as described in equation (4.1). The surface viscosity is 200 times the upper mantle viscosity, at 670 km depth viscosity increases by a factor of 50. The Rayleigh number (specified by the

reference viscosity η_0) varies between 10^6 and 10^7. Viscosity and Rayleigh number are chosen on the base of results of chapter 4 and 5. The time Δtc during which the convergence velocity decreases to zero changes between 10 and 50 Myr.

7.3   Results

This paragraph is divided into two parts: In the first part the evolution of the temperature structure is given. Converted seismic velocity anomaly structures are discussed in the second part.

Table 7.1 *Summary of Models*

case	$t=0$ v_u (cm/yr)	v_o (cm/yr)	v_m (cm/yr)	Δtc (Myr)	Ra		Δtd (Myr)
7.1	6	-2	0	10	10^6		190
7.2	6	-2	0	10	$5 \cdot 10^6$		40
7.3	6	-2	0	10	10^7		22
7.4	6	-2	0	50	10^6		217
7.5	6	-2	0	50	$5 \cdot 10^6$	$\Rightarrow$	41
7.6	6	-2	0	50	10^7		23
7.7	6	-2	1	20	10^6		-
7.8	6	-2	1	20	$5 \cdot 10^6$		16
7.9	6	-2	1	20	10^7		22

Table 7.1 summarizes the models discussed in the following. v_u, v_o, and v_m are the absolute plate velocities of the underthrusting and overriding plate, and the background mantle flow, respectively (see Figure 5.1 of chapter 5). Δtc is the time period during which plate velocities decrease to (the final plate velocity) zero. The rate of decrease of the underthrusting plate velocity v_u depends on the time period Δtc which is varied between 10 and 50 Myr. This rate could also be changed by taking a fixed Δtc but varying the initial plate velocity v_u. We assume, that changes in the initial v_u will have similar effects as changing Δtc. Thus we keep the initial plate velocity v_u in all models constant at 6 cm/yr. The overriding plate velocity v_o is taken to be initially -2 cm/yr throughout the experiments. The possible effect of a fixed overriding plate ($v_o = 0$) will be discussed below. Δtd is the time difference between cessation of subduction ($v_u = 0$, $v_o = 0$) and slab detachment. The arrow in Table 7.1 indicates that Δtd results from our models. All other parameters of Table 7.1 are imposed. (For Δtc and Δtd see also Figure 7.2) The sketch in Figure 7.3 defines slab detachment as it is used here. The subducting slab (left panel) has a monotonously increasing minimum temperature
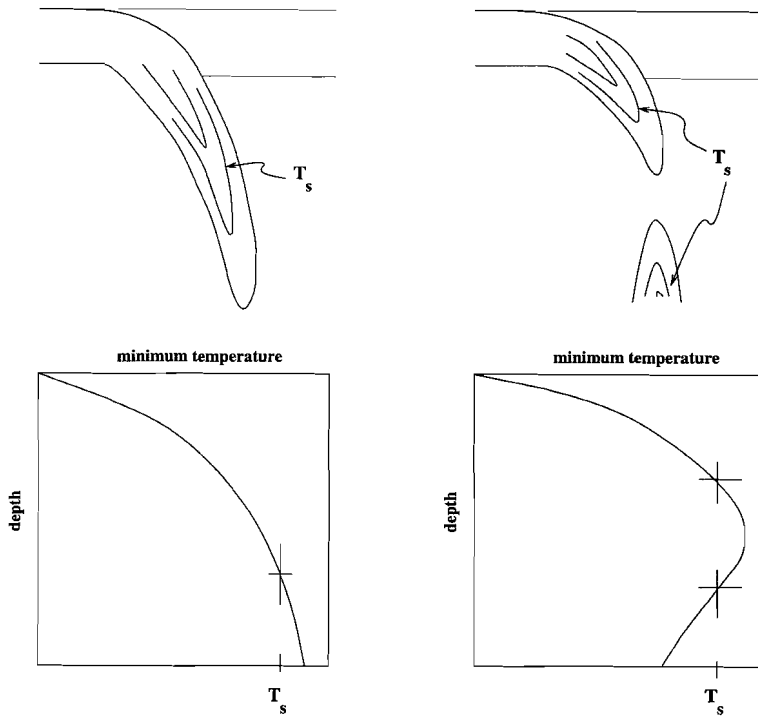
Figure 7.3 *Sketch of slab detachment. The subducting slab (left panel) has a monotonously increasing minimum temperature with depth. A specified temperature T_s is crossed by the graph of minimum temperature only once. After detachment (right panel) the minimum temperature does not increase monotonously, but has a local maximum where the slab is broken up. The temperature T_s is crossed twice by the curve of minimum temperature.*

with depth. A specified temperature T_s is crossed by the graph of minimum temperature only once. After detachment (right panel) the minimum temperature does not increase monotonously, but has a local maximum where the slab is broken up. The temperature T_s is crossed twice by the curve of minimum temperature. In the following, the time of detachment is specified as the isotherm $T_s = 1100°$C is devided. Isolines of lower temperature are torn earlier, those of higher values later. Thus we do not specify an absolute time of detachment, but give a comparable criterion among the model runs.

7.3.1 Temperature anomaly

(i) $\Delta tc = 10$ Myr, Ra varies between 10^6 and 10^7
Figure 7.4 (i) shows the time evolution of the plate velocities of case 7.1. The upper
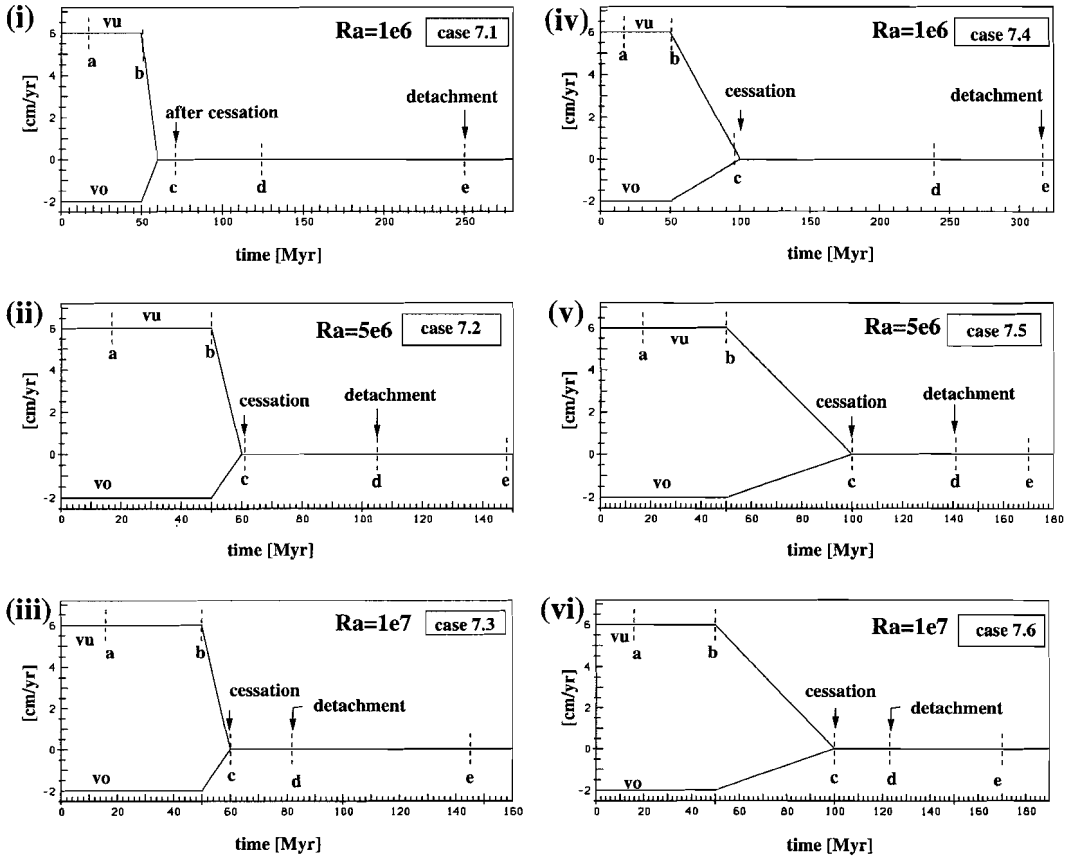
Figure 7.4 *Evolution of plate velocities of case 7.1 (i) to case 7.9 (ix). v_u and v_o is the underthrusting and overriding plate velocity, respectively. Letters indicate timesteps at which snapshots of the temperature field are shown. (continues on page 113)*

branch indicates the velocity of the underthrusting plate (v_u), the lower one that of the overriding plate (v_o). After 50 Myr both the underthrusting and overriding plate velocities begin to decrease. (Decrease of the overriding plate velocity means a decrease in magnitude). 10 Myr after decrease of the plate velocities has started (Δtc) v_u and v_o have become zero, i.e. the subduction process has ceased. The vertical dashed lines marked by letters indicate the timesteps of the temperature fields shown in Figure 7.5. The slab structure as shown in the first panel (a) is at the initial stage of subduction. As indicated by Figure 7.4 (i) at that time the subducting plate moves with 6 cm/yr towards the overriding plate which has a velocity of -2 cm/yr. The second panel of Figure 7.5 (b) shows the temperature field as developed just after the convergence velocity has started to decrease. The
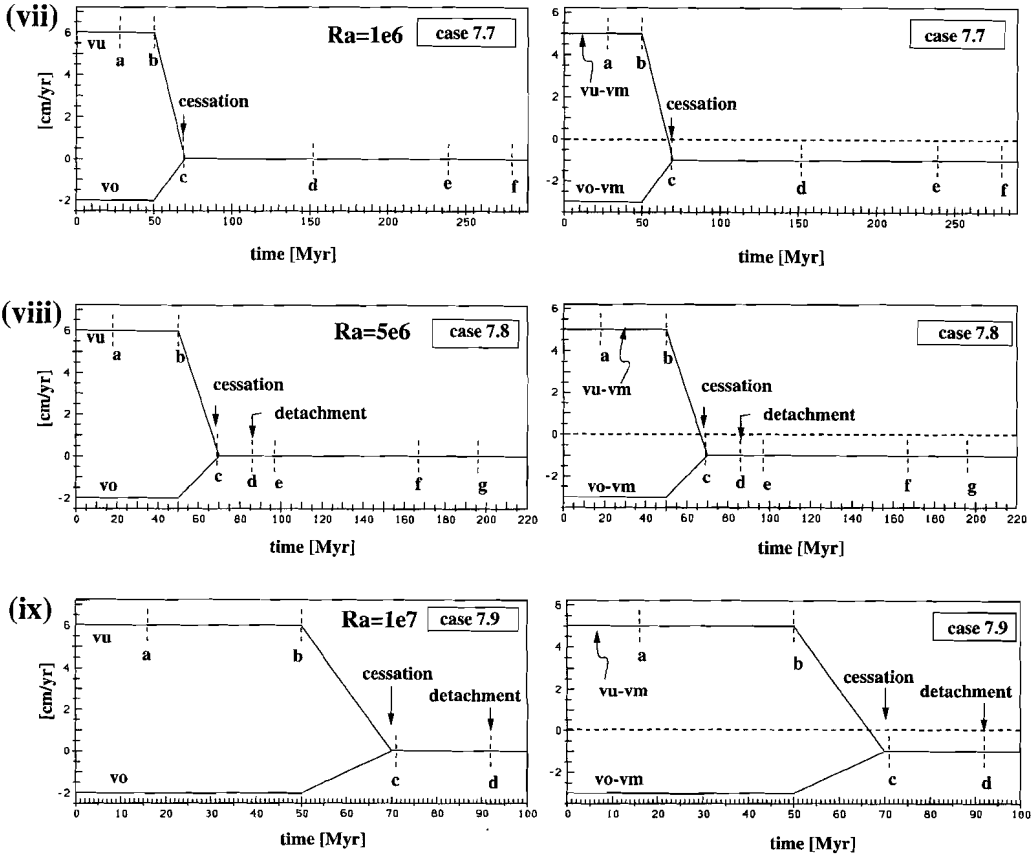

Figure 7.4 *continued   Left panels show absolute plate velocities (v_u, v_o) versus time as in Figure (i)-(vi). Right panels show the evolution of plate velocities relative to the background mantle flow ($v_u - v_m$, $v_o - v_m$). The dashed line indicates zero relative velocity between plates and mantle flow.*

dip angle of the slab is quite small at that stage. Figure 7.5 c shows the temperature field 10 Myr after subduction has ceased. By that time the dip angle has increased. The slab penetrates the lower mantle nearly vertically (Figure 7.5 d) and is detached (break up of the 1100 °C - isotherm) at about 250 Myr (Figure 7.5 e). This can be seen more clearly in Figure 7.6: isotherms are plotted, whereby the 1100°C - isoline is dashed.

Thinning of the slab structure and probably release from slab pull has already been started earlier. The time period Δtd between cessation and slab detachment is about 190 Myr.

The evolution of the plate velocities of case 7.2 is identical to the previous case 7.1 (Figure 7.4 ii). The Rayleigh number is with $5 \cdot 10^6$ five times as high as in the previous case. Figure 7.7 shows the evolution of the temperature of case 7.2.
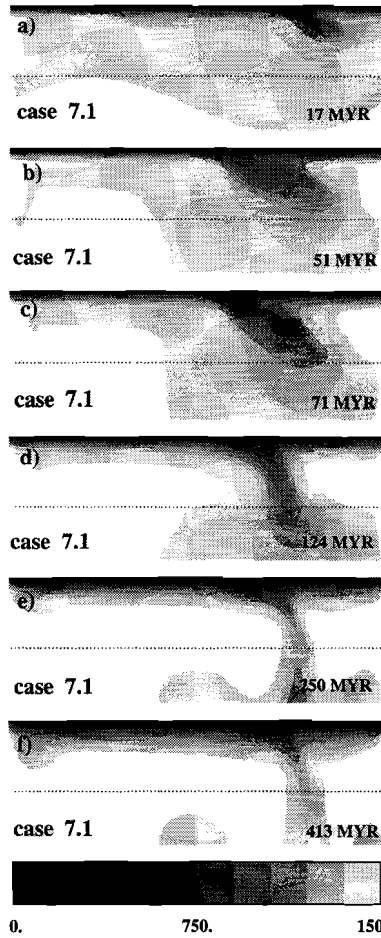
Ra = 1e6

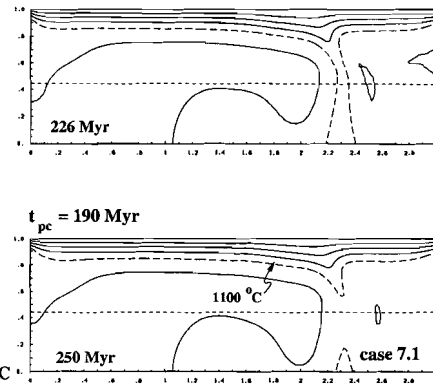<table>
<tr><td>Figure 7.5</td><td>Figure 7.6</td></tr>
</table>

left: *Evolution of the temperature field of case 7.1. Plate velocities are given in Figure 7.4 (i). Snapshots are shown at the subduction process (a), at the begin of the decrease of the convergence velocity (b), shortly after the cessation of subduction (c), at slab detachment - break up of the 1100 °C - isotherm (d), and long time afterwards (e, f).*

right: *Isotherms of case 7.1. 1100 °C-isotherm is dashed. t_{pc} is the time elapsed since cessation of subduction. Thus detachment takes place 190 Myr after subduction has ceased.*
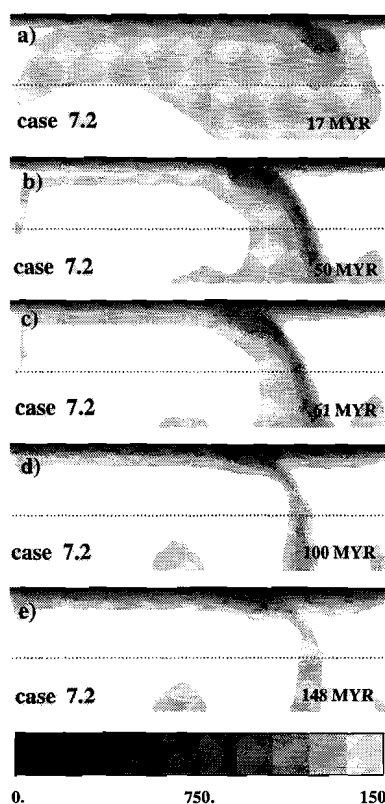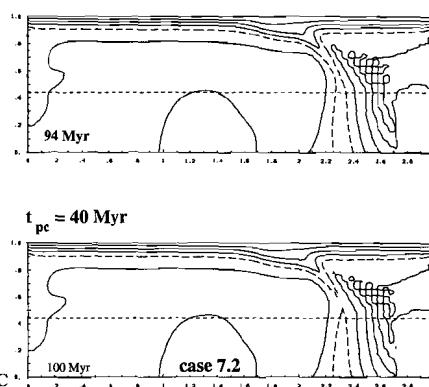
Ra = 5e6

Figure 7.7

Figure 7.8

left: As Figure 7.5. Slab detachment - break up of the 1100° C-isotherm - occurs ca. 40 Myr after cessation of subduction.
right: As Figure 7.6.

In relation to the lower Rayleigh number case (7.1) the subducting slab becomes thinner. Until plate velocities start to decrease (i.e. at 50 Myr after initiation of subduction) the slab has penetrated into the lower mantle (Figure 7.4 ii, 7.7 b). During the following 10 Myr, in which plate velocities become zero (Figure 7.4 ii), the slab structure does not change significantly (Figure 7.7 c). About 40 Myr after subduction has ceased slab detachment is observed (Figure 7.7 d and Figure 7.8 b), which occurs much earlier than in case 7.1.

In case 7.3 Rayleigh number is 10^7. Development of the plate velocities (Figure
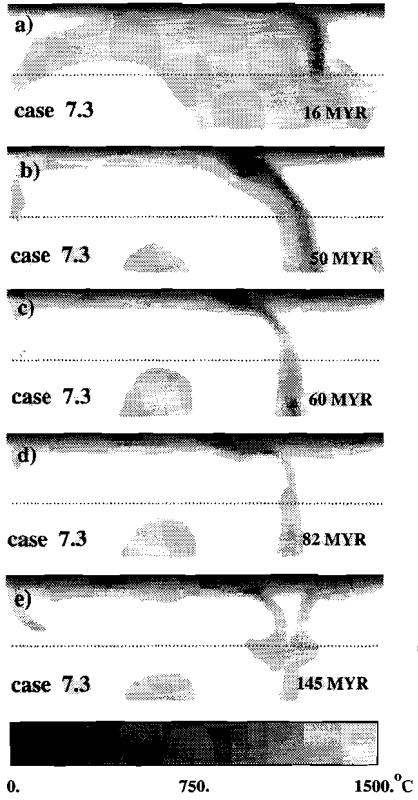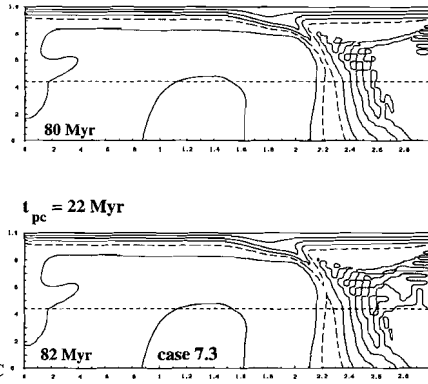
Ra = 1e7

Figure 7.9

Figure 7.10

left: As Figure 7.5. Slab detachment - break up of the 1100° C-isotherm - occurs 22 Myr after cessation of subduction.
right: As Figure 7.6.

7.4 iii) is the same as in the previous two models. During the first 50 Myr the slab subducts into the deep mantle (Figure 7.9 a, b). While convergence velocity decreases to zero during the following 10 Myr the temperature structure becomes thinner. Slab detachment occurs ca 22 Myr after cessation of subduction (Figure 7.9 d and 7.10 b).
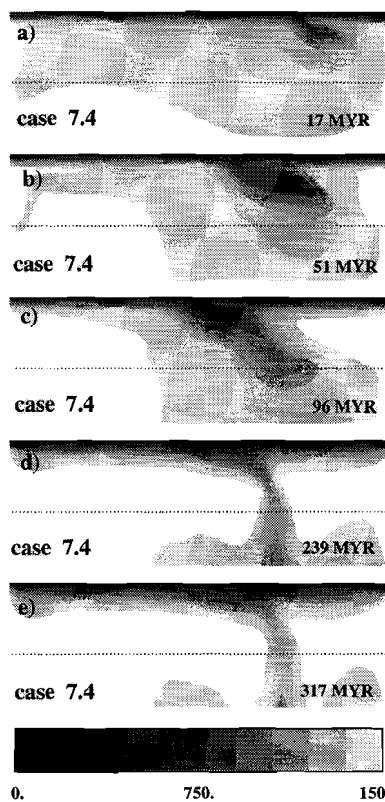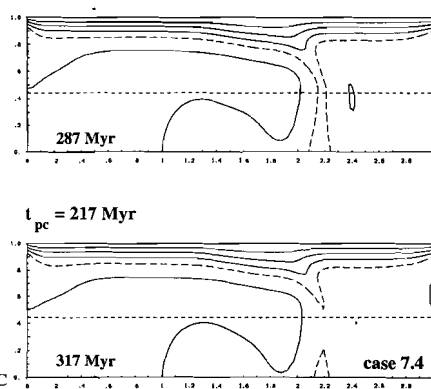
Ra = 1e6

Figure 7.11   **Figure 7.12**

left: As Figure 7.5. Slab detachment occurs 217 Myr after subduction has ceased.
right: As Figure 7.6.

(ii) $\Delta tc = 50$ *Myr, Ra varies between* 10^6 *and* 10^7

In the cases 7.4, 7.5, and 7.6 the time Δtc during which plate velocities decrease
to zero, is varied to 50 Myr. Rayleigh number is 10^6, $5 \cdot 10^6$, and 10^7 in case 7.4,
7.5, and 7.6, respectively. Figure 7.4 (iv) shows the course of the plate velocities
with time for case 7.4. Appropriate temperature fields of the time steps indicated
by letters are shown in Figure 7.11. The development of the subducting slab is
comparable to that of case 7.1 ($\Delta tc = 10$ Myr): The slab sinks with a small dip
angle into the mantle (Figure 7.11 a), the dip angle increases during the decrease
of plate velocities (Figure 7.11 b,c), to become nearly vertical (Figure 7.11 d). Slab
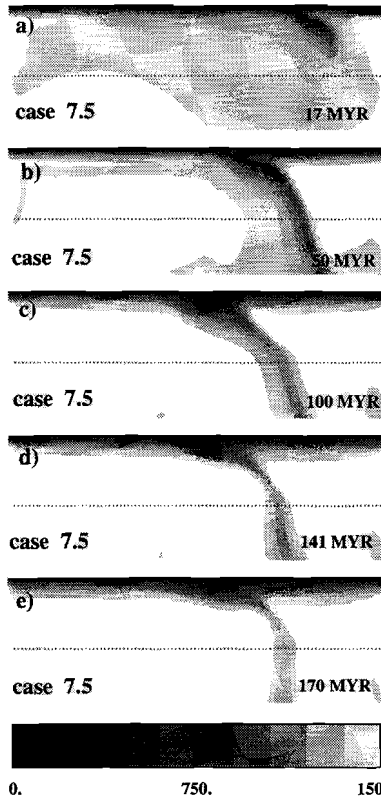
Ra = 5e6

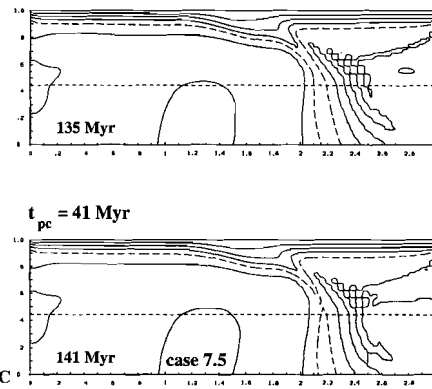Figure 7.13   Figure 7.14

left: As Figure 7.5. Slab detachment occurs 41 Myr after cessation of subduction.
right: As Figure 7.6.

detachment occurs more than 200 Myr after subduction has ceased (Figure 7.11 e and Figure 7.12 b). The time difference Δtd between cessation and detachment is ca. 217 Myr.

Figure 7.4 (v) and 7.13 show the time evolution of the plate velocities and the temperature field of case 7.5 ($Ra = 5 \cdot 10^6$). Time-dependent characteristics as have been discussed in chapter 5 are found. The peculiarity of these strongly time-dependent cases was, that, after deep mantle penetration had taken place, the dip angle of the subducting slab decreased and probably detachment occurred. This was found at even high trench migration rates of -4 cm/yr. Here, in case 7.5,
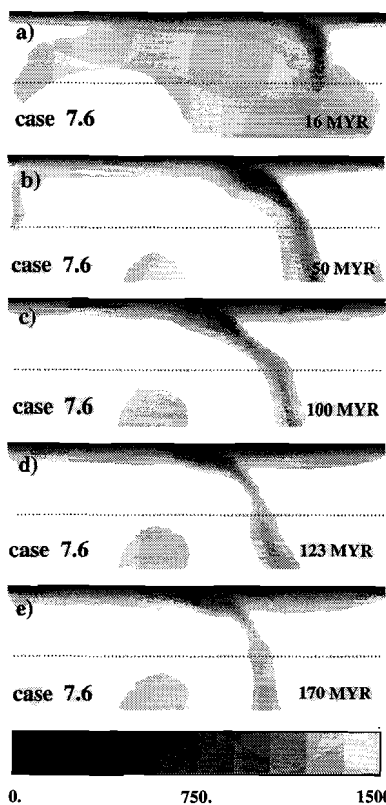
Ra = 1e7

Figure 7.15
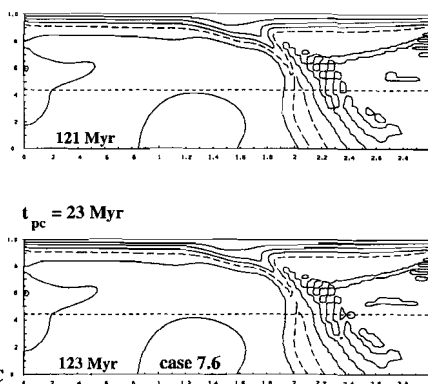
Figure 7.16

left: As Figure 7.5. Slab detachment occurs 23 Myr after cessation of subduction.
right: As Figure 7.6.

the sinking slab is in a stage of decreasing dip angle, when plate velocities decrease (between 50 and 100 Myr, see Figure 7.4 v). Contrary to the previous models, the dip angle decreases during that time, despite of the decrease of v_o which is equal to the trench migration rate. Slab detachment takes place ca. 40 Myr after cessation of subduction (Figure 7.13 d and Figure 7.14 b).

Plate velocities and temperature fields of case 7.6 are shown in Figure 7.4 (vi) and 7.15, respectively. Rayleigh number is 10^7. Slab detachment (Figure 7.15 d, 7.16 b) takes place ca. 23 Myr after cessation of subduction.

Ra = 1e6
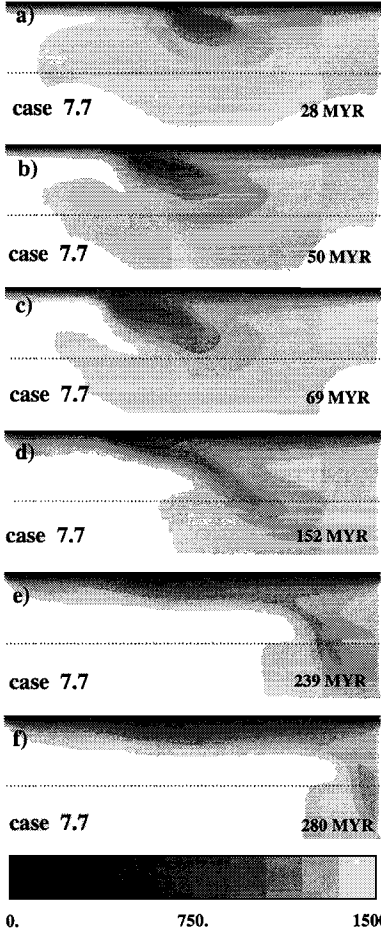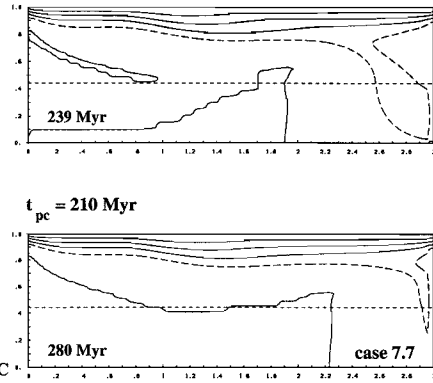
Figure 7.17   **Figure 7.18**

left: As Figure 7.5.
right: No slab detachment occurs before the slab disappears at the right sidewall.

(iii) $\Delta tc = 20$ *Myr, Ra varies between* 10^6 *and* 10^7, *additional mantle flow*
In these three cases (7.7 - 7.9) an additional background mantle flow of 1 cm/yr has
been included. Figure 7.4 (vii) shows the plate velocities versus time of case 7.7.
In the left panel the absolute plate velocities v_u and v_o are given, in the right panel
the velocities relative to the (upper) mantle flow are shown ($v_u - v_m$ and $v_o - v_m$).
When absolute plate velocities have decreased to zero, both plates move with -1

Ra = 5e6

Figure 7.19

Figure 7.20

left: As Figure 7.5. Slab detachment occurs 16 Myr after cessation of subduction.
right: As Figure 7.6.

Ra = 1e7
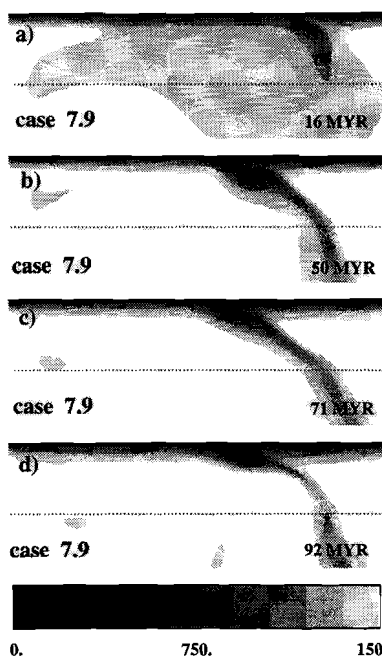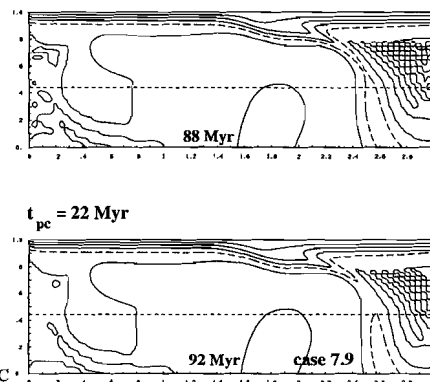
Figure 7.21   **Figure 7.22**

left: As Figure 7.5. Slab detachment occurs 22 Myr after cessation of subduction.
right: As Figure 7.6.

cm/yr relative to the mantle.

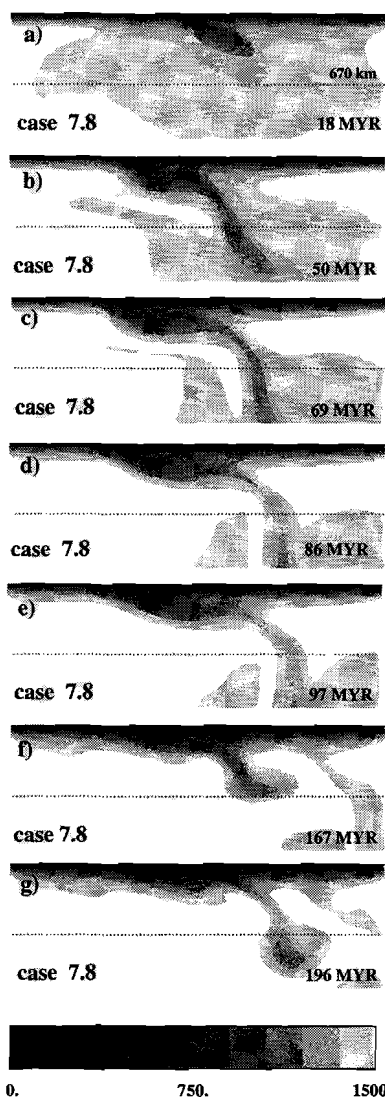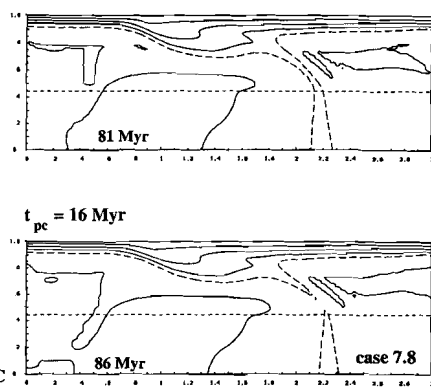After 50 Myr plate velocities start to decrease. 20 Myr (Δtc) later the subduction process ceases. The Rayleigh number is 10^6 in case 7.7. During the first 50 Myr the subducting slab penetrates into the (upper) mantle with a shallow dip angle (Figure 7.17 a,b). From then on plate velocities begin to decrease (see Figure 7.4 vii). As can be seen in Figure 7.18 slab detachment at least does not take place before the slab is transported to the right sidewall of the model domain. The development of plate velocities and the temperature field of the corresponding higher Rayleigh number case 7.8 ($Ra = 5 \cdot 10^6$) can be seen in Figure 7.4 (viii) and 7.19, respectively. At the moment when subduction has ceased (Figure 7.4 viii, Figure 7.19 c) the slab has already penetrated the lower mantle. Slab detachment occurs about 15 Myr afterwards (Figure 7.19 d and Figure 7.20 b). The background mantle flow transports the detached part of the slab away from the trench system.

New thermal boundary layer instabilities are formed, such as in Figure 7.19 f. These are also driven away by the mantle flow (Figure 7.19 g).

Evolution of the plate velocities and the temperature field of case 7.9 is shown in Figure 7.4 (ix) and 7.21, respectively. Dip angles are in general slightly decreased by the background mantle flow - compared to the the other two $Ra = 10^7$-cases. Slab detachment occurs about 22 Myr after the subduction process has ceased (Figure 7.21 d, 7.22 b).

7.3.2 Seismic velocity anomaly

Figure 7.23, 7.24, and 7.25 show the seismic P-wave velocity anomaly revealed by conversion of the temperature structure of the cases 7.4, 7.5 and 7.6, respectively. The transformation from the model temperature to the seismic velocity structure is described in chapter 3.3. After cessation of subduction (at 100 Myr) the magnitude of the seismic velocity anomaly decreases with time from about 7.5 % in the upper mantle by 1-2 %. However, in the lower mantle change in seismic anomaly is not that significant. In case 7.4, of which the time record is quite long, Δv_p decreases by ca. 1 %. The detached part of the subducted slab, indicated by the temperature anomaly structure, provides seismic velocity anomalies not higher than about 1.5%

Figure 7.23   **Figure 7.24**

left: Seismic p-wave velocity anomaly of case 7.4, $Ra = 10^6$. Corresponding temperature fields are shown in Figure 7.11 c-e. The method of conversion of the model temperature anomaly to Δv_p is described in chapter 3.3.
right: Seismic p-wave velocity anomaly of case 7.5, $Ra = 5 \cdot 10^6$. Corresponding temperature fields are shown in Figure 7.13 c-e.

(e.g. Figure 7.13 d,e; 7.15 d,e). Small anomalies of Δv_p within the lower mantle are partly caused by the decreasing sensitivity of the seismic velocity anomaly to temperature with depth (Figure 3.2). For a more detailed structure of the seismic velocity anomaly, particularly in the lower mantle, the greyscale of 0.5 - 1.5 % has been subdivided into four intervals. Figure 7.26 shows the seismic velocity structure of case 7.6 with the smaller divided greyscale. This shows clearly that Δv_p decreases in the lower mantle with time. Figure 7.27 shows the seismic velocity anomaly structure of the higher Rayleigh number cases of $5 \cdot 10^6 - 10^7$ at $t_{cp} = 100$ Myr, i.e. 100 Myr after subduction has stopped. In any case Δv_p is less than 0.75 % within the lower mantle or has even disappeared (Figure 7.27 b).
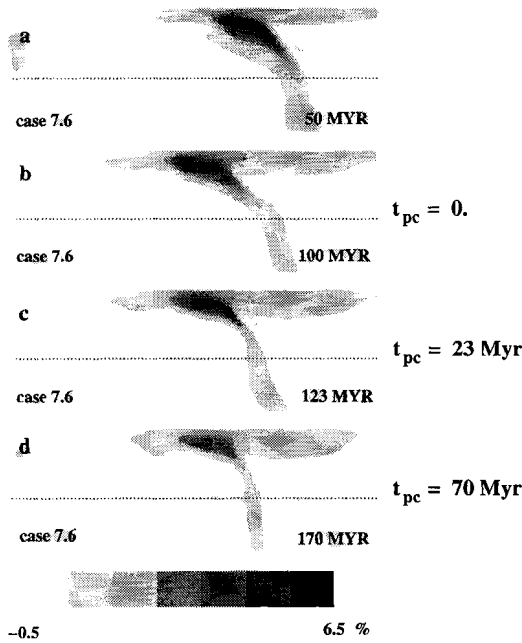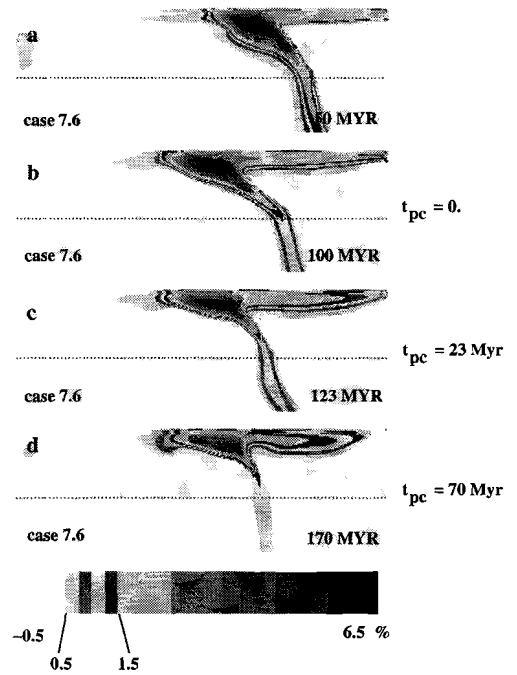
Figure 7.25   **Figure 7.26**
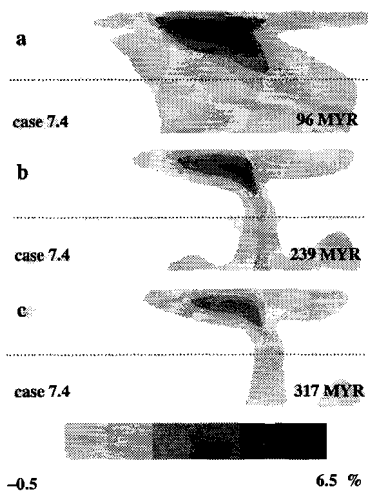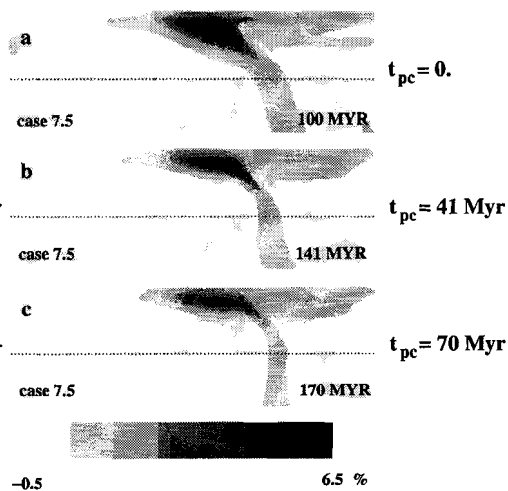
left: Seismic p-wave velocity anomaly of case 7.6, $Ra = 10^7$. Corresponding temperature fields are shown in Figure 7.15 b-e.
right: as Figure 7.25, but greyscale of value 0.5 - 1.5 % has split up into four intervals in order to show that in the lower mantle Δv_p decreases with time.
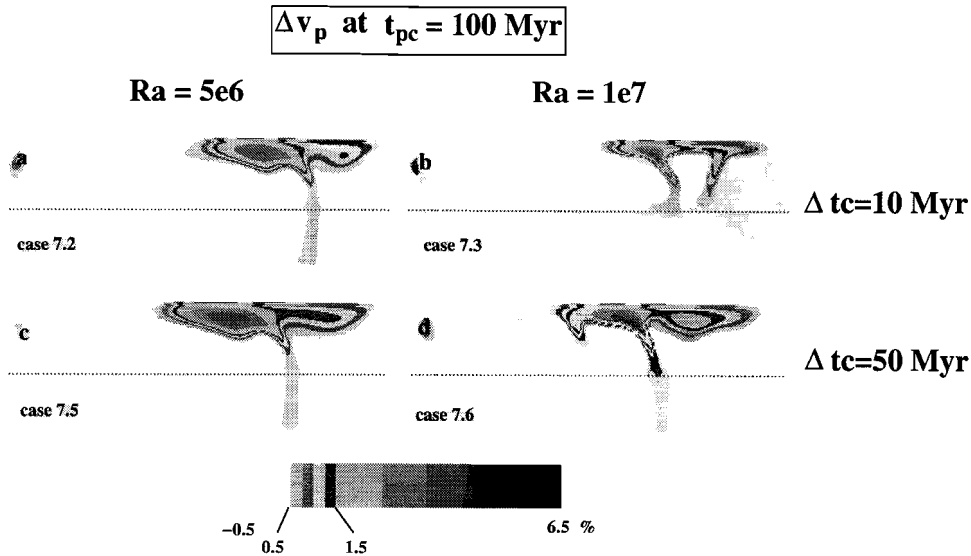
Figure 7.27 *Seismic velocity anomaly 100 Myr after subduction has ceased, i.e.*
$t_{pc} = 100$ *Myr. Anomalies are less than 0.75 % in the lower mantle. Rayleigh*
numbers are $5 \cdot 10^6$ *and* 10^7.

7.4   Discussion

Dip angle changes
50 Myr after subduction the underthrusting plate of each of the lower Rayleigh
number cases $(Ra = 10^6)$ has penetrated the upper mantle with a small dip angle.
During the following decrease of plate velocities the dip angle of the subducting
slab increases to about 45 °. After the subduction process has ceased $(v_c = 0)$ dip
angle continues to increase to nearly vertical and the slab penetrates into the lower
mantle.

In the higher Rayleigh number cases $(Ra = 5 \cdot 10^6, 10^7)$ the subducting slab has
already penetrated the lower mantle when plate velocities start to decrease. When
plate velocities decrease during a short time period (Δtc=10 Myr) slab structure
does not change significantly within that time. During 50 Myr of decrease of
the convergence velocity to zero the dip angle decreases within the upper mantle,
which is related to the time-dependent behaviour rather than to the change in plate
velocities. After cessation of subduction dip angle is increased to nearly vertical
within the lower mantle.

Slab detachment
Except from two models, slab detachment occurs about 200, 40, and 20 Myr

after cessation of subduction in Rayleigh number 10^6-, $5 \cdot 10^6$-, and 10^7-cases, respectively. The time period Δtc, during which convergence velocity decreases to zero, did not effect that. The two exceptions are cases 7.7 and 7.8: In case 7.7 no slab detachment occurred until the slab is transported by the mantle flow 'through the sidewall'. In case 7.8 detachment already takes place 16 Myr after subduction had stopped. Here, the moment of detachment is defined as the break up of one specified isotherm. Isotherms of lower value break up earlier (see Figure 7.3). Thus, release of slab pull and therewith uplift at the surface is likely to start earlier.

These results are in good agreement with the interpretation of uplift in regions of former subduction zones as the consequence of slab detachment (e.g. *Royden, 1993; Platt and Vissers, 1989*). The period Δtd between cessation of subduction and slab detachment is much too high for the cases with Rayleigh number of 10^6. Geological and tomographic studies of the Betic Alboran region or of the Carpathian arc suggest that slab detachment took place ca. 10 to 15 Myr after subduction had ceased (*Spakman, 1990; Blanco and Spakman, 1993; Royden, 1993*). Detachment of the subducted slab is expected to be accompanied by uplift, which could already begin with the thinning of the slab shortly after cessation but still before slab detachment is complete. That means, that the time between cessation of subduction and slab detachment (as defined in our models) at Rayleigh numbers of $5 \cdot 10^6$ and 10^7 is with values up to 40 Myr in better agreement with the timing of observed uplift associated with slab detachment. Moreover, two-dimensional modelling does not take into account three-dimensional effects as the lateral migration of a partly detached slab (*Yoshioka and Wortel, 1995*). Once a slab is torn, propagating of the tear might be fast. However, in two dimensions this effect is neglected and the 'whole' slab has to be detached at once, which could take more time. Thus, the time period between cessation of subduction and slab detachment will be overestimated in two-dimensional modelling.

Comparison with observations
In any case the structure of the detached part of the slab was nearly vertical. Even a horizontal background mantle flow did not hinder the slab from penetrating through the 670 km discontinuity and dip angle was 50° ($Ra = 10^6$) to nearly vertical ($Ra = 5 \cdot 10^6, 10^7$). Tomographic images of the area beneath southern Spain, such as shown in Figure 7.1, indicate a vertical structure which is associated with a detached part of a former subducted slab (*Blanco and Spakman, 1992*). Seismic data from the Carpathians suggest that slab geometry is nearly vertical - at least in the upper mantle (*Fuchs et al., 1979*). Following our results (also of chapter 5) steepening of the former subducted slab of the Carpathian trench system cannot be an effect of migration of the subduction zone towards the European foreland - as suggested by *Royden et al. (1983)* - but is rather a result of

decrease of plate velocities and the cessation of subduction.

Seismic velocity structure
Seismic velocity structure revealed by conversion of the model temperature to Δv_p did not show that clear detached slab structure as was found by the temperature structure. As the sensitivity of the seismic velocity anomaly to temperature anomalies decreases with depth (Figure 3.2) values of Δv_p only reach about 1.5 % in the lower mantle. A more detailed greyscale shows that amplitudes of Δv_p decrease after cessation of subductionnot only in the upper but also in the lower mantle. However, the evolution of the seismic velocity structure looks more like a thermal relaxation of the former subducted slab rather than slab detachment.

Tomographic images (such as in Figure 7.1) show two major differences compared to our results: First, the tomographic images show a separated area of high velocity anomaly associated with subducted lithosphere. Second, the detachment takes place at a shallower depth. However, amplitudes of the converted seismic velocity anomalies of the subducted slab agree with tomography results. The present day tomography image (Figure 7.1) shows probably a stage 20-30 Myr after subduction had ceased. This corresponds to a stadium of the slab in Figure 7.26 c, which shows the seismic velocity structure 23 Myr after cessation of subduction. Magnitudes of Δv_p of the detached part of the slab reach 1.5 % which is similar to the observed anomaly within the detached part of the slab beneath southern Spain (Tomography image in Figure 7.1).

100 Myr after subduction has ceased seismic velocity anomalies within the lower mantle are less than 0.75 % at the high Rayleigh number cases $Ra = 5 \cdot 10^6 - 10^7$). 70 Myr after cessation of subduction seismic anomalies were less 1 %. Since both the numerical solution procedure for the temperature field and the conversion from the model temperature to the seismic velocity anomaly bear errors, magnitudes of Δv_p less than 1% might be within margins of error. This implies that about 100 Myr after the subduction process was active it might not be possible to detect a detached part of the former subducted slab by e.g. tomography.

7.5   Conclusions

With our modelling of high viscosity slabs subducting into a viscous layered mantle we wanted to investigate the evolution of the subduction zone, when the subduction process ceases. During the decrease of the convergence velocity and after cessation of subduction the dip angle of the descending slab increases throughout the whole slab at Rayleigh number of 10^6 and in the lower mantle at higher Rayleigh numbers. The steepening of the dip angle is in agreement with tomography results of e.g. southern Spain (see Figure 7.1). It was found that the subducted slab will be detached after convergence velocity has become zero. The

time between cessation of subduction and slab detachment is not sensitive to the time in which plate velocities decrease to zero. However, it is strongly affected by the Rayleigh number. Compared with the tectonic evolution of the Betic Alboran and the Carpathian region as interpreted from geological and tomographic studies, detachment (break up of a specified isotherm) occurs too late at Rayleigh number of 10^6. Timing of detachment is at Rayleigh numbers between $5 \cdot 10^6$ and 10^7 in better agreement with the timing of uplift in regions of former active subduction zones associated with slab detachment (e.g. Carpathian arc, Betic-Alboran region).

As the sensitivity of the seismic velocity anomaly to temperature anomalies decreases with depth a detailed structure of slab detachment was not found. Decrease in magnitude of the seismic velocity anomaly with time - particularly in the lower mantle - looked more like thermal relaxation of the former subducted slab rather than detachment. In our model, the magnitudes of the seismic velocity anomalies of the detached part of the slab were 70 Myr after cessation of subduction less than 1%. Thus, about 100 Myr after subduction has ceased the former subducted slab is hardly 'visible' for seismic tomography anymore.

CHAPTER 8

Case studies: Application to NW Pacific subduction zones

8.1 Introduction

In this chapter we want to apply our model to specific subduction zones. Plate tectonic history and mainly oceanward trench migration seem to be significant in the evolution of the Izu Bonin and the Mariana subduction zone. *Van der Hilst and Seno (1993)* postulated that tectonic history in the North-West Pacific plays a key role for the different slab morphology between the Izu Bonin and the Mariana subduction zone. Tomography images indicate that beneath Izu Bonin the subducted slab is sub-horizontal within the transition zone, whereas the slab structure below the Mariana arc is almost vertical to a depth of about 1200 km (*Van der Hilst et al., 1981*).

Two models of the tectonic evolution of the North-West Pacific area are advocated. In the one model the tripple junction between the Philippine, Pacific, and Eurasian plate migrated from South-West to North-East accompanied by a clockwise rotation of the Philippine Sea plate (*Seno and Maruyama, 1984; Haston and Fueller, 1991*; for orientation see Figure 8.1 and Figure 2.1 of chapter 2). The other model advocated by e.g. *Hilde and Lee (1984)* does not have such a rotation.

Paleogeographic reconstructions, advocating the former model, suggest that the motion of the Pacific plate changed suddenly 43 Ma ago, accompanied with initiation of subduction along the proto-Mariana arc (*Seno and Maruyama, 1984*). Further north, along the proto-Izu-Bonin arc, subduction started about 48 Ma ago. Until ca. 40 Ma (late Eocene) the proto trench of the Izu Bonin subduction zone migrated northward. Between 40 and 30 Ma no further significant trench migration took place. Between about 30 to 17 Ma (late Oligocene to Middle Miocene) the Philippine plate was rotating clockwise. That caused a retrograde motion of the trench at Izu Bonin of ca. 7.5 cm/yr and at the Mariana arc of about 3 cm/yr. *Van der Hilst and Seno (1993)* argue that this difference in trench migration can explain why the slab beneath the Izu Bonin arc is stagnant at the upper-lower mantle boundary whereas the slab below the Mariana arc penetrates the lower mantle.

The purpose of the study of this chapter is to investigate *Van der Hilst and Seno's (1993)* qualitative explanation by our quantitave dynamical model. The
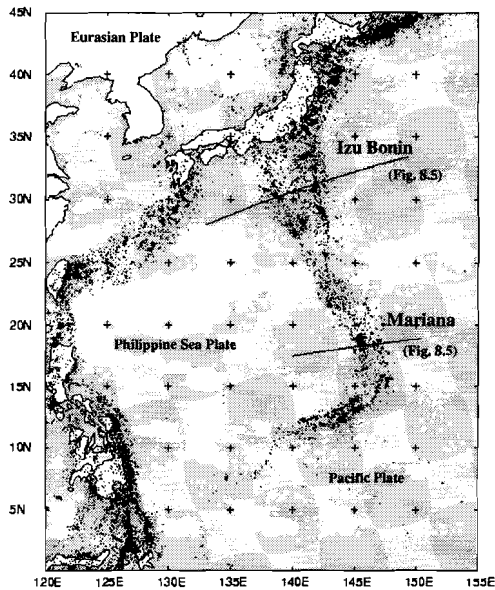
Figure 8.1 *Map of the northwestern Pacific region. Black dots represent epicentre locations for earthquakes larger than magnitude 4.5 on the Richter scale. Lines across the Izu Bonin arc and the Mariana arc indicate the position of the cross sections shown in Figure 8.5.*

results of chapter 5 have shown that in general trench migration can have a major effect on the evolution of subducting slabs.

8.2   The model set up and results

Model set up and simplification of the plate tectonic history
The model set up is equal to that used in the previous chapters (4,5,7). The model geometry is shown in Figure 5.1 (chapter 5). The evolution of the oceanward trench migration is represented by varying the overriding plate velocity with time. The underthrusting plate velocity is kept constant at 8 cm/yr. Based on results from chapter 4 and 5 the viscosity decreases from surface to the upper mantle by a factor

of 200, it increases at 670 km depth by a factor of 50. Results from chapter 4,5, and 7 have shown that sinking velocity of the subducting slab and the timing of slab detachment after cessation of subduction is for models with Rayleigh number of $5 \cdot 10^6$ and 10^7 in agreement with observed values, whereas the development of the subduction zone at Rayleigh number of 10^6 is too slow. Thus, here, the Rayleigh number is taken to be $5 \cdot 10^6$.

Figure 8.2 *Evolution of trench migration rate m_e which, here, is equal to the overriding plate velocity v_o. For the model case 'izu' trench migration rate increases during 15 Myr from zero to 7.5 c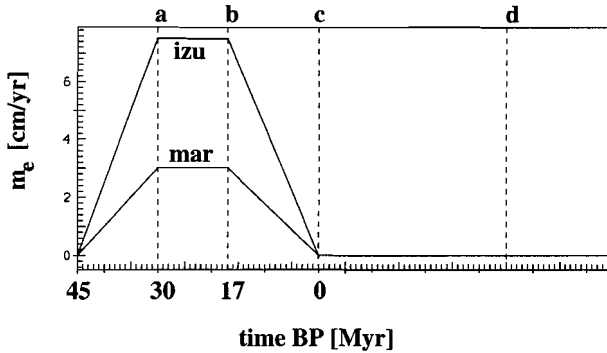m/yr. 13 Myr long the rate stays constant and decreases within 17 Myr again to zero. Maximum trench migration rate for the model case 'mar' is 3.0 cm/yr. The timing has been chosen in accordance with tectonic history in the NW Pacific (see text).*

Two models have been performed: one representing the Izu Bonin subduction zone (*izu*), the other to represent the situation at the Mariana subduction zone (*mar*). Figure 8.2 shows the development of the trench migration rate of the two models. Note that the trench migration rate is similar to the overriding plate velocity v_o. The time scheme is defined in that way, that initiation of subduction occurs 45 Ma ago. Therewith subduction starts about 2 Myr earlier and about 3 Myr later than it is supposed for the Mariana and the Izu Bonin subduction zone, respectively (*Seno and Maruyama, 1984*). This difference in development between northern and southern part of the ridge is important for the origin of the West Philippine basin (*Seno and Maruyama, 1984*).

However, testruns, which are not shown here, indicate that this time shift of initiation of subduction by a few Myr does not affect our results as described in the following. Another simplification in the plate tectonic history is the linear increase of the trench migration rate from initiation of subduction to 30 Ma. During these 15 Myr the migration rate increases to 7.5 cm/yr in case *izu* and to 3 cm/yr in case *mar*. Thus we neglect the first of the two distinct episodes of trench retreat at the Izu Bonin arc during 43-40 Ma ago. However, we think that the second episode of

Ra = 5e6   Ra = 5e6
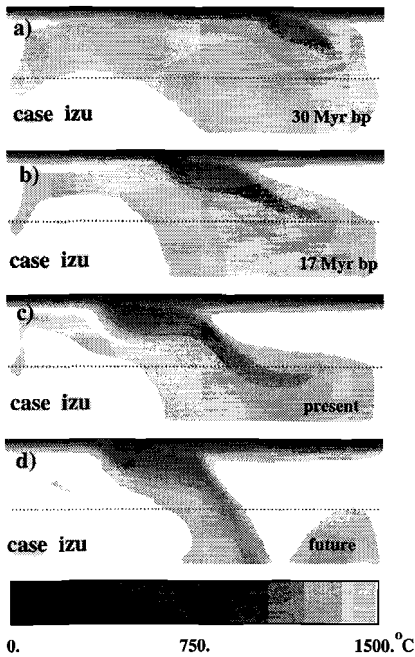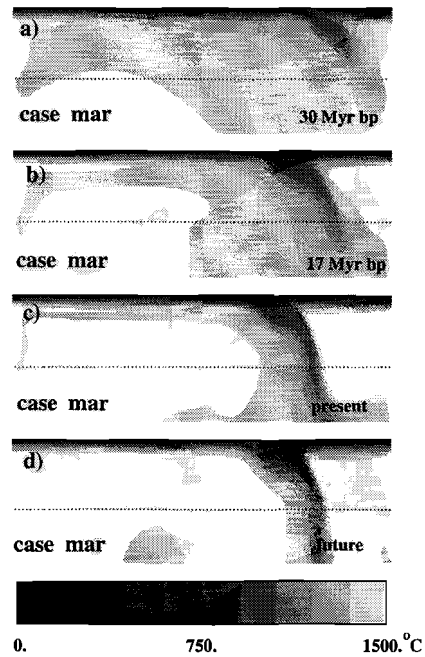
Figure 8.3   **Figure 8.4**

left: Evolution of the temperature field of case 'izu'. The underthrusting plate moves with 8 cm/yr toward the overriding plate. The trench migration rate m_e - equal to the overriding plate velocity - is shown in Figure 8.2. Subduction is initiated 45 bp. 15 Myr after initiation of subduction (a) trench migrates with 7.5 cm. This high rate hinders the slab from penetrating into the lower mantle (b). During the following decrease of trench migration within 17 Myr, in the upper mantle, the dip angle of the subducting slab has increased (c). Just below the 670 km discontinuity the temperature structure is horizontal. This stage corresponds to present time. 35 Myr after 'present' the dip angle increases to about 70° (d).
right: Evolution of the temperature structure of case 'mar'. 15 Myr after subduction was started and trench migration rate has increased to 3 cm/yr, the temperature structure is steeper than that of the corresponding timestep of the case 'izu' (a). After the period of constant trench migration the slab has penetrated the lower mantle (b). The dip angle increases with decreasing trench migration rate during the following 17 Myr until 'present' (c). From than on ($m_e = 0$) slab structure does not change significantly (d).

trench migration in the Miocene (30 - 17 Ma) plays the key role in the subduction zone evolution as proposed by *Van der Hilst and Seno (1993)*. Between 30 and 17

Ma the trench migration rate stays constant. From 17 Ma to the time which is defined as present (0), the migration rate decreases to zero. The nowadays trench migration rate is supposed to be small (*e.g. Griffiths et al., 1995*). However, for simplification migration rate is taken to be zero from present on. The letters a to d in Figure 8.2 indicate the time steps at which the temperature fields are shown in Figure 8.3 and 8.4 for case *izu* and *mar*, respectively.

Results

The first panel (a) of Figure 8.3 shows the temperature field 15 Myr after initiation of subduction. From then on the trench migrates with 7.5 cm towards the underthrusting plate. This high rate hinders the slab from penetrating into the lower mantle (Figure 8.3 b).

During the following decrease of trench migration within 17 Myr the dip angle of the subducting slab between ca. 300 - 670 km depth has increased (Figure 8.3 c) and the slab could just enter the lower mantle. Below the 670 km discontinuity the temperature structure is horizontal. Cessation of trench migration let the slab sink deeper into the lower mantle. 35 Myr after 'present' the dip angle increases to about 70° (Figure 8.3 d). Ca. 120 Myr after 'present' dip angle has further increased to about 90° (not shown). Figure 8.4 illustrates the evolution of the temperature field of the second case *mar*. 15 Myr after subduction was started and trench migration rate has increased to 3 cm/yr, the temperature structure is steeper than that of the corresponding timestep of the first case (Figure 8.3 a, Figure 8.4 a). After the period of constant trench migration the slab has penetrated the lower mantle (Figure 8.4 b). The dip angle increases with decreasing trench migration rate during the following 17 Myr until 'present' (Figure 8.4 c). From than on ($m_e = 0$) slab structure does not change significantly (Figure 8.4 d).

8.3 Discussion

The evolution of the two models differs significantly. In the first case, representing the Izu-Bonin subduction zone, a pronounced horizontal structure is found at the time corresponding to the present.

Figure 8.5 shows the seismic tomography structure beneath the Izu Bonin arc (left) and the Mariana arc (right). Tomographic images are from *Bijwaard, Spakman, and Engdahl (1996; in prep.)*. Similar images have been revealed by *Van der Hilst et al. (1991)*. Location of the cross sections are displayed in Figure 8.1. The high velocity structure below the Izu Bonin arc indicate that the subducting Pacific plate is flattened at the transition zone. Compared to the tomographic image in Figure 8.5 (left) the slab structure of our model *izu* is located too deep: it has already sunk below the 670 km discontinuity, whereas the tomographic structure (Figure 8.5) shows a slab laying above the upper-lower mantle boundary.
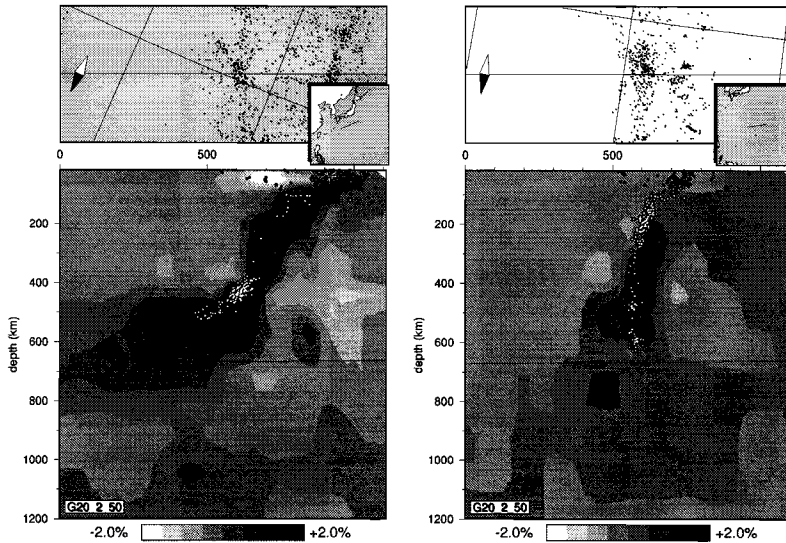
Figure 8.5 *Seismic tomography structure beneath Izu Bonin arc (left) and beneath Mariana arc (right). Tomography images are from Bijwaard, Spakman, and Engdahl (1996, in prep.). Similar images have been revealed by Van der Hilst et al. (1991). Top panels show maps for reference. For reference see also Figure 8.1. High velocity structure (positive anomalies) below the Izu Bonin arc indicate that the Pacific subducting Pacific plate is flattened at the transition zone. The velocity structure beneath the Mariana arc can be interpreted as a slab penetrating into the deep mantle. Dots in the map and the cross section indicate earthquakes.*

The simplification in tectonic history, as the neglect of the first episode of trench retreat, could be one reason for that difference. Moreover, a phase transition or a density interface, additional to the viscosity discontinuity, would probably hinder the descending slab from deep mantle penetration more effectful. As long as no significant trench retreat will occur, the slab structure beneath Izu Bonin might become similar to that of the Mariana subduction zone. This agrees with the speculation on the future slab morphology by *Van der Hilst and Seno (1993)*.

The second model - representing the Mariana subduction zone - shows a straight structure at the time corresponding with nowadays. The trench migration rate of 3 cm/yr during a period of 13 Myr does not flatten the slab structure.

Subduction zone geometry is consistent with the observed slab structure inferred from tomography as shown in Figure 8.5 (right). The seismic velocity anomalies beneath the Mariana arc indicate that the subducting plate penetrates nowadays with a nearly vertical dip angle into the deep mantle (Figure 8.5, right).

Our model results agree perfectly with the tomography results and therewith, confirm the relation between the tectonic history and present slab structure as proposed by *Van der Hilst and Seno (1993)*.

8.4 Conclusions

Our model results applied to the Izu-Bonin and the Mariana subduction zones support the relation between the plate tectonic history and the slab structure (revealed by tomography) as proposed by *Van der Hilst and Seno (1993)*. The difference in migration rate between the proto-Izu-Bonin trench and the proto-Mariana trench in late Oligocene to Middle Miocene (30 - 17 Ma) could be the reason for the nowadays observed slab structure: stagnant in the transition zone beneath the Izu-Bonin trench and penetrating into the deep mantle beneath the Mariana arc. *Van der Hilst and Seno's (1993)* analysis is based on the tectonic model which assumes the Philippine Sea plate rotating as a whole (*Seno and Maruyama, 1984; Haston and Fuellner, 1991*). Thus, implicitly, this tectonic model is supported by our results. Our dynamical model, using their plate tectonic scenario as input, predicts a present-day subduction zone structure which is in good agreement with the tomographic images.

References

Akaogi, M. and E. Ito, Refinement of enthalpy measurements of Mg_2SiO_3 perovskite and negative pressure-temperature slopes for perovskite-forming reactions, *Geophys. Res. Lett., 20*, 1839-1842, 1993.

Akaogi, M., E. Ito, and A. Navrotsky, Olivine-modified spinel- spinel transition in the system Mg_2SiO_4 - Fe_2SiO_4: Calorimetric measurements, thermomechanical calculation, and geophysical application, *J. Geophys. Res., 94*, 15671-15685, 1989.

Aki, K. and W. Lee, Determination of three-dimensional velocity anomalies under a seismic array using first P arrival times from local earthquakes, *J. Geophys. Res., 81*, 4381-4399, 1976.

Aki, K., A. Christoffersson, and E.S. Husebye, Determination of the three-dimensional seismic structure of the lithosphere, *J. Geophys. Res., 82*, 277-296, 1977.

Anderson, D.L., Phase changes in the upper mantle, *Science, 157*, 1165-1173, 1967.

Anderson, D.L., Chemical boundaries in the mantle, in: Glacial isostacy, sea-level and mantle rheology, ed. R. Sabadini and K. Lambeck, Kluwer Academic Publishers, Dordrect, 1990.

Anderson, D.L., C. Sammis, and T. Jordan, Composition of the mantle and core, in *The nature of the solid Earth*, ed. E.C. Robertson, J.F. Hays, and L. Knopoff, pp. 41-66. McGraw-Hill, New York, 1972.

Archambeau, C.B., E.A. Flinn, and D.G. Lambert, Fine structure of the upper mantel, *J. Geophys. Res., 74*, 5825-5865, 1969.

Barazangi, M. and B.L. Isacks, Spatial distribution of earthquakes and subduction of the Nazca plate beneath South America, *Geology, 4*, 686-692, 1976.

Bass, J.D. and D.L. Anderson, Composition of th eupper mantle: Geophysical tests of two petrological models, *Geophys. Res. Lett., 11*, 237-240, 1984.

Bills, B.G. and G.M. May, Lake Bonneville: Constraints on lithospheric thickness and upper mantle viscosity from isostatic warping of Bonneville, Provo, and Gilbert stage shorelines, *J. Geophys. Res., 92*, 11493-11508, 1987.

Bills, B.G., D.R. Currey, and G.A. Marshall, Viscosity estimates for the crust and upper mantle from patterns of lacustrine shoreline deformation in the Eastern Great Basin, *J. Geophys. Res., 99*, 22059-22086, 1994.

Bina, C.R. and B.J. Wood, Olivine-spinel transition: Experimental and thermodynamic constraints and implications for the nature of the 400-km seismic discontinuity, *J. Geophys. Res., 92*, 4853-4866, 1987.

Blanco, M.J. and W. Spakman, The P-wave velocity structure of the mantle below the Iberian Peninsula: evidence for subducted lithosphere below southern Spain, *Tectonophysics, 221*, 13-34, 1993.

Buforn, E., A. Udias, and R. Madariaga, Intermediate and deep earthquakes in Spain, *Pur Appl. Geophys., 136*, 375-393, 1991.

Burnley, P.C., H.W. Green, and D.J. Prior, Faulting associated with the olivine to spinel transformation in Mg_2GeO_4 and its implications for deep-focus earthquakes, *J. Geophys. Res., 96*, 1991

Cahill, T. and B.L. Isacks, Seismicity ansd shape of the subducted Nazca plate, *J. Geophys. Res., 97*, 17503-17529, 1992.

Chase, C.G., Plate kinematics: The Americas, East Afrika, and the rest of the world, *Earth Planet. Sci. Lett., 37*, 355-368, 1978.

Chopelas, A., Thermal properties of forsterite at mantle pressures derived from vibrational spectroscopy, *Phys. Chem. Min., 17*, 149-156, 1990.

Chopelas, A. and R. Boehler, Thermal expansion measurements at very high pressure, systematics and a case for a chemically homogeneous mantle, *Geophys. Res. Lett., 16*, 1347-1350, 1989.

Chopelas, A. and R. Boehler, Thermal expansivity in the lower mantle, *Geophys. Res. Lett., 19*, 1983-1986, 1992.

Christensen, U.R., Models of mantle convection: One or several layers, *Phil. Trans. R. Soc. London Ser. A, 328*, 417-424, 1989.

Christensen, U.R., The influence of trench migartion on slab penetration into the lower mantle, *Earth Planet. Sci. Lett., 140*, 27-39, 1996.

Christensen, U.R. and D.A. Yuen, The interaction of a subducting lithospheric slab with a chemical or phase boundary, *J. Geophys. Res., 89*, 4389-4402, 1984.

Christensen, U.R. and D.A. Yuen, Layered convection induced by phase transitions, *J. Geophys. Res., 90*, 10,291-10,300, 1985.

Cormier, V.F., Slab diffraction of S waves, *J. Geophys. Res., 94*, 3006-30024, 1989.

Creager, K.C. and T.H. Jordan, Slab penetration into the lower mantle, *J. Geophys. Res., 89*, 3031-3049, 1984.

Creager, K.C., Jordan, T.H., Slab penetration into the lower mantle beneath the Mariana and other island arcsof the northwest Pacific, *J. Geophys. Res., 91*, 3573-3589, 1986.

Chung, D.H. Elasticity and equations of state of olivines in the Mg_2SiO_4-Fe_2SiO_4 system, *Geophys. J. R. Astr. Soc., 25*, 511-538, 1971.

Davies, G.F., Penetration of plates and plumes through the mantle transition zone, *Earth Planet. Sci. Lett., 133*, 507-516, 1995.

Davies, D. and D.P. McKenzie, Seismic travel time residuals and plates, *Geophys. J. R. Astron. Soc., 18*, 51-63, 1969.

Davies, G.F. and M.A. Richards, Mantle convection, *J. Geol., 100*, 151-206, 1992.

De Jonge, M.R., Geodynamic evolution and mantle structure, Mededelingen van de Faculteit Aardwetenschappen Universiteit Utrecht, Netherlands, PhD-thesis, No. 127, 1995.

De Jonge, M.R., M.J.R. Wortel, and W. Spakman, Regional scale tectonic evolution and the seismic velocity structure of the lithosphere and upper mantle: the Mediterranean region, *J. Geophys. Res., 99*, 12091-12108, 1994.

DeMets, C., R.G. Gordon, D.F. Argus, and S. Stein, Current plate motions, *Geophys. J. Int, 101*, 425-478, 1990.

DeMets, C., R.G. Gordon, D.F. Argus, and S. Stein, Effect of recent revisions to the geomagnetic reversal time scale on estimates of current plate motions, *Geophys. Res. Lett., 21*, 2191-2194, 1994.

Doglioni, C., A proposal for the kinematic modelling of W-dipping subductions - possible applications to the Tyrrhenean-Apennines system, *Terra Nova, 3*, 423-434, 1990.

Doglioni, C., I. Moretti, and F. Roure, Basal lithospheric detachment, eastward mantle flow and Mediterranean geodynamics: a discussion, *J. Geodynamics, 1*, 47-65, 1991.

Dziewonski, A.M. and D.L. Anderson, Preliminary reference Earth model, *Phys. Earth Planet. Inter., 25*, 297-356, 1981.

Dziewonski, A.M. and J.H. Woodhouse, Global images of the Earth's interior, *Science, 236*, 37-48, 1987.

Fuchs, K., P. Bonjer, G. Bock, D. Cornea, C. Radu, D. Enescu, D. Jiame, G. Nouescu, G. Merkler, Moldoveanu, and G. Tudorache, Aftershocks and migration of seismic activity, *Tectonophysics, 53*, 225-247, 1979.

Fukao, Y., M. Obayashi, H. Inoue, and M. Nenbai, Subducting slabs stagnant in the mantle transition zone, *J. Geophys. Res., 97*, 4809-4822, 1992.

Funamori, N. and T. Yagi, High pressure and high temperature in situ x-ray observation of MgSiO3 perovskite under lower mantle conditions, *Geophys. Res. Lett., 20*, 387-390, 1993.

Gaherty, J.B. and B.H. Hager, Compositional vs. thermal buoyancy and the evolution of subducted lithosphere, *Geophys. Res. Lett., 21*, 141-144, 1994.

Garfunkel, Z., C.A. Anderson, and G. Schubert, Mantle circulation and the lateral migration of subducted slabs, *J. Geophys. Res., 91*, 7205-7223, 1986.

Giardini, D. and J.H. Woodhouse, Horizontal shear flow in the mantle beneath the Tonga arc, *Nature, 319*, 551-555, 1986.

Graham, E.K. and G.R. Barsch, Elastic constants of single-crystal forsterite as a function of temperature and pressure, *J. Geophys. Res., 74*, 5949-5972,1969.

Griffiths, R.W., R.I. Hackney, and R.D. Van der Hilst, A laboratory investigation of effects of trench migration on the descent of subducted slabs, *Earth Planet. Sci. Lett., 133, 1-17*, 1995.

Gripp, A.E. and R.G. Gordon, Current plate velocities relative to the hotspots incorporating the Nuvel-1 global plate motion model, *Geophys. Res. Lett., 17*, 1109-1112, 1990.

Gubbins, D. and R. Snieder, Dispersion of P waves in subducted lithosphere: evidence for an eclogite layer, *J. Geophys. Res., 96*, 6321-6333, 1991.

Guillou-Frottier, L., J. Buttles, and P. Olson, Laboratory experiments on the structure of subducted lithosphere, *Earth Planet. Sci. Lett., 133*, 19-34, 1995.

Gurnis, M. and B.H. Hager, Controls on the structure of subducted slabs, *Nature 335*, 317-321, 1988.

Gwanmesia, G.D., S Rigden, I. Jackson, and R.C. Lieberman, Pressure dependence of elastic wave velocity for β-Mg2SiO4 and the composition of the Earth's mantle, *Science, 250*, 794-797, 1990.

Hager, B.H., Subducted slabs and the geoid: Constraints on mantle rheology and flow, *J. Geophys. Res., 89*, 6003-6015, 1984.

Hager, B.H. and R. Clayton, Constraints on the structure of mantle convection using seismic observations, flow models, and the geoid, In: *Mantle Convection: Plate Tectonicss and Global Dynamics*, ed. W.R. Peltier, pp 657-763, New York: Gordon and Breach, 1989.

Hager, B.H. and M.A. Richards, Long-wavelength variations in Earth's geoid: physical model and dynamical implications, *Phil. Trans. R. Soc. London Ser. A 328*, 309-327, 1989.

Hager, B.H., R.W. Clayton, M.A. Richards, R.P. Comer, and A.M. Dziewonski, Lower mantle heterogeneity, dynamic topgraphy and the geoid, *Nature, 313*, 541-545, 1985.

Hansen, U., and A. Ebel, Time-dependent thermal convection - a possible explanation for a

multi-scale flow in the Earth's mantle, *Geophys. J., 94*, 181-191, 1988.

Hansen, U., D.A. Yuen, S.E. Kroening, and T.B. Larsen, Dynamical consequences ofdepth-dependent thermal expansivity and viscosity on mantle circulations and thermal structure, *Phys. Earth Planet. Inter., 77*, 205-223, 1993.

Harland, W.B., A.V. Cox, P.G. Llewellyn, C.A.G. Pickton, A.G. Smith, and R. Walters, *A geologic time scale*, 131 pp, Cambridge Univ. Press, New York, 1982.

Hasegawa, A. and I.S. Sacks, Subduction of the Nazca plate beneath Peru as determined from seismic observations, *J. Geophys. Res., 86*, 4971-4980, 1981.

Haston, R. B. and M. Fueller, Paleomagnetic data from the Philippine Sea plate and their tectonic significance, *J. Geophys. Res, 96*, 6073-6098, 1991.

Heinrich, J.C., P.S. Huyakorn, and O.C. Zienkiewicz, An 'Upwind' Finite Element scheme for two-dimensional convective transport equation, *Int. J. for Numerical Methods in Engineering, 11*, 131-134, 1977.

Hilde, T. W. C. and C.-S. Lee, Origin and evolution of the West Philippine Basin: A new interpretation, *Teconophysics, 102*, 85-104, 1984.

Hilgen, F.J., Extension of the astronomically calibrated (polarity) time scale to the Miocene/Pliocene boundary, *Earth Planet. Sci. Lett., 107*, 349-368, 1991.

Honda, S., D.A. Yuen, S. Balachandar, and D. Reuteler, Three- dimensional instabilities of mantle convection with multiple phase transitions, *Science, 259*, 1308-1311, 1993a.

Honda, S., S. Balachandar, D.A. Yuen, and D. Reuteler, Three- dimensional mantle dynamics with an endothermic phase transition, *Geophys. Res. Lett., 20*, 221-224, 1993b.

Irifune, T. and A.E. Ringwood, Phase transformations in subducted oceanic crust and buoyancy relationships at depths of 600- 800 km in the mantle, *Earth Planet. Sci. Lett., 117*, 101-110, 1993.

Isaak, D.G., O.L. Anderson, T. Goto, and I. Suzuki, Elasticity of single-crystal forsterite measured to 1700K, *J. Geophys. Res., 94*, 5895-5906, 1989.

Isacks, B. and P. Molnar, Distributions of stresses in the descending lithosphere from a global survey of focal mechanism solutions of mantle earthquakes, *Rev. Geophys. Space Phys., 9*, 103-174, 1971.

Isacks, B., J. Oliver, and L.R. Sykes, Seismology and the new global tectonics, *J. Gephys. Res., 73*, 5855-5899, 1968.

Ito, E., M. Akaogi, L. Topor, and A. Navrotsky, Negative pressure-temperature slopes for reactions forming $MgSiO_3$ perovskite from calorimetry, *Science, 249*, 1275-1278, 1990.

Ito, E. and H. Sato, Effect of phase transformations on the dynamics of the descending slab, *High-pressure research: Application to Earth and Planetary Sciences*, edited by Y. Syono and M. H. MAnghnani, pp. 257-262, 1992.

Ito, E. and E. Takahashi, Postspinel transforms in the system Mg_2SiO_4 and some geophysical implications, *J. Geophys. Res., 94*, 10,637-10,646, 1989.

Jarrard, R.D., Relations among subduction parameters, *Rev. Geophys., 24*, 217-284, 1986.

Jeanloz, R. and E. Knittle, Density and composition of the lower mantle, *Phil. Trans. R. Soc. London Ser. A 328*, 377-389, 1989.

Jordan, T.H., Lithospheric slab penetration into the lower mantle beneath the sea of Okhotsk, *J. Geophys., 43*, 473-496, 1977.

Jordan, T.H., A.L. Lerner-Lam, and K.C. Creager, Seismic imaging of boundary layers and deep mantle convection. In *Mantle Convection: Plate Tectonics and Global Dynamics*, ed. W.R. Peltier, pp 97-201, New York: Gordon and Breach, 1989.

Kennet, B.L.N. and E.R. Engdahl, Travel times for global earthquake location and phase identification, *Geophys. J. Int., 105*, 429-466, 1991.

Kerr, R.A., Putting Stiffness in Earth's Mantle, *Science, 271*, 1053-1054, 1996.

Kincaid, C. and P. Olson, An experimental study of subduction and slab migration, *J. Geophys. Res., 92*, 13,832-13,840, 1987.

King, S.D. and B.H. Hager, Subducted slabs and the geoid 1. Numerical experiments with temperature-dependent viscosity, *J. Geophys. Res., 99*, 19843-19852, 1994.

Kirby, S., Interslab earthquakes and phase changes in subducting lithosphere, *Rev. Geophys.*, Supplement, U.S. Nat. Report to IUGG 1991-1994, 287-297, 1995.

Kirby, S.H., W.B. Durham, and L.A. Stein, Mantle phase changes and deep-earthquakes faulting in subducting lithosphere, *Science, 252*, 216-225, 1991.

Knittle, E., R. Jeanloz, and G.L. Smith, The thermal expansion of silicate perovskite and stratification of the Earth's mantle, *Nature, 319*, 214-216, 1986.

Lambeck, K., Evidence for lateral mantle viscosity structure, *EOS Trans. AGU, 71*, 1568, 1990.

Lambeck, K., P. Johnston, and M. Nakada, Holocene glacial rebound and sea-level change in north-western Europe, *Geophys. J. Inter., 103*, 451-468, 1990.

Lay, T., Localized velocity anomalies in the lower mantle, *Geophys. J. R. Astron. Soc., 72*, 483-516, 1983.

Lay, T., The fate of descending slabs, *Annu. Rev. Earth Planet. Sci., 22*, 33-61, 1994.

Lowman, J.P. and G.T. Jarvis, Mantle convection models of continental collision and breakup incorporating finite thickness plates, *Phys. Earth Planet. Inter., 88*, 53-68, 1995.

Machetel, P. and P. Weber, Intermittent layered convection in a model mantle with an endothermic phase change at 670 km, *Nature, 350*, 55-57, 1991.

McAdoo, D.C., Geoid anomalies in the vicinity of subduction zones, *J. Geophys. Res., 86*, 6073-6090, 1981.

McKenzie, D. P., Speculations on the consequences and causes of plate motions, *Geophys. J. R. Astr. Soc., 18*, 1-32, 1969.

Minster, J.B. and T.H. Jordan, Present-day plate motions, *J. Geophys. Res., 83*, 5331-5354, 1978.

Mizutani, H.Y., Y. Hamano, Y. Ida, and S. Akinoto, Compressional wave velocities of fayalite, Fe_2SiO_4 spinel and coesite, *J. Geophys. Res., 75*, 2741-2747, 1970.

Nakada, M., K. Lambeck, Glacial rebound and relative sea-level variations: a new appraisal, *Geophys. J. R. Astron. Soc., 90*, 171-224, 1987.

Nakada, M., K. Lambeck, Late Pleistocene and Holocene sea-level change in the Australian region and mantle rheology, *Geophys. J., 96*, 497-517, 1989.

Okano, K. and D. Suetsugu, Search for lower mantle high-velocity zones beneath the deepest Kurile and Mariana earthquakes, *Geophys. Res. Lett., 19*, 745-748, 1992.

Paulssen, H., Evidence for a sharp 670-km discontinuity as inferred from P-to-S converted waves, *J. Geophys. Res., 93*, 10489-10500, 1988.

Peltier, W.R. and L.P. Solheim, Mantle phase transitions and layered chaotic convection,

Geophys. Res. Lett., 19, 321-324, 1992.

Platt, J.P. and R.L.M. Vissers, Extensional collapse of thickened continental lithosphere: A working hypothesis for the Alboran Sea and Gibraltar arc, *Geology, 17*, 540-543, 1989.

Revenaugh, J. and T.H. Jordan, Mantle layering from ScS reverberations 2. The transition zone, *J. Geophys. Res., 96*, 19,763-19,780, 1991.

Ricard, Y., B. Wuming, Inferring the viscosity and the 3-D density structure of the mantle from geoid, topography and plate velocities, *Geophys. J. Int., 105*, 561-571, 1991.

Ricard, Y., C. Doglioni, and R. Sabadini, Differential rotation between lithosphere and mantle: A consequence of lateral mantle viscosity variations, *J. Geophys. Res., 96*, 8407-8415, 1991.

Richards, M.A. and G.E. Davies, On the separation of relatively buoyant components from subducted lithosphere, *Geophys. Res. Lett., 16*, 831-843, 1989.

Richter, F.M., Focal mechanisms and seismic energy release of deep and intermediate earthquakes in the Tonga-Kermadec region and their bearing on the depth extent of mantle flow, *J. Geophys. Res., 84*, 6783-6795, 1979.

Ringwood, A.E., Phase transformations and differentiation in subducted lithosphere: implications for mantle dynamics, basalt petrogenesis, and crustal evolution, *J. Geol., 90*, 611-643, 1982.

Ringwood, A.E., Slab-mantle interactions 3. Petrogenesis of intraplate magmas and structure og the upper mantle, *Chemical Geology, 82*, 187-207, 1990.

Ringwood, A.E., Role of th transition zone and 660 km discontinuity in mantle dynamics, *Phys. Earth Planet. Inter., 86*, 5-24, 1994.

Ringwood, A.E. and A. Major, The system Mg_2SiO_4-Fe_2SiO_4 at high pressures and temperatures, *Phys. Earth Planet. Inter., 3*, 89-108, 1970.

Royden, L.H., Evolution of retreating subduction boundaries formed during continental collision, *Tectonics, 12*, 629-638, 1993.

Royden, L.H., F. Horvath, and J. Rumpler, Evolution of the Pannonian basin system 1. Tectonics, *Tectonics, 2*, 63-90, 1983.

Rubie, D.C. and C.R. Ross, Kinetics of the olivine-spinel transformation in subducting lithosphere: experimental constraints and implications for deep slab processes, *Phys. Earth Planet. Inter., 86*, 223-241, 1994.

Sawamoto, H., D.J. Weidner, S. Sasaki, and M. Kumazawa, Single-crystal elastic properties of the modified spinel (beta) phase of magnesium orthosilicate, *Science, 224*, 749-751, 1884.

Schmalzl, J. and U. Hansen, Mixing in the Earth's mantle by thermal convection: A scale dependent Phenomenon, *Geophys. Res. Lett., 21*, 987-990, 1994.

Schubert, G., D.A. Yuen, and D.L. Turcotte, Role of transition in a dynamic mantle, *Geophys. J. R. Astr. Soc., 42*, 705-735, 1975.

Schwarz, H.R., Methode der finiten Elemente, Teubner Studienbücher, Stuttgart, 1980.

Seno, T. and S. Maruyama, Paleogeographic reconstruction and origin of the Philippine Sea, *Tectonophysics, 102*, 53-84, 1984.

Shearer, P.M. and T.G. Masters, Global mapping of topography on the 660 km discontinuity, *Nature, 355*, 791-796, 1992.

Shen, Y. and D.W. Forsyth, The effects of temperature- and pressure-dependent viscosity on three-deimensional passive flow of the mantle beneath a ridge-transform system, *J.*

Geophys. Res., 97, 19717-19728, 1992.

Silver, P.G., R.W. Carlson, and P. Olson, Deep slabs, geochemical heterogeneity and the large-scale structure of mantle convection: investigation of an enduring paradox, *Annu. Rev. Earth Planet. Sci., 16,* 477-541, 1988.

Silver, P.G. and W.W. Chan, Observations of body wave multy pathing from broadband seismograms: evidence for lower mantle slab penetration beneath the Sea of Okhotsk, *J. Geophys. Res., 91,* 13787-13802, 1986.

Solheim, L.P. and W.R. Peltier, Avalanche effects in phase transition modulated thermal convection: A model of the Earth's mantle, *J. Geophys. Res., 99,* 6997-7018, 1994.

Spakman, W., Tomographic images of the upper mantle below central Europe and the Mediterranean, *Terra Nova, 2,* 542-553, 1990.

Spakman, W., Delay time tomography of the upper mantle below Europe, the Mediterranean, and Asia Minor, *Geophys. J. Int., 107,* 309-332, 1991.

Spakman, W. and G. Nolet, Imaging algorithms, accuracy and resolution in delay time tomography, in: *Mathematical Geophysics: a survey of recent developments in seismology and geodynamics,* ed. N.J. Vlaar et al., Reidel, Dordrecht, 155-188, 1988.

Spakman, W., S. Stein, R. Van der Hilst, and R. Wortel, Resolution experiments for NW Pacific subduction zone tomography, *Geophys. Res. Lett., 16,* 1097-1100, 1989.

Spakman, W., S. van der Lee, and R. van der Hilst, Travel time tomography of the European-Mediterranean mantle down to 1400 km, *Phys. Earth Planet. Inter., 79,* 3-74, 1993.

Spakman, W., M.J.R. Wortel, and N.J. Vlaar, The Hellenic subduction zone: a tomographic image and its geodynamic implications, *Geophys. Res. Lett., 15,* 60-63, 1988.

Steinbach, V. and D.A. Yuen, The effects of multiple phase transitions on Venusian mantle convection, *Geophys. Res. Lett., 19,* 2243-2246, 1992.

Stixrude, L., R.J. Hemley, Y. Fei, and H.K. Mao, Thermoelasticity of silicate perovskite and magnesiowüstite and stratification of the Earth's mantle, *Science, 257,* 1099-1101, 1992.

Su, W.-J. and A.M. Dziewonski, Predominance of long-wavelength heterogeneity in the mantle, *Nature, 352,* 121-126, 1991.

Sumino, Y., O.L. Anderson and I. Suzuki, Temperature coeeficients of elastic constants of single crystal MgO between 80 and 1300 K, *Phys. Chem. Min., 9,* 38-47, 1983.

Sumino, Y., O. Nishizawa, T. Goto, I. Ohno, and M. Ozima, Temperature variation of elastic constants of single crystal forsterite between -190 and 400 °C, *J. Phys. Earth, 25,* 145-159, 1975.

Sung, C.-M. and R.G. Burns, Kinetics of high-pressure phase transformations: Implication to the evolution of the olivine → spinel transition in the downgoing lithosphere and its consequences on the dynamics of the mantle, *Tectonophysics, 31,* 1-32, 1976.

Suzuki, I., Thermal expansion of periclase and olivine and their anharmonic properties, *J. Phys. Earth, 23,* 145-159, 1975.

Suzuki, I., O.L. Anderson, and Y. Sumino, Elastic properties of single-crystal forsterite Mg_2SiO_4 up to 1200 K, *Phys. Chem. Min., 10,* 38-46, 1983.

Suzuki, I., K. Seya, H. Takei, and Y. Sunimo, Thermal expansion of fayalite, Fe_2SiO_4, *Phys. Chem. Min., 7,* 60-63, 1981.

Tackley, P.J., Mantle dynamics: Influence of the transition zone, *Rev Geophys.,* Supplement,

U.S. Nat. Report to IUGG 1991-1994, 275-282, 1995.

Tackley, P.J., D.J Stevenson, G.A. Glatzmaier, and G. Schubert, Effects of an endothermic phase transition at 670 km depth in a spherical model of convection in the Earth's mantle, *Nature, 361*, 699-704, 1993.

Tackley, P.J., D.J Stevenson, G.A. Glatzmaier, and G. Schubert, Effects of multiple phase transitions in a 3-D spherical model of convection in the Earth's mantle, *J. Geophys. Res., 99*, 15,877-15,901, 1994.

Tao, W.C. and R.J. O'Connell, Ablative subduction: a two-sided alternative to the conventional subduction model, *J. Geophys. Res., 97*, 8877-8904, 1992.

Turcotte, D.L. and G. Schubert, Structure of the olivine-spinel phase boundary in the descending lithosphere, *J. Geophys. Res., 76*, 1971.

Turcotte, D.L. and G. Schubert, *Geodynamics: Applications to Continuum Physics to Geological Problems,* 450 pp., Wiley, New York, 1982.

Turcotte, D.L., K.E. Torrance, and A.T. Hsui, Convection in the Earth's mantle, in: *Methods in computational physics, 13*, 431-454, 1973.

Vacher, P., A. Mocquet, and C. Sotin, Comparison between tomographic structeres and models of convection in the upper mantle, *Geophys. J. Int., 124*, 45-56, 1996.

Van der Hilst, R., Complex morphology of subducted lithosphere in the mantle beneath the Tonga trench, *Nature, 374*, 154-157, 1995.

Van der Hilst, R. and S. Seno, Effects of relative plate motion on the deep structure and penetration depth of slabs below the Izu-Bonin and Mariana island arcs, *Earth Planet. Sci. Lett., 120*, 395-407, 1993.

Van der Hilst, R. and R. Snieder, High-frequency precursors to P wave arrivals in New Zealand: Implications for slab structure, *J. Geophys. Res., 101*, 8473-8488, 1996.

Van der Hilst, R. and W. Spakman, Importance of the reference model in linearized tomography and images of subduction below the Carribean plate, *Geophys. Res. Lett., 16*, 1093-1096, 1989.

Van der Hilst, R., E.R. Engdahl, W. Spakman, and G. Nolet, Tomographic imaging of subducted lithosphere below northwest Pacific island arcs, *Nature, 353*, 37-43, 1991.

Van der Hilst, R., E.R. Engdahl, and W. Spakman, Tomographic inversion of P and pP data for aspherical mantle structure below the northwest Pacific region, *Geophys. J. Int., 115*, 264-302, 1993.

Van Keken, P.E., S. Karato, and D.A. Yuen, Rheological control of oceanic crust separation in the transition zone, *Geophys. Res. Lett.,* in press, 1996.

Vassiliou, M.S., B.H. Hager, and A. Raefsky, The distribution of earthquakes with depth and stress in subducting slabs, *J. Geodyn., 1*, 11-28, 1984.

Vidale, J.E., Waveform effects of a high velocity subducted slab, *Geophys. Res. Lett., 14*, 542-545, 1987.

Vidale, J.E. and H.M. Benz, Upper mantle seismic discontinuities and the thermal structure of subduction zones, *Nature, 356*, 678-683, 1992.

Vidale, J.E. and D. Garcia-Gonzalez, Seismic observations of a high velocity slab 1200-1600 km in depth, *Geophys. Res. Lett., 15*, 369- 372, 1988.

Vidale, J.E., Q. Williams , and H. Houston, Waveform effects of a metastable olivine tongue in

subducting slabs, *Geophys. Res. Lett., 18*, 2201-2204, 1991.

Vlaar, N.J., Thermal anomalies and magmatism due to lithospheric doubling and shifting, *Earth Planet. Sci. Lett., 65*, 322-330, 1983.

Vlaar, N.J. and M.J.R. Wortel, Lithospheric aging, instability and subduction, *Tectonophysics, 32*, 331-351, 1976.

Wang, H. and G. Simmons, Elasticity of some mantle crystal structures 1. Pleonaste and hercynite spinel, *J. Geophys. Res., 77*, 4379-4392, 1972.

Weidner, D.J., H. Sawamoto, and S. Sasaki, single-crystal elastic properties of the spinel phase of Mg_2SiO_4, *J. Geophys. Res., 89*, 7852-7860, 1984.

Wicks, C.W. Jr and M.A. Richards, A detailed mapp of the 660 km discontinuity beneat the Izu-Bonin subduction zone, *Science, 261*, 1424-1427, 1993.

Widiyantoro, S. and R. Van der Hilst, Structure and evolution of lithospheric slab beneath the Sunda arc, Indonesia, *Science, 271*, 1566-1569, 1996.

Wortel, R., Age-dependent subduction of oceanic lithosphere, PhD thesis, Universiteit Utrecht, Utrecht, pp 147, 1980.

Wortel, R., Seismicity and rheology of subducted slabs, *Nature, 296*, 553-556, 1982.

Wortel, R., Deep earthquakes and the thermal assimilation of subducting lithosphere, *Geophys. Res. Lett., 13*, 34-37, 1986.

Wortel, M.J.R. and W. Spakman, Structure and dynamics of subducted lithosphere in the Mediterranean region, *Proc. Kon. Ned. Akad. v. Wetensch., 95*, 325-347, 1992.

Wortel, M.J.R. and N.J. Vlaar, Subduction zone seismicity and the thermo-mechanical evolution of down-going lithosphere, *Pageoph, 128*, 554-562, 1988.

Yoshioka, S. and M.J.R. Wortel, Three-dimensional numerical modeling of detachment of subducted lithosphere, *J. Geophys. Res., 100*, 20223-20244, 1995.

Yuen, D.A., D.M. Reuteler, S. Balachandar, V. Steinbach, A.V. Malevsky, and J.L. Smedsmo, Various influences on three-dimensional mantle convection with phase transitions, *Phys. Earth Planet. Inter., 86*, 185-203, 1994.

Zhao, W., D.A. Yuen, and S. Honda, Multiple phase transitions and the style of mantle convection, *Phys. Earth Planet. Inter., 72*, 185-210, 1992.

Zhong, S. and M. Gurnis, Role of plates and temperature-dependent viscosity in phase change dynamics, *J. Geophys. Res., 99*, 15,903-15,917, 1994.

Zhong, S. and M. Gurnis, Mantle convection with plates and mobile, faulted plate margins, *Science, 267*, 838-843, 1995.

Zhou, H.-W., Mapping of P wave slab anomalies beneath the Tonga, Kermadec and New Hebrides arcs, *Phys. Earth Planet. Inter., 61*, 199-229, 1990a.

Zhou, H.-W., Observations on earthquake stress axes and seismic morphology of deep slabs, *Geophys. J. Int., 103*, 377- 401, 1990b.

Zhou, H.-W. and R.W. Clayton, P and S wave travel time inversions for subducting slab under the island arcs of the northwest Pacific, *J. Geophys. Res., 95*, 6829-6851, 1990.

Zienkiewicz, O.C., *The finite element method*, McGraw-Hill, 3rd edition, 1977.

Samenvatting (Summary in Dutch)

De beweging van oceanische en continentale lithosfeer, vulkanische activiteit, aardbevingen en andere tektonische verschijnselen vormen een uitdrukking van processen in de aardmantel. Het is tegenwoordig algemeen aanvaard dat deze verschijnselen samenhangen met convectie-stromingen in de mantel. Deze convectie vormt het mechanisme waardoor warmte uit het inwendige van de Aarde wordt omgezet in mechanische arbeid. Een voorbeeld van dit mechanisme is de vorming van oceanische lithosfeer bij mid-oceanische ruggen, waar warm mantelmateriaal opstijgt. Aan randen, waar twee platen naar elkaar toe bewegen, duikt een lithosfeerplaat (de oceanische) in de mantel - ze wordt gesubduceerd.

Het grootste gedeelte van de informatie met betrekking tot de struktuur van de Aarde is afkomstig van de seismologie. Seismologische observaties hebben laten zien dat er een grote variatie in de geometrie van subductiezones bestaat. Er bestaan subducerende platen met een zeer kleine hellingshoek (bijvoorbeeld: Peru) en tevens platen met een hellingshoek van bijna 90° (bijvoorbeeld: Marianen). De platen kunnen stagneren aan de grens tussen boven- en ondermantel (bijvoorbeeld: Izu-Bonin) maar ook doordringen in de ondermantel (bijvoorbeeld: Sundaboog). De initiatie en het eindigen van subductie vormen een manifestatie van de tijdsafhankelijkheid van de dynamische processen in de mantel.

Afbeeldingen van de verdeling van de seismische snelheid in de mantel bieden een momentopname van de tijdsafhankelijke struktuur die, gekoppeld aan tijdsafhankelijke processen, in een dynamische context moeten worden geïnterpreteerd. Het is de doelstelling van dit proefschrift om meer inzicht te verkrijgen in de evolutie van het subductieproces. Er wordt onderzocht in welke mate de geometrie van subductie afhankelijk is van parameters zoals de plaatsnelheid en de viscositeitsstruktuur van de mantel. Voor dit doel wordt in deze studie gebruik gemaakt van computermodellen. Numerieke studies hebben het voordeel dat de parameters over een groot bereik kunnen worden gevarieerd. De snelheden van platen en van mantelstroming kunnen eenvoudig (vooral in vergelijking met laboratorium-experimenten) als randvoorwaarden worden opgenomen. Het dient te worden opgemerkt dat ons model ook vereenvoudigingen omvat. De meest fundamentele vereenvoudiging is wellicht het verwaarlozen van de derde dimensie.

Gedurende de laatste 20 jaar zijn er ten aanzien van subductiezones talrijke studies verricht. *Hoofdstuk 2* geeft een overzicht van recente en invloedrijke resultaten van de verschillende deelgebieden van de geofysica. Er wordt ingegaan op de informatie omtrent struktuur en evolutie van subducerende platen zoals die wordt geleverd door de seismologie, geoïde data, plaattektonische analyses en door zowel numerieke als experimentele studies. Deze informatie vormt de basis voor het onderzoek in dit proefschrift.

In *Hoofdstuk 3* wordt de numerieke methode die ten grondslag ligt aan het twee-

dimensionale model gepresenteerd. Als eerste worden de basisvergelijkingen behandeld die een beschrijving vormen van het convectiesysteem dat de aardmantel voorstelt. Aansluitend wordt de eindige-elementenmethode beschreven waarvan bij de berekeningen gebruik zal worden gemaakt. Omdat het hier beschreven onderzoek grotendeels is gebaseerd op seismologische resultaten is tevens aandacht geschonken aan de omrekening van gemodelleerde temperatuur naar seismische snelheid. Deze transformatie wordt eveneens in *Hoofdstuk 3* behandeld.

Hoofdstuk 4 betreft de invloed van de viscositeitsstruktuur van de mantel op een subducerende plaat. De viscositeit zou over de dikte van de lithosfeer kunnen afnemen met een factor van drie tot vier ordes van grootte. Aan de grens tussen boven- en ondermantel neemt de viscositeit waarschijnlijk weer met een factor van 10 tot 100 toe. De details van het viscositeitsprofiel zijn nog altijd omstreden.

Omdat in *Hoofdstuk 4* de eerste modelresultaten worden gepresenteerd zullen hier tevens het model en het modelschema worden beschreven. Het gemodelleerde gebied omvat de bovenste 1200 km van de Aardmantel. De toepassing van geschikte randvoorwaarden, zoals bijvoorbeeld een achtergrond-mantelstroming en een 'open' bodem (waar materiaal doorheen kan vloeien), levert een model dat deel uitmaakt van een convectiesysteem waarbij de gehele mantel is betrokken. De stijfheid van de lithosfeerplaten wordt gemodelleerd door middel van een temperatuur-afhankelijke viscositeit. Het Rayleigh getal (Ra), dat een maat vormt voor de instabiliteit van het convectieve systeem, wordt gekozen tussen 10^6 en 10^7. Het Rayleigh getal is gebaseerd op de viscositeit in de bovenmantel. Toename van Ra met één orde van grootte impliceert dus een afname van de referentieviscositeit met één orde van grootte. De keus voor Ra is in overeensteming met het 'open' karakter van het model - zijnde een onderdeel van het systeem van convectie van de gehele mantel.

Ons twee-dimensionale model laat zien dat een toename in viscositeit aan de grens tussen boven- en ondermantel met een factor van 300 niet voldoende is om het indringen van een subducerende plaat in de ondermantel te verhinderen. De geometrie van de anomaliën (temperatuur en seismische snelheid) veroorzaakt door een subducerende plaat hangt sterk af van de viscositeitseigenschap van de dalende lithosfeer. We vinden tevens dat een verandering in de snelheid van de onderduikende plaat geen fundamenteel effect op de geometrie heeft. Samengevat kan worden geconcludeerd dat de grote variatie die wordt waargenomen in de struktuur van subductiezones niet alleen door veranderingen in de viscositeit en in de snelheid van de subducerende plaat kan worden verklaard.

In *Hoofdstuk 5* wordt de invloed van migratie van de trog op het subductieproces behandeld. In toevoeging tot de modellen van *hoofdstuk 4* is de overschuivende plaat nu mobiel. Voor de analyse van trogmigratie wordt de achtergrond-mantelstroming belangrijk. Er moet niet alleen rekening worden gehouden met de absolute plaat- en trogsnelheid, zoals gespecificeerd in bijvoorbeeld het hotspot referentiesysteem,

maar ook met relatieve bewegingen tussen platen aan de oppervlakte en de daaronder stromende mantel. Dit hoofdstuk is opgedeeld in drie delen. In het eerste gedeelte onderzoeken we de verandering van viscositeit, maar in tegenstelling tot *hoofdstuk 4* is nu trogmigratie aanwezig. Gebaseerd op de resultaten van zowel *hoofdstuk 4* als *hoofdstuk 5* wordt een viscositeitsprofiel gekozen voor de volgende modellen. In het tweede gedeelte wordt een gedetailleerd onderzoek uitgevoerd met betrekking tot de invloed van trogmigratie op het subductieproces, zonder de radiale viscositeits-struktuur verder te veranderen. Analyse van relatieve bewegingen tussen lithosfeer en de daaronder liggende mantel heeft gewezen op het optreden van een globale oostelijke mantelstroming ten opzichte van de platen. Dit zou kunnen betekenen dat er een verschil tussen oost- en westwaarts subducerende platen is. De vergelijking tussen oost- en westwaarts duikende platen vormt de opgave in het derde gedeelte.

We vinden dat in combinatie met trogmigratie, een toename van de viscositeit aan de grens tussen boven- en ondermantel de mogelijkheid verminderd dat de subducerende plaat in de hoog viskeuze ondermantel duikt. De stijfheid van de lithosfeer verkleint de kans dat de plaat door de 670 km discontinuïteit doordringt. Een toename van trogmigratie, in de orde van geobserveerde waarden, doet de mogelijkheid dat de gesubduceerde plaat in de ondermantel dringt afnemen. Onze modellen laten zien dat de struktuur van de ondergedoken plaat zelfs gevoelig is voor kleine waarden van trogmigratie (1 cm/jaar). Modellen met grotere Rayleigh getallen (10^7) zijn overwegend sterk tijdsafhankelijk. Fases met het direkt induiken in de ondermantel wisselen af met fases van een vlakke plaatstruktuur in de bovenmantel. We concluderen dat de tijdsafhankelijkheid en de individuele tektonische gegevens van een subductiezone een grote variatie van anomaliën kunnen opleveren. Tenslotte laat de transformatie van de modeltemperatuur naar de seismische P-golfsnelheid een goede overeenstemming zien met de struktuur van geobserveerde seismische anomaliën.

In *hoofdstuk 6* bestuderen we de afhankelijkheid van subductie van de ouderdom van de lithosfeer. Het ouder worden van de lithosfeer gaat samen met afkoeling en met toename van de dichtheid als gevolg van thermische contractie. Een karakteristiek aspect dat wordt veroorzaakt door het ouder worden van de lithosfeer is toename van de dikte van de plaat. Het voorgaande suggereert dat de ouderdom van de lithosfeer die gesubduceerd wordt van belang is voor de daar op volgende processen. Er worden in subductiezones, in samenhang met de ouderdom, twee verschillende dieptebereiken geobserveerd waarin aardbevingen optreden. In subductiezones waar de onderduikende lithosfeer jonger is dan 70 Ma ligt de aardbevingshaard nooit dieper dan 300 km. Alleen in subductiezones waar lithosfeer ouder dan 70-100 Ma wordt geconsumeerd vinden aardbevingen op een diepte van 500-700 km plaats. Het wordt aangenomen dat oude lithosfeer sneller zinkt en kouder is dan jonge lithosfeer. In deze snel zinkende plaat zou de temperatuur in

het koude binnenste onder een karakteristische waarde kunnen blijven. Daarbij
zal de faseovergang van olivijn naar spinel op een diepte van 400 km naar beneden
worden verschoven. Volgens een actuele hypothese vormt deze verplaatsing van
de olivijn-spinel faseovergang het mechanisme van diepe aardbevingen die gepaard
gaan met een hoge vrijgave van energie. Als de faseovergang van olivijn naar spinel
bij een hogere temperatuur plaatsvindt, zoals waarschijnlijker is voor jonge en
langzaam subducerende lithosfeer, geschiedt deze transformatie op een diepte van
ongeveer 400 km.

Voor jonge en oude lithosfeer wordt een plaatdikte genomen van respektievelijk
55 km en 100 km, hetgeen overeenkomt met circa 20-30 Ma en 100 Ma oude
lithosfeer. Onze modelresultaten suggereren dat de minimum temperatuur in het
inwendige van de oude en dikke lithosfeer lager is dan in de jonge en dunne plaat.
Dit betekent dat de faseovergang van olivijn naar spinel in jonge lithosfeer zou
kunnen plaatsvinden onder evenwicht op een diepte van circa 400 km, maar dat de
transformatie onderdrukt zou kunnen worden in oude lithosfeer. Dus ondersteunen
onze modelresultaten de voorgestelde verklaring voor de geobserveerde relatie
tussen de diepte van aardbevingen in subductiezones en de ouderdom van de
subducerende platen.

In *Hoofdstuk 7* wordt ingegaan op subductieprocessen die vroeger aan conver-
gente marges actief waren. Zo wijzen, bijvoorbeeld, studies van de tectonische
geschiedenis van het Karpaten orogeen er op dat subductie in dit gebied gedurende
het Midden Mioceen gestopt is. Opheffing van het Transsylvanische bekken en
het omringende gebergte gedurende het Plioceen en Kwartair kunnen worden
geïnterpreteerd als zijnde het gevolg van het afbreken van de subducerende plaat
(het zogenaamde 'detachment') en de daarmee gepaard gaande opheffing van de be-
lasting. Tomografische resultaten laten hoge P-golfsnelheidsanomaliën onder het
Oost-Europeese platform zien, die geïnterpreteerd worden als afgebroken plaat.
Tomografische studies wijzen tevens op het bestaan van vroegere subductie onder
Spanje. De combinatie van tomografische en tektonische gegevens suggereert dat
in dit gebied subductie plaats gevonden zou moeten hebben gedurende tenminste
een deel van het Oligoceen, gevolgd door detachment van de gesubduceerde plaat
in het Vroeg Mioceen. Ons model laat zien dat het - in het algemeen - waarschi-
jnlijk is dat dit afbreken plaatsvindt nadat het subductieproces is gestopt. Hierbij
is de tijdsspanne tussen het ophouden van subductie en detachment met circa 200
Ma veel te lang voor de modellen met een laag Rayleigh getal (10^6). Geologische
en tomografische studies van de Karpaten en het Betisch-Alboran gebied wijzen er
op dat detachment circa 10-15 Ma na het ophouden van subductie is opgetreden.
Modellen met een hoger Rayleigh getal ($5 \cdot 10^6$, 10^7) zijn in betere overeenstem-
ming met de observaties. Transformatie van de modeltemperatuur naar seismische
anomaliën toont aan dat de sterktes van de seismische anomaliën met de tijd
afnemen. De afnemende gevoeligheid van de seismische snelheid voor de temper-

atuuranomaliën met toenemende diepte zou de mogelijkheid kunnen verminderen om een afgebroken gedeelte van lithosfeer via de tomografische methode te kunnen ontdekken. Wij vinden dat na circa 100 Ma de gesubduceerde plaat nauwelijks nog 'zichtbaar' is voor de seismische tomografie.

In *Hoofdstuk 8* wordt ons model toegepast op subductiezones in het gebied van noordwestelijke Stille Oceaan. Tomografische resultaten tonen aan dat onder de Izu-Boninboog de subducerende plaat stagneert op de grens naar de ondermantel, maar onder de Marianenboog bijna rechtdoor in de ondermantel duikt. Dit verschil in geometrie zou verklaard kunnen worden door de tektonische geschiedenis van de beide gebieden. Reconstructies suggereren dat de trogmigratie bij Izu-Bonin tussen 30 Ma en 17 Ma circa 7.5 cm/jaar bedroeg. Bij Mariana was dit, gedurende dezelfde periode, slechts circa 3 cm/jaar. Omdat de resultaten van *Hoofdstuk 5* hebben laten zien dat trogmigratie een grote rol speelt in het subductieproces hebben we getoetst of het veronderstelde verschil in trogmigratie de geobserveerde verschillen in geometrie zou kunnen veroorzaken. Ons dynamisch model, dat het voor de noordwestelijke Stille Oceaan voorgestelde tektonische scenario als invoer gebruikt, voorspelt een hedendaagse struktuur van subductiezones die in goede overeenstemming is met de tomografische resultaten.

150

Acknowledgments

Ik wil iedereen bedanken die een bijdrage heeft geleverd bij de totstandkoming van dit proefschrift. Allereerst wil ik mijn promotor Rinus Wortel bedanken voor zijn begeleiding van dit onderzoek. Ik heb veel van zijn brede vakkennis geleerd en zijn ideeen en advies hebben me altijd gemotiveerd en verder geholpen. I want to thank my Co-Promotor Ulli Hansen that I could use his numerical model for this study. Particularly, I want to thank him that I could appear at his office with my questions at any time. Arie van den Berg dank ik voor zijn steun in het begin van mijn onderzoek. Wim Spakman heeft de tomografische plaatjes in dit proefschrift verzorgd. Daarvoor wil ik hem bedanken. De tomografische plots uit hoofdstuk 8 zijn gebaseerd op het werk van Rob van der Hilst. Ook hem wil ik daarvoor bedanken zijn resultaten beschikbaar gesteld te hebben. Jörg Schmalzl installed and established a lot of computer facilities and programs - as for example all the graphics software - which I used for this thesis. Many thanks to him for his support at the computer. I would like to thank Rachel Walcott for reading and correcting Chapter 2. I also thank Rachel that she asked me to be her field assistent on the Cyclades last spring; and thank Jörg for the ticket! I had a very good time and could relax from my work. Mijn kamergenoot Paul Meijer was altijd behulpzam. In het bijzonder wil ik hem voor het vertalen van de samenvatting in het Nederlands en voor de hulp bij figuur 2.2 bedanken. I am grateful to Andrew Curtis and Rachel Walcott that I could stay at their place in the very last phase of finishing my thesis. The most important support, however, I got from Jörg. Not only for his help at the computer, but much more I would like to thank him that he particularly in the harder times kept cheering me up.

Curriculum Vitae

16.05.1963 Born in Köln, Germany
1982   Abitur at the Gymnasium Erftstadt Lechenich
1982-1984   Study of Mathematics at the University Köln, Germany
1984-1991   Study of Geophysics at the University Köln, Germany
1991-1997   PhD student at the Department of Geophysics,
            Utrecht University

List of Symbols

b	parameter controling temperature dependence of the viscosity (see eqn. 4.1)
c	parameter controling depth dependence of the viscosity (see eqn. 4.1)
d_L	thermal thicknesss of lithospheric plates [km]
$\vec{g}$	acceleration vector of gravity [m s^{-2}]
K	bulk modulus [GPa]
m_e	effective trench migration rate [cm/yr]
P	hydrodynamic pressure [Pa]
Ra	Rayleigh number
t	time [Myr, dimensionless]
t_{pc}	time elapsed since subduction has ceased [Myr]
Δtc	time period during which convergence velocity decreases to zero [Myr]
Δtd	time period between cessation of subduction and slab detachment [Myr]
T	temperature [°C, dimensionless]
T_s, T_{ch}	specified, characteristic temperature [°C]
$\vec{v}$	velocity vector
v_c	convergence velocity [cm/yr]
v_m	background mantle flow [cm/yr]
v_o	overriding plate velocity [cm/yr]
v_p	seismic P-wave velocity [km/s]
Δv_p	seismic P-wave velocity anomaly [%]
v_u	underthrusting plate velocity [cm/yr]
x, z	x-, z-component of direction
α	thermal expansion coefficient [K^{-1}]
β	lower to upper mantle viscosity ratio
η	dynamic viscosity
η_{lo}	lower mantle viscosity
η_{up}	upper mantle viscosity
η_0	reference viscosity (upper mantle)
κ	thermal diffusivity [m^2 s^{-1}]
λ	aspect ratio (width to height) of the model domain
μ	rigidity [GPa]
ρ	density [kg m^{-3}]
$\underline{\underline{\sigma}}$	deviatoric stress tensor [Pa]
ψ	stream function